12-1-2012

Topics in Galaxy Formation: Pairwise Velocities of Dark Matter Halos and Molecular Hydrogen Regulated Star Formation in Cosmological Simulations

Robert Jo Thompson
University of Nevada, Las Vegas, rlthomps@unlv.nevada.edu

TOPICS IN GALAXY FORMATION: PAIRWISE VELOCITIES OF DARK MATTER HALOS AND MOLECULAR HYDROGEN REGULATED STAR FORMATION IN COSMOLOGICAL SIMULATIONS

By

Robert Jo Thompson

Bachelor of Science in Physics
University of Nevada, Las Vegas
2008

Master of Science in Astronomy
University of Nevada, Las Vegas
2010

A dissertation submitted in partial fulfillment
of the requirements for the

Doctor of Philosophy in Astronomy

Department of Physics & Astronomy
College of Sciences
The Graduate College

University of Nevada, Las Vegas
December 2012

THE GRADUATE COLLEGE

We recommend the dissertation prepared under our supervision by

Robert Thompson

entitled

Topics in Galaxy Formation: Pairwise Velocities of Dark Matter Halos and Molecular Hydrogen Regulated Star Formation in Cosmological Simulations

be accepted in partial fulfillment of the requirements for the degree of

Doctor of Philosophy in Astronomy
Department of Physics and Astronomy

Kentaro Nagamine, Ph.D., Committee Chair

Daniel Proga, Ph.D., Committee Member

Stephen Lepp, Ph.D., Committee Member

Balakrishnan Naduvalath, Ph.D., Graduate College Representative

Tom Piechota, Ph.D., Interim Vice President for Research &
Dean of the Graduate College

December 2012

ABSTRACT

In this dissertation we investigate two distinct challenges within the concordance ΛCDM model and an unrelated project. The first is a discrepancy between theory and observation. A massive galaxy sub-cluster known as the 'bullet' has fallen through a more massive parent galaxy cluster at a redshift of $z = 0.296$. Theory finds that in order to reproduce the observational quantities of this cluster, an unusually high relative velocity of $v_{12} = 3000\,\mathrm{km\,s^{-1}}$ between the two cluster's parent halos is required. We quantify the statistical probability of producing a 'bullet-like' halo pair within large N-body simulations, and conclude that either the ΛCDM model is currently incompatible with observations, or the inferred relative velocity must be revised to a lower value. Recent improvements to the observed mass estimates provide hope that we may be able reconcile the differences in the future.

The second challenge is on the topic of galaxy formation within cosmological smoothed particle hydrodynamic simulations. Recent observational evidence suggests that star formation correlates tightly with the presence of molecular hydrogen (H_2). New analytic models have emerged allowing us to calculate the mass fraction of H_2 at virtually no computational cost. We can then regulate star formation within our simulations by the local abundance of H_2, rather than the gas density. A comparison study between the new H_2-based star formation prescription and previous models is presented, detailing the advantages and disadvantages of the new model.

Finally we discuss the construction of a galactic halo and disk with the goal of exploring and developing a better method for implementing supernova feedback in small scale hydrodynamic simulations. This proves to be a non-trivial process, and ultimately an unrealistic method to construct galaxies in a cosmological context.

ACKNOWLEDGMENTS

I would first like to express my sincerest gratitude to my adviser, Dr. Kentaro Nagamine, for welcoming me into his office nearly five years ago. Without his patience, persistence, and encouragement this thesis may well have never been completed. More importantly, his incredible work ethic and healthy skepticism inspires me to be a better scientist on a daily basis. It has been a great pleasure working with him, and I look forward to our future collaborations.

Thank you to my committee members for your helpful comments, insightful suggestions, and your time: Drs. Kentaro Nagamine, Daniel Proga, Stephen Lepp, & Balakrishnan Naduvalath.

I have had many wonderful professors throughout the years and would like to thank them for their dedication to teaching. I learned a great deal from Drs. Kentaro Nagamine, Daniel Proga, Bing Zhang, Stephen Lepp, & George Rhee in their amazingly insightful graduate courses over the past few years. I would like to thank Dr. Lon Spight for teaching me to always be skeptical, it plays an important role in my everyday life. Two in particular are responsible for introducing me to the wonderful subject of astronomy: Drs. Dale Etheridge & Harold Nations. I am grateful to them for teaching me to the basic ideas and concepts that left me captivated and wanting to know more.

I must thank the many graduate students who have provided stimulating con-

versation and encouragement over the years: John Howard, Jason Baker, Francisco Virgili, Amanda Maxham, Stefan Luketic, John Boisvert, Matthew Kelley, Ed Romano, Liz Tanis, Tim Waters, Bin Bin Zhang, David Whitehead, Keita Todoroki, and many others. I am especially thankful to Jason Jaacks & Saju Varghese for their active participation and significant contributions to our group. I have greatly benefited from conversations with Drs. Jun-Hwan Choi and Amit Kashi; thank you for the laughs. I am grateful to John Kilburg & Jay Nietling for their hard work keeping the department computer systems up & running smoothly, and Ron Young at the NSCEE for his help with the local cluster Eureka. I would also like to thank the Physics & Astronomy department staff for always taking care of my paperwork in a very timely manner and keeping me well informed.

My parents Terri & Kurt Lord deserve all the credit in the world for their constant love and support. They have always encouraged me to make my own decisions and have supported me regardless. Without them, none of this would have been possible. Lastly I would like to thank the love of my life Hillary. She has been my inspiration in times of doubt, and unknowingly motivated me nearly every step of the way.

TABLE OF CONTENTS

LIST OF TABLES

LIST OF FIGURES

CHAPTER 1

INTRODUCTION

The Λ Cold Dark Matter (ΛCDM) model (Blumenthal et al., 1984; Ostriker & Steinhardt, 1995) is currently the most widely accepted model of our Universe. It is based on Einstein's theory of General Relativity and the Cosmological Principle. General Relativity provides the mathematical framework for describing gravity as the distortion of space-time by the energy & momentum of matter & radiation. The Cosmological Principle postulates that on sufficiently large scales ($> 100\,\mathrm{Mpc}$) the Universe is isotropic and homogeneous. This means that there is no preferred reference frame, the Universe appears the same regardless of an observer's location, and the laws of physics are the same in all places at all times. Friedmann (1922, 1924) & Lemaître (1927) independently derived a solution to the Einstein field equations of General Relativity describing such a Universe; Robertson (1935, 1936a,b); Walker (1937) was able to later show that these were unique solutions and they became known as the Friedmann-Lemaître-Robertson-Walker (FLRW) metric. Friedmann's first analytic solution to the Einstein equation relates the time derivative of the scale factor a to the energy density, vacuum energy density, and curvature of the Universe

$$H^2 = \left(\frac{\dot{a}}{a}\right)^2 = \frac{8\pi G}{3}\rho - \frac{kc^2}{a^2} + \frac{\Lambda}{3}. \tag{1.1}$$

Here H is the Hubble parameter, G is Newton's gravitational constant ($G = 6.67 \times 10^{-8}\mathrm{cm}^3\mathrm{g}^{-1}\mathrm{s}^{-2}$), ρ the mass density of the universe composed of baryonic matter and non-baryonic dark matter, k the spatial curvature which takes the form of three solutions ($k = 0$ for a flat Universe, $k = -1$ for a negatively curved or open Universe,

and $k = +1$ for a positively curved or closed Universe), and Λ the cosmological constant which allows for the current accelerating expansion of the Universe. By assuming the cosmological constant Λ and the spatial curvature k are equal to zero, we can solve Equation 1.1 for a critical density in which the Universe remains flat:

$$\rho_{c,0} = \frac{3H_0^2}{8\pi G} = 2.77 \times 10^{11} h^2 \, \mathrm{M}_\odot \, \mathrm{Mpc}^{-3}, \tag{1.2}$$

where H_0 denotes the Hubble parameter at present time, and $h \equiv H_0/100 \, \mathrm{km \, s^{-1} \, Mpc^{-1}}$. We can now define the matter density of the universe as:

$$\Omega_m \equiv \frac{\rho}{\rho_c}. \tag{1.3}$$

We can derive two additional cosmological parameters from Equation 1.1: the curvature $\Omega_k \equiv kc^2/(aH)^2$, and the vacuum energy density $\Omega_\Lambda \equiv \Lambda/(3H^2)$. These three parameters describe how the energy of the Universe is distributed and must satisfy the sum rule $\Omega_\mathrm{m} + \Omega_k + \Omega_\Lambda = 1$.

ΛCDM has been successful due to its predictive power, and its ability to explain a wide variety of observations. The most notable of which, was the detection of a predicted background radiation by Penzias & Wilson (1965), interpreted to be a remnant of the Big Bang (Dicke et al., 1965). This cosmic microwave background (CMB) radiation was measured to have a uniform temperature of $T \sim 2.7 \, \mathrm{K}$ across the entire sky. Two decades later, small anisotropies of $\Delta T/T \sim 10^{-5}$ in the CMB temperature were detected by the COBE satellite (Smoot et al., 1992). These anisotropies proved to be one of the strongest pieces of evidence in support of the ΛCDM model, which describe these anisotropies as temperature peaks & troughs in early baryonic acoustic oscillations. Recent observations have also provided precise measurements of the CMB's polarization (see Komatsu et al., 2011).

These measurements put very tight constraints on the cosmological parameters

described above: $\Omega_\Lambda = 0.725 \pm 0.016$, $-0.0133 < \Omega_k < 0.0084$, and $\Omega_\mathrm{m} = 0.274 \pm 0.004$ which is composed of both baryonic matter $\Omega_b = 0.0458 \pm 0.002$ and dark matter $\Omega_\mathrm{dm} = 0.229 \pm 0.015$ (Komatsu et al., 2011). Other parameters are also tightly contained by the CMB observations: The primordial power spectrum is described by $P \propto k^{n_s}$, where $n_s = 0.968 \pm 0.012$ is the spectral index of scalar fluctuations, and the amplitude of the linear power spectrum on the scale of $8\,h^{-1}\,\mathrm{Mpc}$ is constrained to $\sigma_8 = 0.816 \pm 0.024$ (Komatsu et al., 2011). CMB measurements, coupled with supernova type Ia data (Riess et al., 1998; Kowalski et al., 2008), can also constrain the Hubble parameter $H_0 = 70.2 \pm 1.4\,\mathrm{km\,s^{-1}\,Mpc^{-1}}$. These results describe a flat Universe dominated by a vacuum energy density $\sim 73\%$, and non-baryonic dark matter $\sim 23\%$. The remaining $\sim 4\%$ is attributed to normal every day baryonic matter.

The theory however, is not without challenges. For example, strong empirical evidence for the existence of dark matter has recently been found in observations of the large galaxy cluster 1E0657-56 (Clowe et al., 2006). The relative velocity between these two clusters has been inferred to be quite high, contrary to predictions from cosmological CDM simulations which have shown very good agreement with the observed large scale structure of the Universe (Davis et al., 1985; Springel et al., 2006). This specific discrepancy between theory and observation is investigated in Chapter 2 of this thesis.

When and how galaxies form poses another challenge to the ΛCDM model. In a simplified picture, hot gas cools by radiating energy away while falling into the gravitational potential wells of dark matter halos. Dense molecular clouds then provide a suitable environment for star formation. Feedback from young stars in the form of ultraviolet (UV) radiation and supernova (SN) explosions return energy & metals to the surrounding medium regulating the star formation process. We have a clear theoretical picture of how mass is distributed throughout the Universe in the form of

dark matter halos (e.g. Davis et al., 1985; Springel et al., 2006), and observationally we have a good picture of how luminosity is distributed via large sky surveys (e.g. Abazajian et al., 2009; Grogin et al., 2011); the challenge lies in linking the two.

One of the most direct ways in which we can approach this highly nonlinear problem is through the use of numerical simulations. Two distinct types of code have found great success in modeling galaxy formation in the ΛCDM context: Adaptive Mesh Refinement (AMR; e.g. Bryan & Norman, 1997) and Smoothed Particle Hydrodynamics (SPH; see Springel, 2010, for a review). Both solve the hydrodynamic equations directly, but in very different ways. SPH codes divide the fluid element into a set of discrete elements or particles, while AMR covers the computational volume with an adaptive mesh. SPH codes are generally faster, and have lower memory footprints. However, SPH is not without its limitations. AMR is much more accurate in capturing shocks, generally has better resolution in low density regions, and easily mixes gas properties (thermal energy, metals, etc.).

Current computers are not powerful enough to simultaneously solve the for large scale structure and the small scale processes involved in galaxy formation with sufficient resolution. These small small scale processes (such as star formation and feedback) must then be approximated by statistical representations of larger scale trends; these are referred to as 'sub-grid' models. Over the past decade computing power has increased tremendously allowing for the inclusion of more realistic physics into our sub-grid models, which is the subject of Chapter 3.

In Chapter 3 we also introduce baryonic physics into our simulations: our aim is to improve upon previous sub-grid star formation prescriptions. We examine galaxy properties such as the stellar-halo-mass-ratio (SHMR), galaxy stellar mass function (GSMF), mass-metallicity relation, and Kennicutt-Schmidt (KS) relationship. In Chapter 4 I briefly touch on unpublished work of creating a quasi-equilibrium dark matter halo. Final discussions and future prospects can be found in Chapter 5.

CHAPTER 2

PAIRWISE VELOCITIES OF DARK MATTER HALOS: A TEST FOR THE Λ COLD DARK MATTER MODEL USING THE BULLET CLUSTER

Abstract

The existence of a bullet cluster (such as 1E0657-56) poses a challenge to the concordance Λ cold dark matter model. Here we investigate the velocity distribution of dark matter halo pairs in large N-body simulations with differing box sizes ($250h^{-1}\,\mathrm{Mpc} - 2h^{-1}\mathrm{Gpc}$) and resolutions. We examine various basic statistics such as the halo masses, pairwise halo velocities (v_{12}), collisional angles, and pair separation distances. We then compare our results to the initial conditions required to reproduce the observational properties of 1E0657-56 in non-cosmological hydrodynamical simulations.

We find that the high velocity tail of the v_{12} distribution extends to greater velocities as we increase the simulation box size. We also find that the number of high-v_{12} pairs increases as we increase the particle count and resolution with a fixed box size, however, this increase is mostly due to lower mass halos which do not match the observed masses of 1E0657-56. We find that the redshift evolution effect is not very strong for the v_{12} distribution function between z=0.0 and $z\sim$0.5.

We identify some pairs whose v_{12} resemble the required initial conditions, however, even the best candidates have either wrong halo mass ratios, or too large separations. Our simulations suggest that it is very difficult to produce such initial conditions at $z = 0.0, 0.296,$ & 0.489 in comoving volumes as large as $(2\,h^{-1}\mathrm{Gpc})^3$. Based on the

extrapolation of our cumulative v_{12} function, we find that one needs a simulation with a comoving box size of $(4.48\,h^{-1}\,\mathrm{Gpc})^3$ and 2240^3 DM particles in order to produce at least one pair of halos that resembles the required v_{12} and observed masses of 1E0657-56. From our simulated v_{12} probability distribution function, we find that the probability of finding a halo pair with $v_{12} \geq 3000\,\mathrm{km\,s^{-1}}$ and masses $\geq 10^{14} M_{\odot}$ to be 2.76×10^{-8} at z=0.489. We conclude that either 1E0657-56 is incompatible with the concordance ΛCDM universe, or the initial conditions suggested by the non-cosmological simulations must be revised to give a lower value of v_{12}.

2.1 Introduction

It is widely believed that the structure formation in our Universe is largely driven by the gravity of dark matter. Therefore it is worthwhile to probe dark matter dynamics through measurements of galaxy peculiar velocities and constrain our cosmological model by comparing against numerical simulations. In fact there has been extensive work along these lines, recovering the local density field from the measured velocity field (Bertschinger & Dekel, 1989; Davis et al., 1996; Willick et al., 1996). Unfortunately the observations of peculiar velocity fields contain large uncertainties, and accurate determination of the cosmological mass density parameter Ω_{m} turned out to be difficult using this method.

More recently, clusters of galaxies have been used to prove the existence of dark matter itself, thanks to accurate measurements of projected dark matter density using weak and strong lensing techniques. Some clusters show signs of a cluster-cluster merger, where the baryonic component and collisionless dark matter show different spatial distributions, strongly supporting the existence of dark matter. Furthermore, using the shock features seen in the gas, one can infer the collision velocity of two galaxy clusters (Clowe et al., 2004, 2006; Bradač et al., 2006). These new observations have brought renewed interest to dark matter dynamics and using it to check the

standard Λ cold dark matter (ΛCDM) cosmological model (Efstathiou et al., 1990; Ostriker & Steinhardt, 1995).

In particular, the observations of the massive cluster of galaxies 1E0657-56 seem to suggest a much higher relative dark matter halo velocity than one would expect in the ΛCDM model. This system includes a massive sub-cluster (the "bullet") with $M_{\rm bullet} \simeq 1.5 \times 10^{14} M_{\odot}$ that has fallen through the parent cluster of $M_{\rm parent} \simeq 1.5 \times 10^{15} M_{\odot}$ roughly 150 million years ago, and is separated by $\simeq 0.72\,{\rm Mpc}$ on the sky at an observed redshift of z=0.296 (Clowe et al., 2004, 2006; Bradač et al., 2006). The uniqueness of this system comes from the collision trajectory being almost perpendicular to our line of sight. This provides an opportunity to better study the dynamics of large cluster collisions. The Chandra observations revealed that the primary baryonic component had been stripped away in the collision and resided between the two clusters in the form of hot X-ray emitting gas (Markevitch, 2006). This provides strong evidence for the existence of dark matter (DM); As the two clusters passed through each other, the baryonic components interacted and slowed down due to ram pressure, while the dark matter component was allowed to move ahead of the gas since it only interacts through gravity without dissipation. One can infer the velocity of the bow shock preceding the 'bullet' using the shock Mach number and a measurement of the pre-shock temperature. The inferred shock velocity was found to be $v_{\rm shock} = 4740^{+710}_{-550}\,{\rm km\,s^{-1}}$ (Markevitch, 2006).

Hayashi & White (2006) examined the Millennium Run (Springel et al., 2005b) in search for such a sub-cluster moving with a velocity relative to its parent cluster of $v_{\rm bullet} = 4500^{+1100}_{-800}$ km s^{-1} (Markevitch et al., 2004). Due to the limited volume of the simulation (500 h^{-1}Mpc)^3, few halos had masses comparable to 1E0657-56. Still they estimated that about 1 in 100 have velocities comparable to the bullet cluster, and concluded that the event is not impossible within the current ΛCDM model.

It is often assumed that the inferred shock velocity is equal to the velocity of

the dark matter 'bullet' itself. Several groups have shown, however, that this is not necessarily true through the use of non-cosmological hydrodynamic simulations. Milosavljević et al. (2007) used two dimensional simulations to find that the subcluster's velocity differed from the shock velocity by about 16%, bringing the relative velocity of DM halos down to $\sim 3980\,\mathrm{km\,s^{-1}}$. They assumed a zero relative velocity at a separation distance of 4.6 Mpc for their initial conditions. They also emphasized that their conclusion is sensitive to the initial mass and gas density profile of the two clusters. Springel & Farrar (2007) was able to reproduce the inferred shock velocity through the use of an idealized three dimensional hydrodynamic simulation with initial conditions that assumed a relative velocity of $2057\,\mathrm{km\,s^{-1}}$ at a separation distance of 3.37 Mpc, and found that the subcluster was moving with a relative speed of only $\sim 2600\,\mathrm{km\,s^{-1}}$ just after the collision. Mastropietro & Burkert (2008) argued that Springel & Farrar (2007) failed to reproduce the observed displacement of X-ray peaks that represent an important indicator of the nature of the interaction. In their simulations they found that in order to reproduce the observational data of 1E0657-56 a relative halo infall velocity of $\sim 3000\,\mathrm{km\,s^{-1}}$ at an initial separation distance of 5 Mpc was required.

Similar to previous work by Hayashi & White (2006), Lee & Komatsu (2010) quantified the likelihood of finding bullet-like systems in the large cosmological N-body simulation MICE (Crocce et al., 2010). They examined DM halos at z=0.0 & 0.5, searching for a halo pair matching the initial conditions of Mastropietro & Burkert (2008). They concluded that ΛCDM is excluded by more than 99.91% confidence level at z=0. Their results at z=0.5 are inconclusive due to limited statistics. However, by fitting their pairwise velocity probability distribution function to a Gaussian distribution, they were able to estimate the probability of finding a pair with $v_{12} > 3000$ km s^{-1} to be 3.6×10^{-9} and $v_{12} > 2000$ km s^{-1} to be 2.2×10^{-3} at z=0.5. They did warn that one must be careful about this approach since they are probing the tail of

the distribution where their fits may not be accurate.

Most recently Forero-Romero et al. (2010) approached the problem from a different perspective. They studied data from the MareNostrum Universe (Gottlöber & Yepes, 2007) which contains baryonic matter in addition to collisionless DM. Instead of examining the pairwise velocities of DM halo pairs, they concerned themselves with the physical separation between the dominant gas clump and its predominant DM structure. They argued that their approach provides a more robust comparison to observation; deriving the relative velocity from the observations includes statistical and systematic uncertainties whereas the separation uncertainty is dominated by statistical errors in the measuring process. Additionally they point out that current simulations do not include the proper prescriptions for cooling, star formation, or feedback which implies that their predictions of the detailed X-ray properties of hot gas in massive halos are not robust. Using their method they found that large displacements between gas & DM are common in ΛCDM simulations therefore, 1E0657-56 should not be considered a challenge.

In this paper, we take a similar approach to that of Lee & Komatsu (2010), and examine large ΛCDM N-body simulations to see how common these high relative velocities are among massive DM halos. One of the things that the earlier works have not performed is an examination of resolution and box size effect. Therefore we first conduct a study to determine the effects of increasing resolution or varying box sizes on the parameters of interest. We then examine our largest simulation in search for a pair matching the initial conditions required by Mastropietro & Burkert (2008) to reproduce the observed properties of 1E0657-56.

The rest of the paper is organized as follows: Section 2.2 discusses simulation parameters, Section 2.3 shows the simulation results and examines the distribution of parameters relevant to this study, such as halo masses, pairwise velocity, and pair separation distances. Section 2.4 examines the simulation results at earlier redshifts

of z=0.296 & z=0.489, and how they relate to the bullet system. Finally, Section 2.5 contains concluding remarks and discussion of future prospects.

2.2 Simulations

For our simulations we use the GADGET-3 code (originally described in Springel, 2005) which simulates large N-body problems by means of calculating gravitational interactions with a hierarchical multipole expansion. It uses a particle-mesh method (Hockney & Eastwood, 1981; Klypin & Shandarin, 1983; White et al., 1983) For long-range forces and a tree method (Barnes & Hut, 1986) for short-range forces.

Cosmological parameters consistent with the cosmological constraints from the Wilkinson Microwave Anisotropy Probe (WMAP) data and an Eisenstein & Hu (1998) transfer function were employed when creating the initial conditions for each simulation with random Gaussian phases: ($\Omega_{\rm m}$, Ω_Λ, H_0, σ_8, n_s)=(0.26, 0.74, 72, 0.8, 1.0) (Komatsu et al., 2009, 2011). We note that we used a value of n_s=1.0 although the best-fit value from the WMAP data is n_s=0.96. Two additional simulations were ran with n_s=0.96 and no differences in their high mass halo pairs were found from the n_s=1 simulations, because the tilt in the primordial power spectrum mostly changes the small scale structures. All simulations contain only collision-less dark matter particles that interact solely through gravity.

Several simulations with varying particle counts and box sizes were ran from z=100 to z=0. The list of simulations along with other parameters can be found in Table 1. Starting with the L250N125 run, the box size and particle count were simultaneously increased (from $L_{\rm box} = 250h^{-1}\,{\rm Mpc}$ to $2016h^{-1}\,{\rm Mpc}$, and from $N = 125^3$ to 1008^3 particles) in order to maintain the same mass resolution and gravitational softening length up until the L2016N1008 run. The second set of simulations were ran to examine the resolution effect. We started with the original L250N125 simulation and increased the particle count and decreased the gravitational softening length while

keeping the box size the same, up to the L250N500 run.

2.3 Data Analysis & Results

2.3.1 Halo Mass Function

DM particles were grouped using a simplified version of the parallel friends-of-friends (FOF) group finder SUBFIND (Springel et al., 2001). The code groups the particles into DM halos if they lie within a specified linking length (FOF LL). This linking length is a fraction of the initial mean inter-particle separation, for which we adopt a standard value of b=0.2. In order to be considered a halo it must also contain at least 32 particles.

Figures 1 and 2 show DM halo mass functions in our simulations. Both figures include the Sheth & Tormen (1999) mass function (ST) plotted as a black dotted line. Recent work by More et al. (2011) found that the commonly used value of b=0.2 selects a significantly larger local overdensity ($\delta_{\rm FOF}$) than previously thought. Normally it is assumed that b=0.2 results in $\delta_{\rm FOF} \approx 60$ (corresponding to the enclosed overdensity of $\delta \sim 180$), but their study finds that it results in $\delta_{\rm FOF} \approx 80.61$ which is a $\sim$35% increase. We find that our mass function is slightly higher than the ST mass function on all mass scales. By regrouping the L1000N500 sim using b=0.1 we under-predict the number density on all mass scales, as shown by the solid magenta line in Figures 1 & 2. Changes in b certainly have a significant impact on the halo mass function.

Figure 1 shows that the number of high mass halos increases by increasing the box size from 250 h^{-1}Mpc to 2016 h^{-1}Mpc while maintaining the same resolution. The lowest mass halo in all simulations shown in Figure 1 is $M_{\rm halomin}$=$1.84 \times 10^{13} h^{-1} M_{\odot}$. The run with the largest box size (L2016) shows a slight shortage in the number of low mass halos around $M_{\rm halo} \simeq 10^{13.24} - 10^{14.20} h^{-1} M_{\odot}$ when compared to the other three runs with smaller box sizes. The most likely explanation for this shortage is

that the lower mass halos were absorbed into higher mass halos.

Higher resolution runs can resolve larger number of low mass halos as seen in Figure 2. The least massive halo for the highest resolution simulation (L250N500) has $M_{\rm halomin}$=$2.87 \times 10^{11} h^{-1} M_{\odot}$, which is roughly two orders of magnitude lower than the lowest mass halos found in Figure 1.

While searching for a bullet-like pair of halos with masses on the order of $M_{\rm bullet}$ & $M_{\rm parent}$, Figures 1 & 2 indicate that it is possible to form such massive halos in box sizes as small as 250 h^{-1}Mpc at z=0 but there will be a low number of them.

2.3.2 Pairwise Velocity Function

In this section, we present the results on the pairwise velocity ($v_{12} = |\vec{v}_1 - \vec{v}_2|$) function, i.e., the number of halo pairs within a velocity bin per unit volume (dn/dv_{12}). Figures 3 & 4 show dn/dv_{12} with four panels for different simulation runs, each panel containing three lines for halo pairs with a separation distance of less than $d_{12} = 2, 5,$ & 10 Mpc.

Figure 3 shows that increasing the box size with a fixed resolution allows for a greater number of high v_{12} pairs, but with greater separation distances. Doubling the box size from L250 to L500 yields only a small increase in high v_{12} pairs. Doubling it again to L1000 gives us a considerable jump in high v_{12} pairs with separation distances of 5< d_{12} <10 Mpc, while the 2< d_{12} <5 Mpc range only sees a moderate increase. Doubling the box size one final time to L2016, we again only see a moderate increase in v_{12} similar to going from the L250 to L500 sim. The number of close halo pairs with d_{12} <2 Mpc seem to remain fairly constant with relatively low v_{12} throughout changes in the box size. This implies that increasing the box size does not increase v_{12} for pairs within 2 Mpc of one another.

By increasing the resolution, the number of halo pairs with high v_{12} increases (Figure 4), but unlike the case of enlarging the box, this does not necessarily come

at the cost of increased separation distances. Each increase in resolution gives us a larger number of low and high v_{12} pairs on all distance scales. When compared to Figure 3, the simulations shown in Figure 4 are better at resolving smaller structures and length scales, leading to larger values of v_{12}. Unfortunately this data does not give us any information on the mass of the halos pairs, so increasing the resolution in order to increase the number of close high v_{12} pairs may not be beneficial when searching for high mass pairs such as 1E0657-56.

2.3.3 Relative Halo Velocity & Halo Mass

It is useful to study the effects of different box sizes and resolutions on the average mass of a halo pair vs. v_{12}. Figure 5 shows how increasing the box size with a constant resolution increases the number of low-mass, high v_{12} halo pairs, along with increasing the number of high-mass, high-v_{12} pairs to a lesser degree. As the box size increases, we are allowing for a greater number of rare high v_{12} halo pairs which probe the tail of the distribution.

Figure 6 shows that an increase in the resolution results in a larger number of low-mass, high-v_{12} pairs, and a less substantial increase in the number of high-mass, high-v_{12} pairs. Increasing the box size yields high v_{12} pairs with increasing mass, while increasing the resolution yields a larger number of high v_{12} pairs at the maximum halo mass allowed by the box.

2.3.4 Cumulative v_{12} Function

To examine how the box size and resolution affects the actual number of high v_{12} halo pairs, we plot the cumulative v_{12} distribution function as shown in Figures 7 & 8. Changing the box size (Figure 7) extends the curve to higher v_{12}. The larger box and particle count result in better statistics, which allows us to probe the high velocity tail of the v_{12} distribution as mentioned in the previous section.

By increasing the resolution alone (Figure 8), we see that the normalization of the cumulative v_{12} distribution function becomes higher due to larger number of lower mass halos. These figures suggest that by increasing the box size and/or resolution one would be able to produce a halo pair with a greater v_{12}, however, as we saw earlier in Figures 5 & 6, the majority of high-v_{12} pairs have lower average masses than 1E0657-56.

2.4 Results at Earlier Redshifts

To be fully consistent with the observations of 1E0657-56, comparing our simulations at the same redshift as 1E0657-56 would be ideal. Up until this point, we have examined only simulation data at z=0, yet 1E0657-56 is observed at z=0.296. This difference in time of $\sim$3.31 billion years can have a considerable impact on the velocities, sizes, and separation distances of the DM halos contained in the simulation. Another problem arises when we consider how we group the DM particles. At z=0.296 the separation between the two halos of 1E0657-56 is $d_{12} \simeq 0.72\,\mathrm{Mpc}$, which is larger than the linking lengths listed in Table 1 (0.1-0.4 Mpc) for each of our simulations. At first glance it may appear that we could identify each halo independently within our sims, but when one considers their large masses, we find that this is not the case. The virial radius of each halo is found to be 1.42 & 3.06 Mpc for the 'bullet' ($M_{\mathrm{bullet}} \simeq 1.5 \times 10^{14} M_{\odot}$) and its 'parent' ($M_{\mathrm{parent}} \simeq 1.5 \times 10^{15} M_{\odot}$), respectively. When two halos of this size are separated by $\simeq$0.72 Mpc, they will easily overlap, resulting in the FOF group finder identifying them as a single halo at the observed redshift of z=0.296. If we assume the separation distance of 5 Mpc and infall velocity of $3000\,\mathrm{km\,s^{-1}}$ as required by Mastropietro & Burkert (2008) to reproduce the observed quantities of 1E0657-56, then a halo pair in this initial configuration should be found at z=0.489.

2.4.1 Peculiar Velocities

Before we examine the simulation at z=0.489, we first compare our simulations to the prediction of linear theory for further validation. Linear theory predicts that for an Einstein de-Sitter (EdS) universe the growing mode of the peculiar velocity field grows as $t^{1/3}$. The peculiar velocity of each mode in a non-EdS universe is given by (Peebles, 1980)

$$v_{pec} = \frac{H(z)\, a^2}{4\pi} \frac{dD}{da}, \tag{2.1}$$

where $H(z)$=$H_0 E(z)$ is the Hubble parameter, a is the scale factor, D is the growth factor for linear perturbations, and $E(z)$=$[\Omega_{m,0}(1+z)^3 + (1-\Omega_{k,0}-\Omega_{m,0})(1+z)^2 + \Omega_{\Lambda,0}]^{1/2}$.

The peculiar velocity of each halo in five of our runs was calculated and averaged up to z=10, then compared against the normalized theory curve in Figure 9. Our simulations agree well between z=6 to z=1.0, but start to deviate from the linear theory curve at $z < 1.0$, which is likely due to their virialization.

2.4.2 Pairwise Velocity: Linear Theory

Juszkiewicz et al. (1999) proposed a simple closed-form expression relating the mean relative velocity of pairs of galaxies at a fixed separation to the two-point correlation function of mass density fluctuations:

$$-\frac{v_{12}}{Hr} \approx \frac{2}{3} f \bar{\bar{\xi}} \left[1 + \alpha \bar{\bar{\xi}}\right], \tag{2.2}$$

where H is the Hubble parameter, $r = ax$ is the proper separation, $f \equiv d\ln D / d\ln a$, $\alpha \approx 1.2 - 0.65\gamma$, γ is the logarithmic slope of the correlation function, $\bar{\bar{\xi}} = \bar{\xi}/\left[1+\xi\right]$, $\bar{\xi} = 3x^{-3}\int_0^x \xi y^2 dy$, and ξ is the two point correlation function. At z=0, the value of f is $\simeq$0.5, and then it asymptotes to unity at $z \gtrsim 8$.

To obtain theoretical results based on Eq. (2.2) that can be compared with our

simulations, we calculate ξ by correlating the center-of-mass positions of halos with a random data set and use the Landy & Szalay (1993) estimator

$$\xi(r)_{\rm halo} = \frac{DD - 2DR + RR}{RR}, \tag{2.3}$$

where DD, DR, & RR represents halo pair counts for Data-Data, Data-Random, & Random-Random data sets at a given value of r. The result of $\xi(r)_{\rm halo}$ for the L250N500 sim is plotted in Figure 10. Higher values of $\xi_{\rm halo}$ correspond to a larger probability that another halo lies at a separation of r. The value of $\xi_{\rm halo}$ decreases with increasing r, implying that halos tend to cluster more on smaller scales. The value of $\xi_{\rm halo}$ also decreases with increasing redshift, meaning halos are less clustered in the earlier universe.

To compare our simulation with Eq. (2.2), we calculated the average pairwise halo velocities $\langle v_{12} \rangle$ for pairs residing within physical shells of 1 Mpc thickness (± 0.5 Mpc) around r=1, 3, 5, & 10 Mpc for the L250N500 run. The results are shown in Figure 11, where the solid curves represent simulation data, the dashed curves correspond to the theoretical predictions of Eq. (2.2) using ξ-values from Figure 10, and the different colors distinguish between different values of r. Juszkiewicz et al. (1999) did not consider the effect of galaxy bias relative to dark matter, and without any correction, we find that $\langle v_{12} \rangle$ of halos in our simulation are somewhat higher than those predicted by Eq. (2.2). Therefore we invoke an ad hoc correction factor of $\times 1.5$ to account for this effect, and the dashed lines in Figure 11 include this multiplication factor in the right-hand-size of Eq. (2.2). After this correction, our simulation agrees with Eq. (2.2) very well for $r = 3$ & 5 Mpc, but there is some deviation from theory for the $r = 1$ & 10 Mpc results. The shape of the theory curve is determined by the competition between increasing $H(z)$, decreasing ξ, and increasing f with increasing redshift.

Fukushige & Suto (2001) examined the validity and limitations of the stable con-

dition ($-v_{12}/Hr = 1$), which states that the mean physical separation r of galaxy pairs is constant on small scales. They found a significant time variation in the mean pairwise peculiar velocities and argued that this behavior was not due to a numerical artifact, but a natural consequence of the continuous merging process. This irregular oscillatory behavior could be reduced by averaging over cosmological volumes larger than 200 Mpc^3, resulting in a more accurate estimate of the mean pairwise velocity. Our data is also consistent with Fukushige & Suto (2001) (dashed cyan line in Figure 11) in that the oscillatory behavior is suppressed due to our cosmological volume being greater than 200 Mpc^3, and their result for r=1.52 Mpc lies between our r=1 & 3 Mpc curves.

2.4.3 In Search of the 'Bullet'

Hereafter we will only be examining our largest simulation (L2016N1008) at redshifts of z=0.0, 0.296, and 0.489. In Figure 12, we show the redshift evolution of the pairwise velocity function (dn/dv_{12}) from z=0 to z=0.489. Qualitatively this plot changes very little with redshift, except that there is a slight increase in the number of pairs at the highest end of the v_{12} distribution. Pairs within separation distances of $d_{12} < 2$ Mpc have maximum v_{12} on the order of $\simeq$1800 km s^{-1} at z=0.296 and z=0.489. For pairs with greater d_{12}, the maximum v_{12} reaches as high as $\simeq$3300 km s^{-1}.

In Figure 13, we show the redshift evolution of the average halo mass vs. their pairwise velocity. One can see the effect of halo mergers, and the number of high-mass halo pairs with $\langle M_{\rm halo} \rangle > 10^{15} M_\odot$ are increasing from z=0.489 to z=0. The cyan dashed lines in the z=0.489 panel illustrate the average pair mass of 1E0657-56 ($8.25 \times 10^{14} M_\odot$) and initial pairwise velocity of $v_{12} \approx 3000\,{\rm km\,s^{-1}}$ required by Mastropietro & Burkert (2008). Two pairs are found in our simulation near the region of interest, but their masses and velocities are still too low.

2.4.3.1 Candidate Halo Pairs

Table 2 lists the five halo pairs with highest $\langle M_{\rm halo} \rangle$ for z=0, z=0.296, and z=0.489. A simulation of this size (comoving $2\,h^{-1}$Gpc) produces many halo pairs massive enough to match that of 1E0657-56 at the examined redshifts. While the separation distances of these pairs may be in the range we are interested in, the pairwise velocities are too low to match the required v_{12}=3000 km s^{-1} by Mastropietro & Burkert (2008).

Table 3 lists the five halo pairs with the highest v_{12} at the three examined redshifts. All halo pairs in this table match or exceed the required v_{12} of 3000 km s^{-1}, but they miss the mark when it comes to the other observables of 1E0657-56. All of the halos in this table have masses one or two orders of magnitude lower than $M_{\rm bullet}$ & $M_{\rm parent}$. The mass ratios are also a bit high; the lowest being $\sim$0.3 at z=0.489 compared to 0.1 for 1E0657-56 at z=0.296. None of the collision angles are head on, yet most are highly inclined. Lastly the separation distance of each pair at z=0.489 is somewhat large; Mastropietro & Burkert (2008) set their initial separation at proper 5 Mpc while each pair in this table is separated by >7.5 Mpc.

2.4.3.2 Simulation Requirements to Produce the 'Bullet'

In Figures 7 & 8, we examined the cumulative v_{12} distribution, however these figures included a large number of low-mass halos which are of little interest to this study. Therefore in Figure 14, we restrict the halo sample to those with masses greater than $10^{14} M_{\odot}$ at z=0, z=0.296, & z=0.489. With increasing redshift we see a decrease in the total number density of halo pairs above $10^{14} M_{\odot}$.

Assuming that the trend of the cumulative v_{12} function would continue to higher velocities with increasing box size (as was the case for z=0 shown in Figure 7), we can fit a line to the z=0.489 curve and estimate the box size and particle count required to produce at least one halo pair with a specified v_{12}. A quadratic of the form $y = y_0 + ax + bx^2$ was fit to the z=0.489 curve between the values of v_{12}=800$-$1500 km s^{-1},

and we obtain the best fit values of y_0=−3.97, a=-3.31×10^{-3}, & b=1.59×10^{-7}. Based on this fit, we estimate the minimum box sizes and particle counts (for the same resolution as the L2016N1008 run) required to produce at least one halo with the initial velocities given by Mastropietro & Burkert (2008), and Springel & Farrar (2007). The result is listed in Table 4.

Our result suggests that we would need a simulation box size of $(4.48h^{-1}\mathrm{Gpc})^3$ & 2240^3 DM particles in order to produce at least one halo pair with an average mass greater than $10^{14}M_\odot$ and $v_{12} > 3000\,\mathrm{km\,s^{-1}}$ at z=0.489. The exact values of the required box size and particle count is somewhat sensitive to the range of v_{12} used for the fit, therefore the values listed in Table 4 should be taken as a rough estimate. The required simulations are so large and they would take significant computational resources which is currently not feasible for us.

2.4.3.3 Probability of Finding the 'Bullet'

We also examine the probability distribution function (PDF) of v_{12} for halos with $\langle M_{\mathrm{halo}}\rangle > 10^{14}M_\odot$. We perform a least square fit to the data using a skewed normal distribution (Azzalini & Capitanio, 2009), and calculate the probability of finding a halo pair with $v_{12} > 3000\,\mathrm{km\,s^{-1}}$ at z=0.489.

In Figure 15, we show the binned PDF data with blue circles, and the best-fit skew normal distribution as the red curve. By integrating the PDF from $v_{12} = 3000\,\mathrm{km\,s^{-1}}$ to infinity, we calculate the probability of finding a halo pair with masses greater than $10^{14}\,M_\odot$ and $v_{12} > 3000\,\mathrm{km\,s^{-1}}$ to be $P(> 3000\,\mathrm{km\,s^{-1}}) = 2.8 \times 10^{-8}$, which is roughly one order of magnitude higher than calculations done by Lee & Komatsu (2010) (P=3.6×10^{-9}). This very low probability corroborates our earlier finding that it is very difficult to produce a massive halo pair with a high v_{12} matching the required initial configuration suggested by Mastropietro & Burkert (2008).

2.5 Conclusions

We performed many N-Body cosmological simulations with varying box sizes and resolutions in order to examine how changing these parameters affect the search for high-v_{12} halo pairs comparable to the initial conditions required to reproduce the observed properties of the 1E0657-56 system in non-cosmological simulations. Using our largest L2016N1008 run, we examined the pairwise velocities, halo masses, and halo separation distances at z=0.0, 0.296, & 0.489.

We find that the high-v_{12} tail of the distribution extends to a greater velocities as we increase the simulation box size. We also find that the number of high-v_{12} pairs increased as we increase the particle count and resolution with a fixed box size, however, this increase is mostly due to lower mass halos which do not correspond to the characteristics of 1E0657-56. We find that the redshift evolution effect is not very strong for the v_{12} distribution function.

As we show in Table 3, some of the halo pairs have a high relative velocity similar to the initial conditions required to reproduce the observational quantities of 1E0657-56 in non-cosmological simulations, but they are galaxy group-scale halos ($10^{13}-10^{14} M_{\odot}$) and much less massive than the observed estimates for 1E0657-56.

We find that, in N-body simulations with comoving volumes of less than $(2\,h^{-1}\,\mathrm{Gpc})^3$, it is very difficult to reproduce a system that resembles the initial conditions required to reproduce the observational properties of 1E0657-56. Based on the extrapolation of our cumulative v_{12} function, we find that one needs a simulation with a comoving box size of $(4.48\,h^{-1}\,\mathrm{Gpc})^3$ and 2240^3 DM particles in order to produce at least one pair of halos that resembles the initial conditions suggested by Mastropietro & Burkert (2008). In the future it would be useful to run larger simulations (e.g., with $\sim$5 Gpc box and $\sim 2500^3$ particles) to improve the statistics of massive halos.

From the simulated v_{12} PDF of halos, we calculated the probability of finding a halo pair with $v_{12} \geq 3000\,\mathrm{km\,s^{-1}}$ and masses $\geq 10^{14} M_{\odot}$ to be 2.76×10^{-8}, which

is somewhat larger than previous work by Lee & Komatsu (2010). However, both probabilities are quite small and the difference is negligible. These results suggest that a system like 1E0657-56 is currently incompatible with the concordance ΛCDM universe, if its initial condition really requires an initial pairwise velocity of $v_{12} \geq 3000\,\mathrm{km\,s^{-1}}$. As Lee & Komatsu (2010) discussed in detail, there seems to be more systems like 1E0657-56 being observed already, which exacerbates the incompatibility in terms of probability. One other possibility is that there is something wrong with the referred non-cosmological simulations, and the suggested initial v_{12} must be revised to a lower value.

Recent improved observations of 1E0657-56 by Paraficz et al. (2012) have significantly reduced the mass estimates of these two halos. The 'parent' and 'bullet' cluster mass estimates were lowered by $(11 \pm 4)\%$ and $(27 \pm 12)\%$ respectively. Given that these reduced masses still lie well above $10^{14}\mathrm{M}_{\odot}$, our probabilities are not affected. However, non-cosmological hydrodynamic simulations may be able to reproduce the observational quantities of 1E0657-56 with a lower v_{12} given these new estimates, which could in turn ease the tension between theory and observations by altering the required initial conditions needed to reproduce such observations within simulation.

The author would like to thank the co-author of this paper Dr. Kentaro Nagamine for his dedication to detail and insightful discussions.

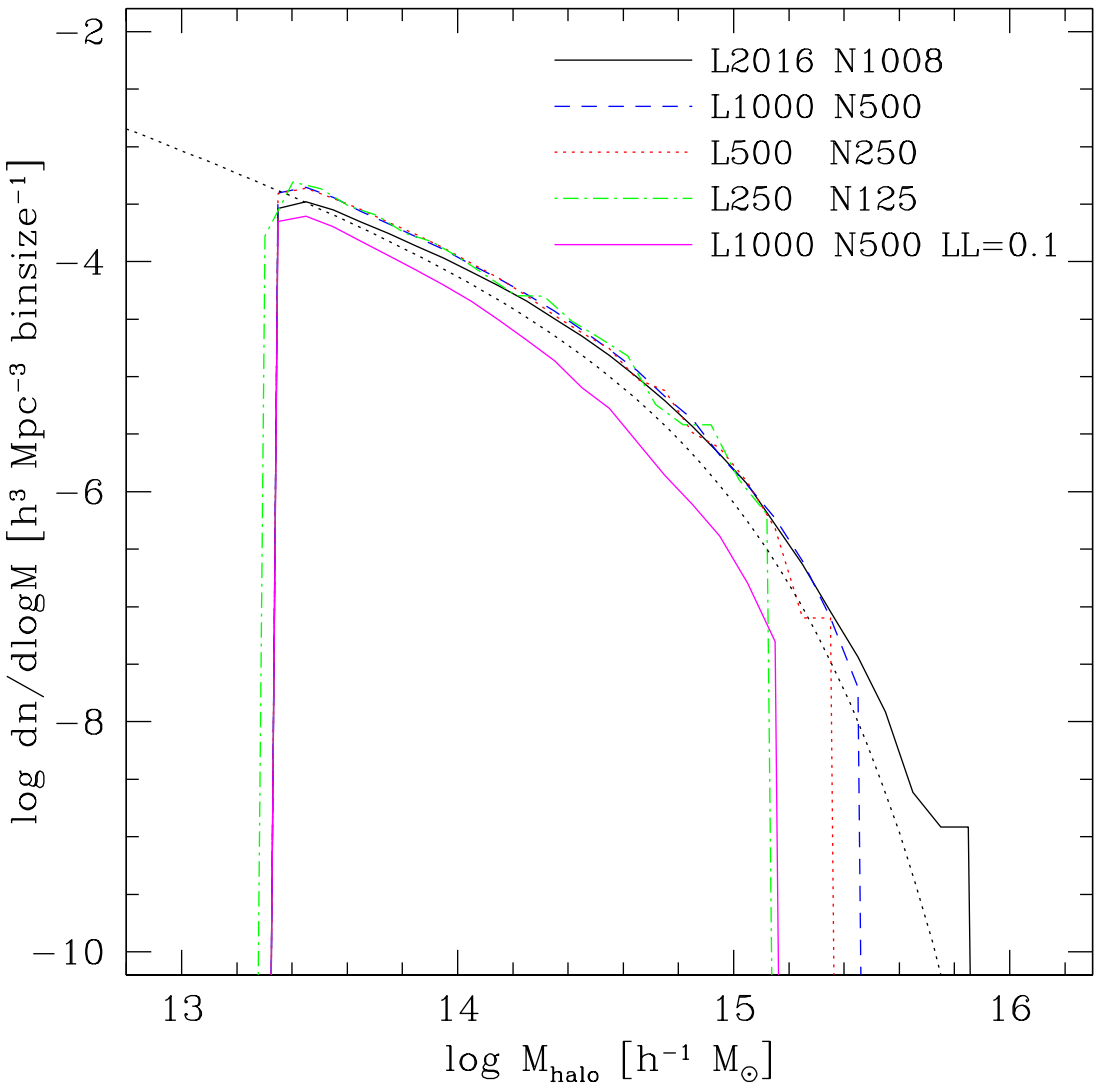

Figure 1 DM halo mass function at z=0. This figure shows the box size effect; how increasing the simulation box size allows for a larger number of high mass halos. The abscissa uses a bin size of $\Delta \log M_{\rm halo}$=0.1. The black dotted line is the ST mass function using the Eisenstein & Hu (1998) transfer function. The solid magenta line is from the 1GpcN500 simulation grouped with a linking length parameter of b=0.1 instead of 0.2.

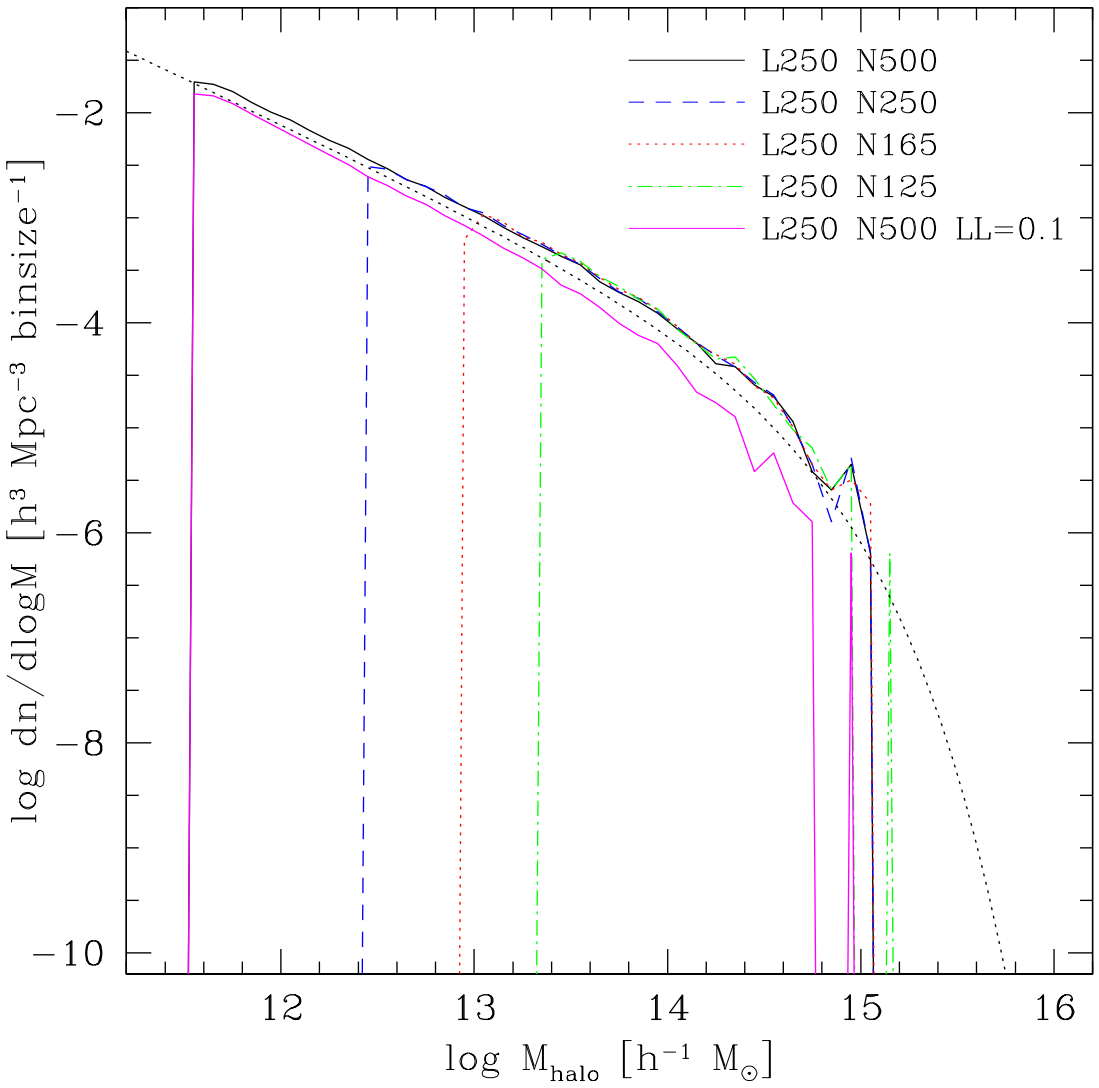

Figure 2 DM halo mass function at z=0. This figure shows the resolution effect; how increasing the resolution of a simulation allows for a greater number of small mass halos. The abscissa uses a bin size of $\Delta \log M_{\rm halo}$=0.1. The black dotted line is the ST mass function using the Eisenstein & Hu (1998) transfer function. The solid magenta line is from the 250MpcN500 run, using a linking length of b=0.1 instead of 0.2.

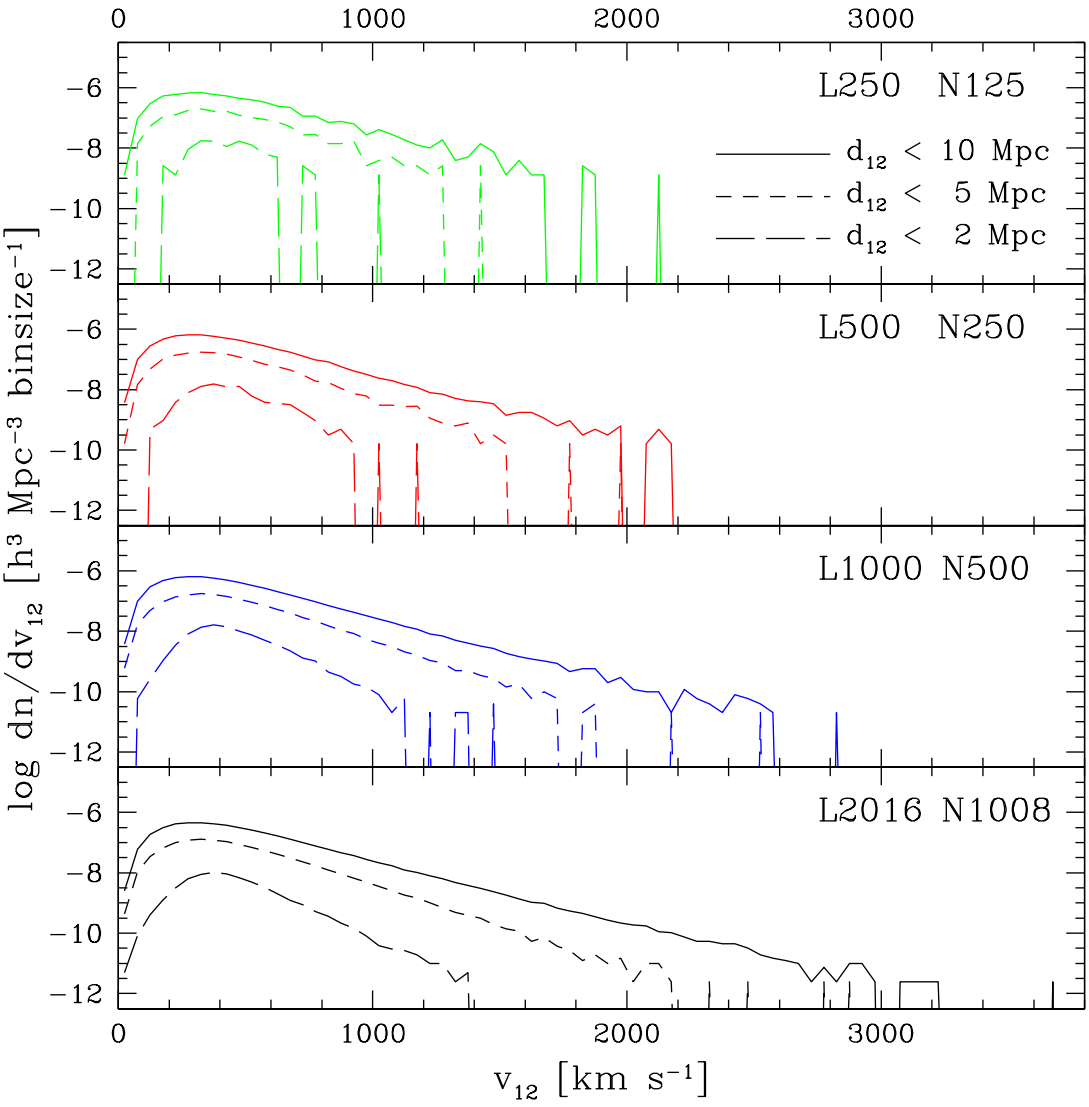

Figure 3 Pairwise velocity function at $z = 0$, demonstrating the box size effect. Each panel contains three lines representing pair separation distances of $d_{12} = 2$, 5, & 10 Mpc. Increasing the box size allows a higher v_{12} for pairs within $d_{12} < 10\,$Mpc, while pairs within $d_{12} < 5\,$Mpc only see a minor increase. Pairs residing within $d_{12} < 2\,$Mpc see the smallest increase in v_{12} as the box size increases.

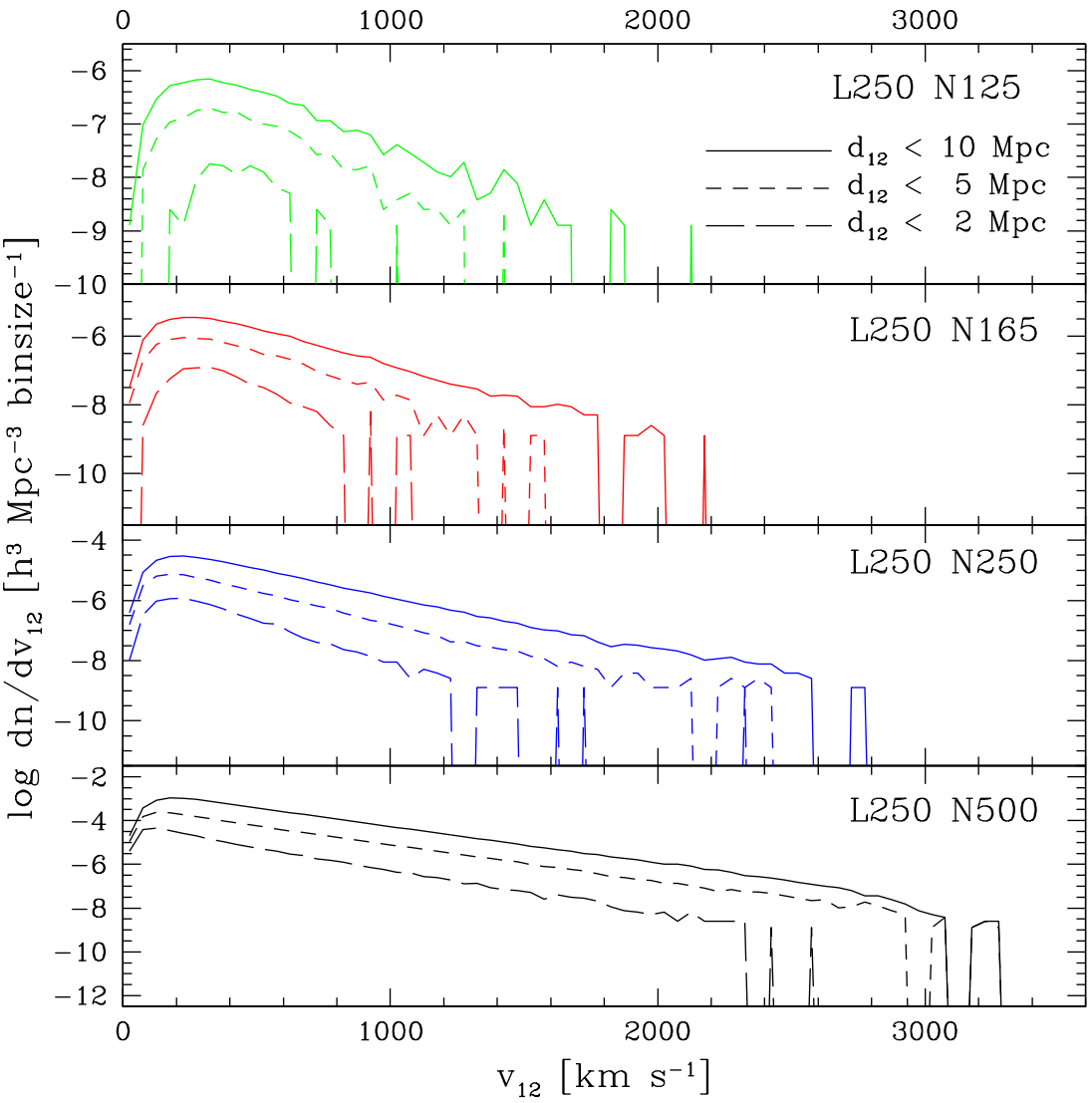

Figure 4 Pairwise velocity function at z=0, demonstrating the resolution effect. Each panel contains three lines representing pair separation distances of d_{12} = 2, 5, & 10 Mpc. Each subsequent increase in resolution allows for smaller structures to be resolved, leading to the increase in v_{12} at all separation distances.

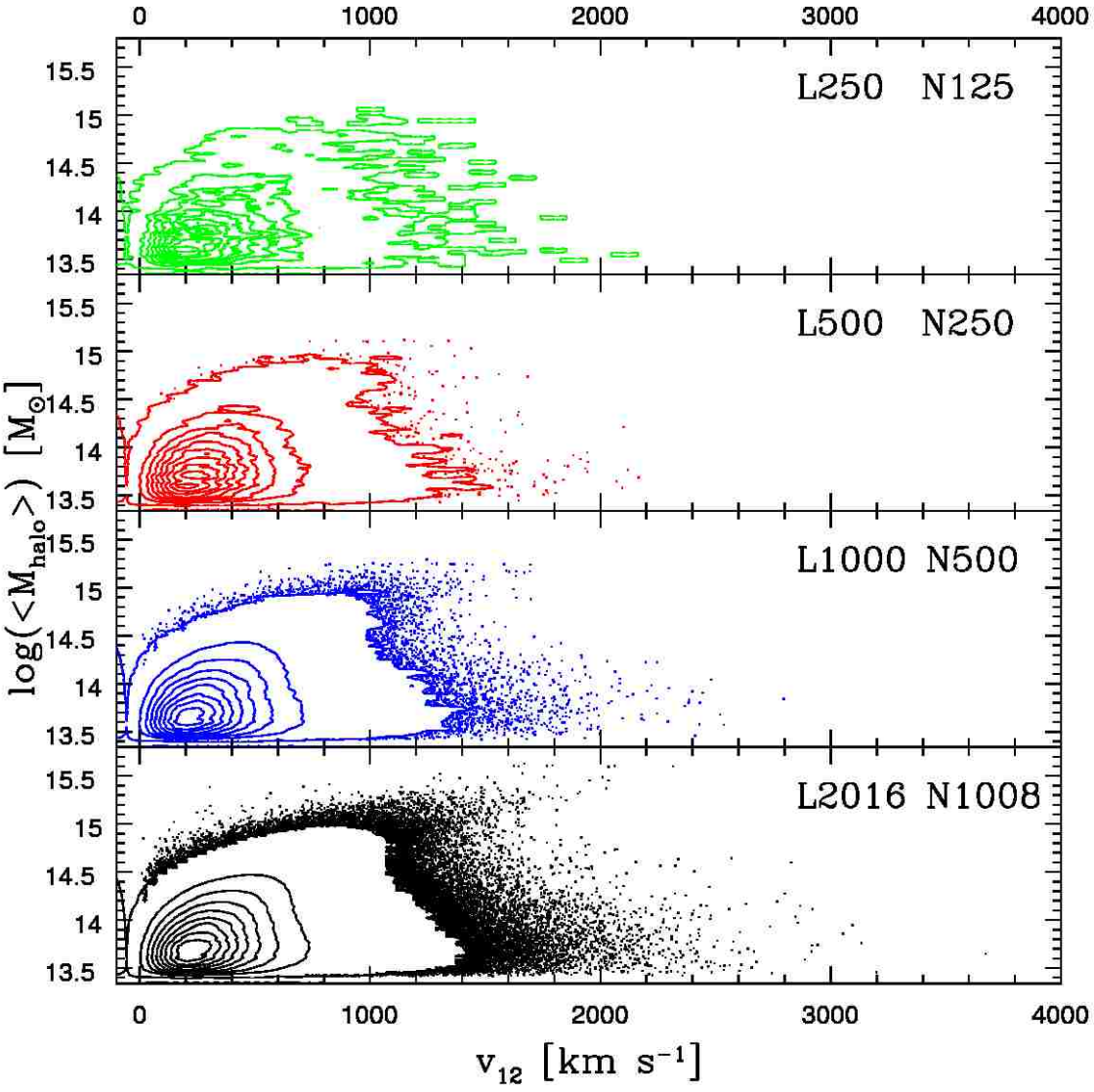

Figure 5 Pairwise velocity vs. average mass of DM halo pairs at z=0. Here we show the box size effect; increasing the simulation box size increases the number of low-mass, high-v_{12} pairs more than the high-mass, high-v_{12} pairs. Each increase in the box size and particle count yields better statistics, broadening the distribution of v_{12}.

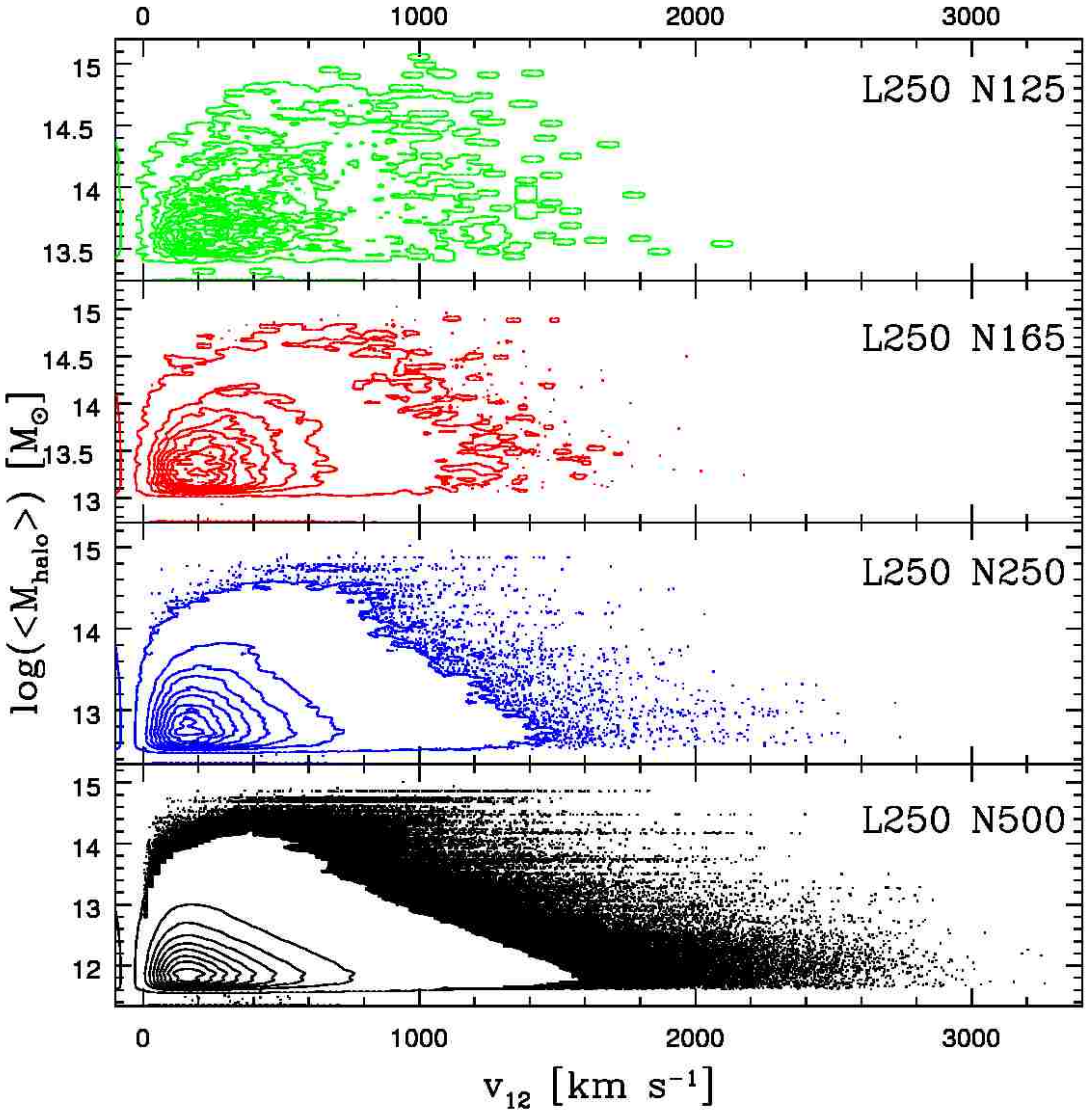

Figure 6 Pairwise velocity vs. average DM halo pair mass at z=0. This illustrates the resolution effect; how increasing the resolution probes lower mass halo pairs. There is a slight increase in high-mass, high-v_{12} pairs, but the majority of the increase is in the low mass halos. As the particle count increases we can resolve smaller structures with higher v_{12}.

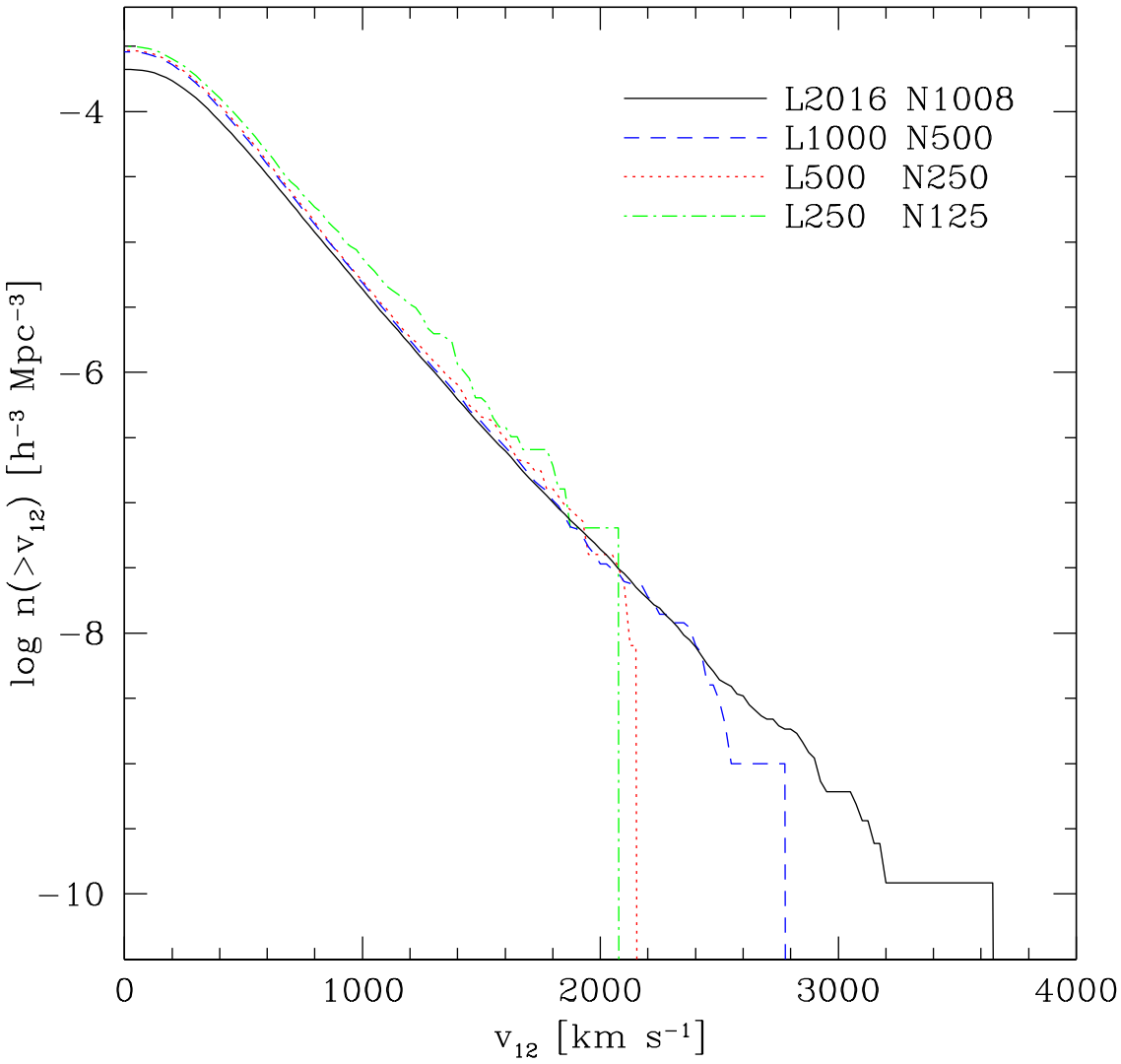

Figure 7 Cumulative v_{12} function of DM halos at z=0. This figure shows how increasing the box size increases the number of high-v_{12} pairs, extending the tail of the distribution.

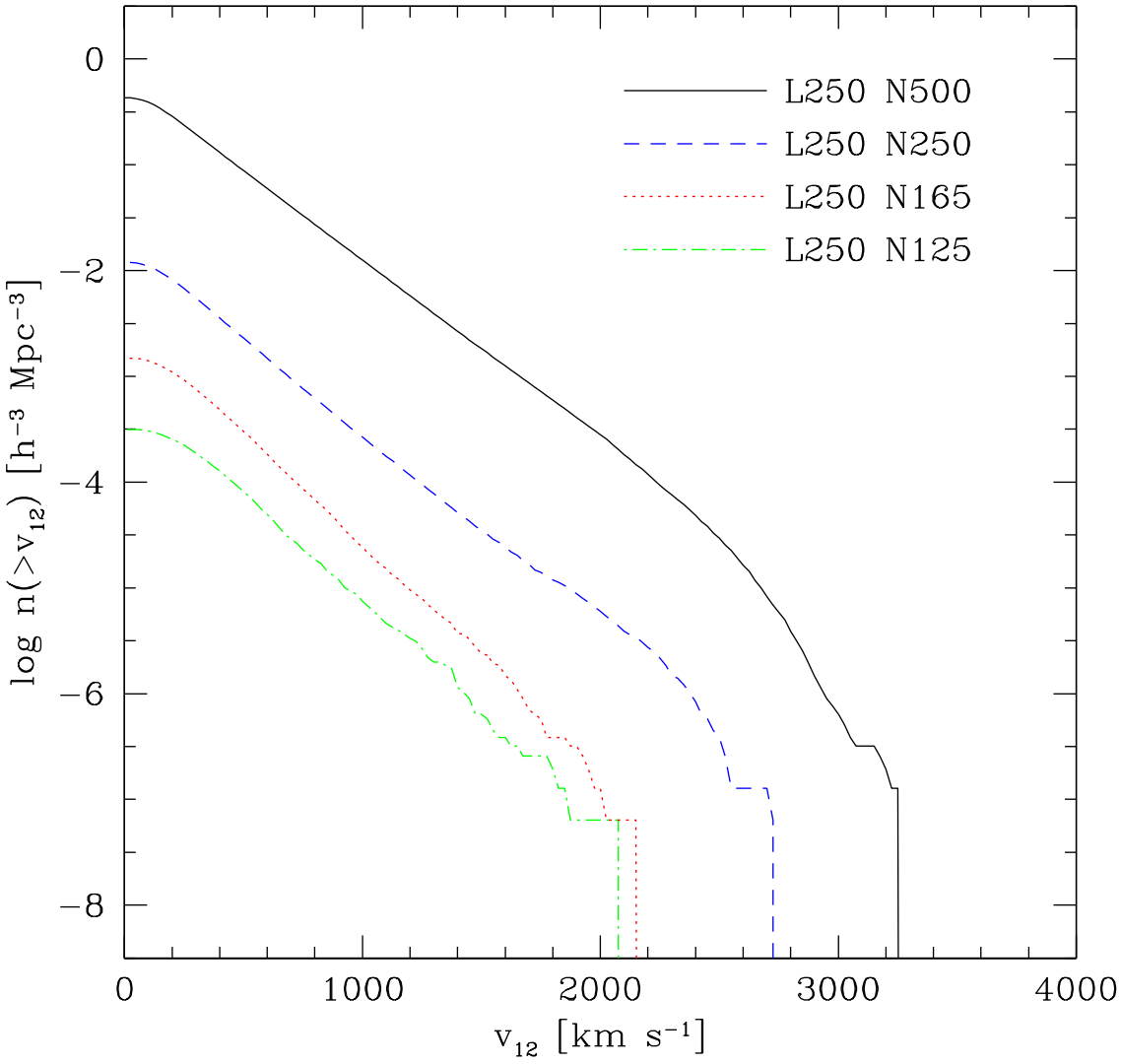

Figure 8 Cumulative v_{12} function of DM halos at z=0. This figure shows the resolution effect. As the resolution increases, the normalization of the distribution increases due to a larger number of lower mass halos with higher velocities.

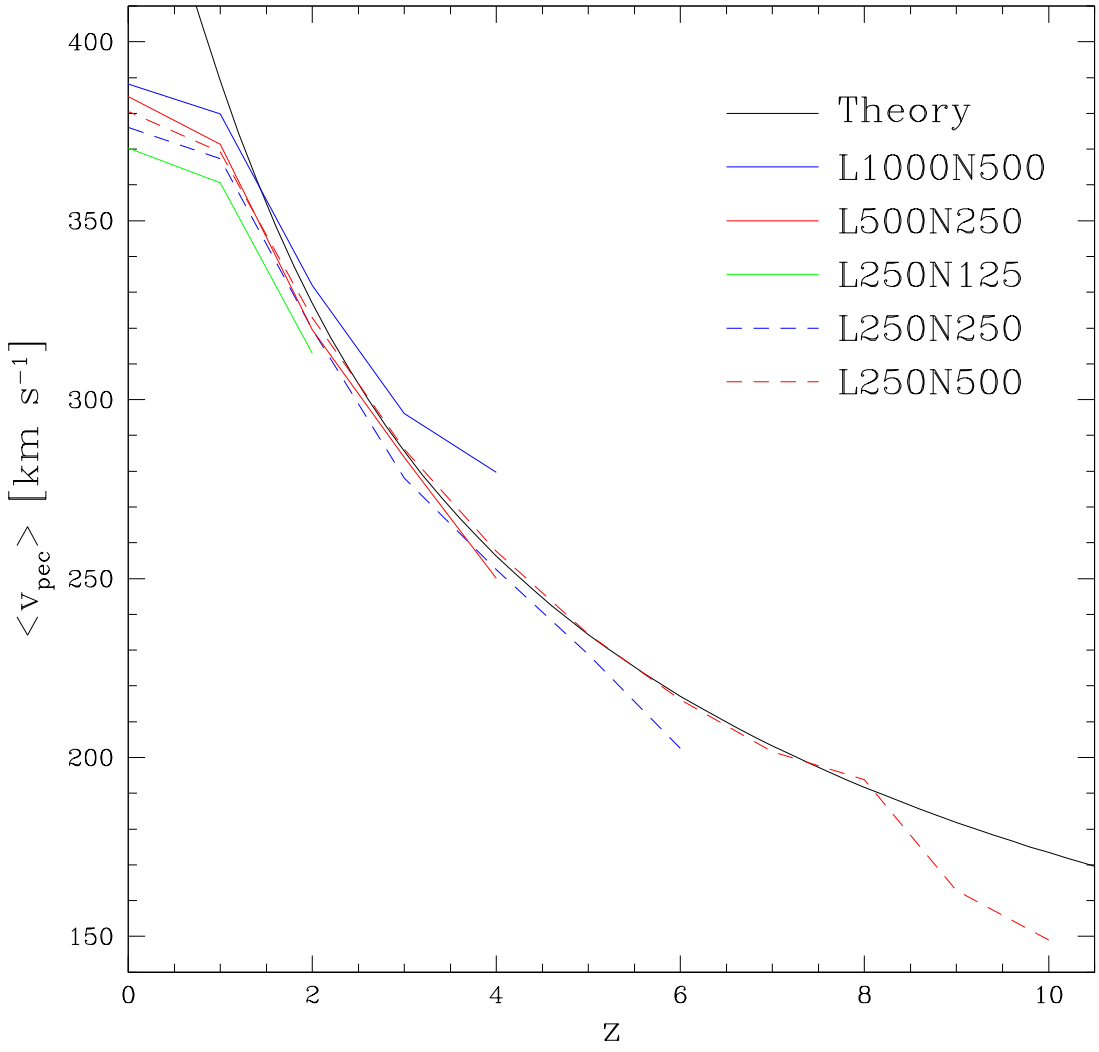

Figure 9 The average halo peculiar velocity of five simulations used in this study, compared with the normalized prediction of linear theory described by Eq. (2.1). The data agrees with theory at $z > 1$, but the velocities begin to level off at $z < 1$, which is likely due to the virialization of the halos.

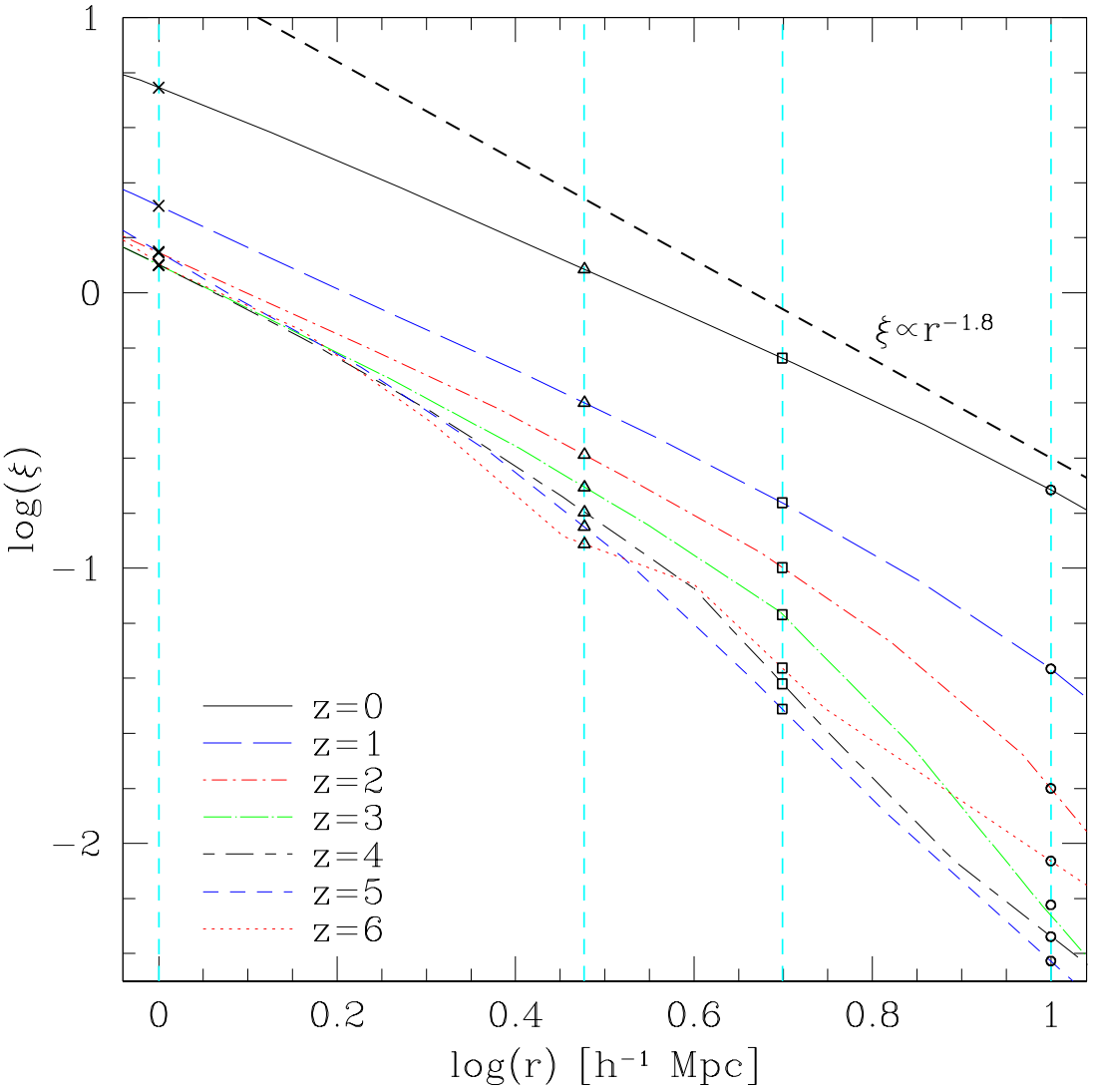

Figure 10 Auto-correlation function of DM halos in the L250N500 run at z=0−6. The vertical cyan dashed lines indicate r=1, 3, 5, & 10 Mpc, where we measure the evolution of ξ as a function of redshift. Symbols lying along these dashed lines represent the ξ-values used in Eq. (2.2) for producing the dashed lines in Figure 11. For comparison, we also show the dashed black line with a slope of $\xi \propto r^{-1.8}$ — the result consistent with the z=0 SDSS galaxies (Zehavi et al., 2010).

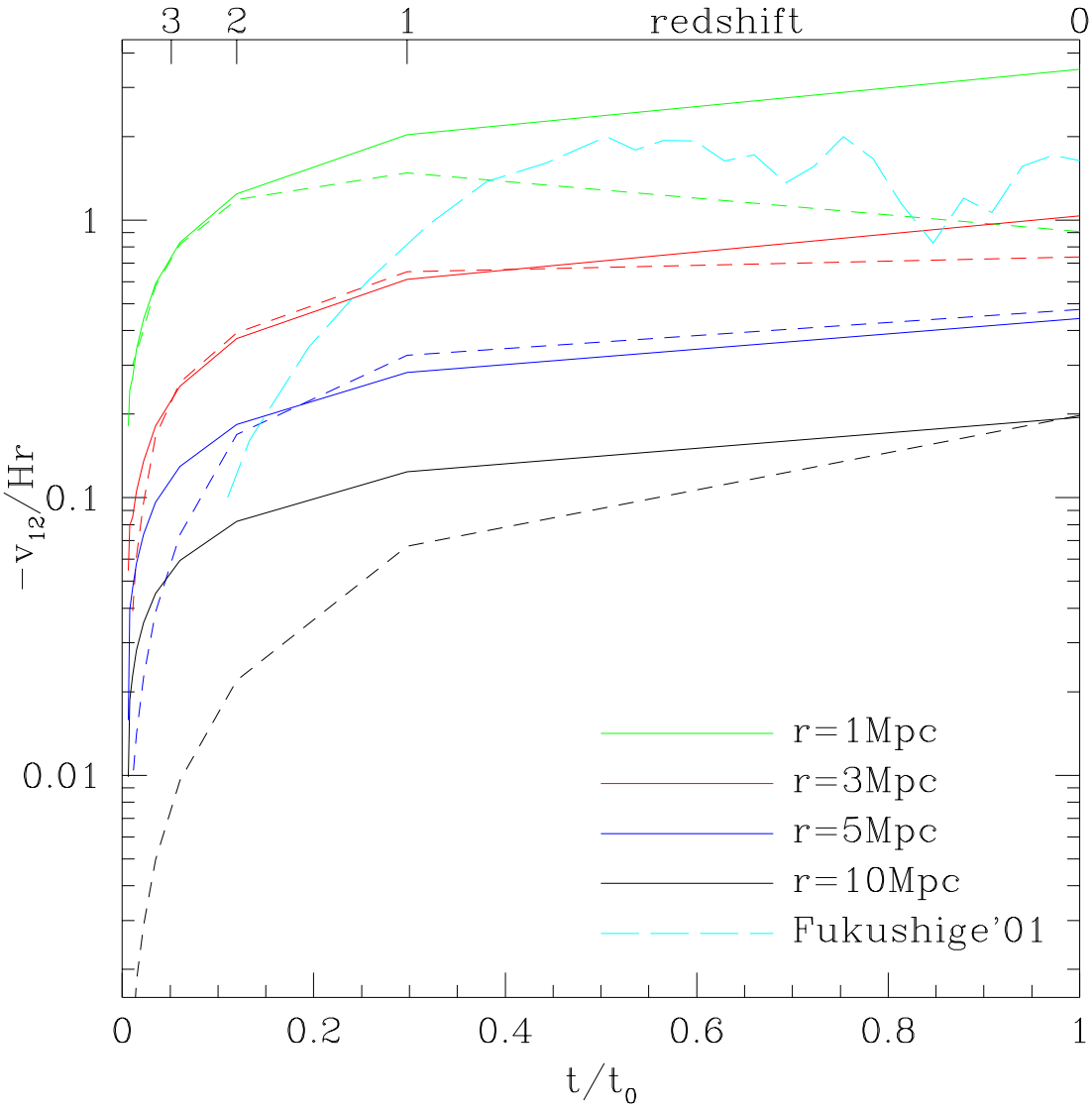

Figure 11 *Solid lines:* Average pairwise halo velocities $\langle v_{12} \rangle$ from the 250MpcN500 run residing in physical shells of 1Mpc thickness with the indicated radii. *Dashed lines:* Theoretical $\langle v_{12} \rangle$ curves given by Equation (2.2) using the ξ values from Figure 10 at each corresponding radius. The dashed cyan line represents data from Fukushige & Suto (2001) at a separation distance of r=1.52Mpc. When these curves reside below unity the Hubble flow is greater than their pairwise velocities, at unity their physical separations remain constant, and above unity their pairwise velocities are greater than the Hubble flow.

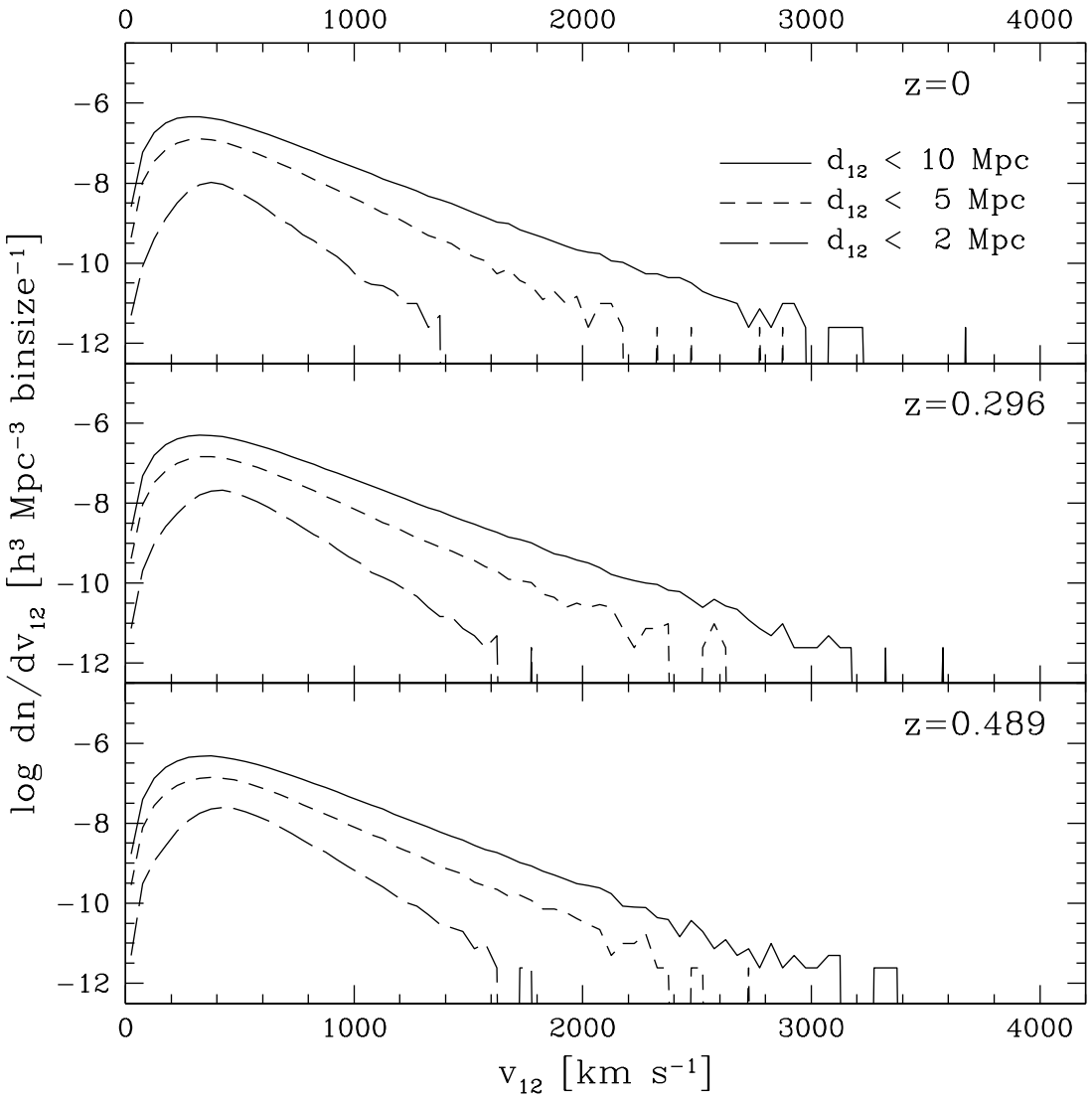

Figure 12 Pairwise velocity function for the L2016N1008 run at z=0.0, 0.296, & 0.489. There is a slight increase in the number of pairs at the highest end of the v_{12} distribution as the redshift increases.

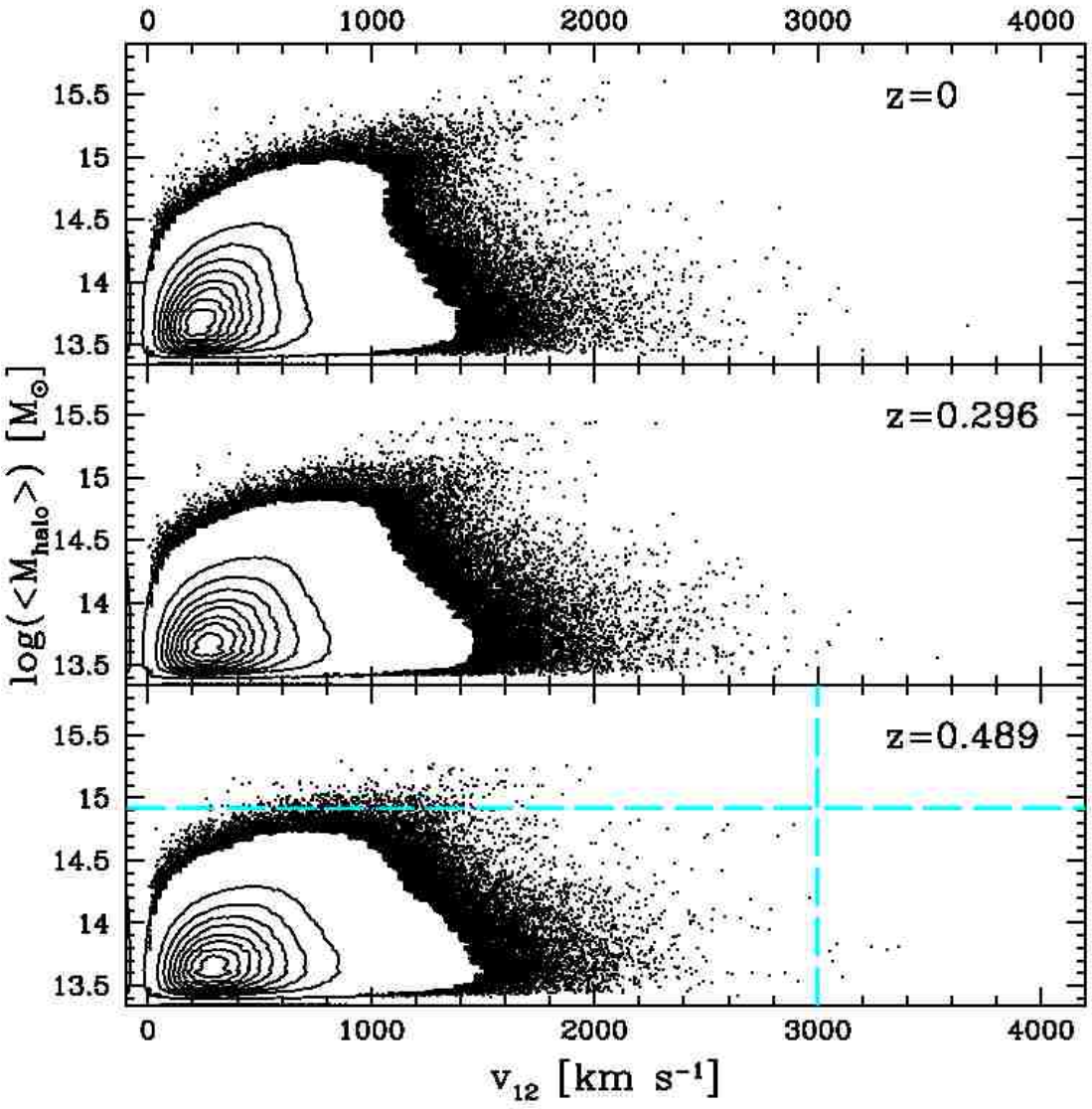

Figure 13 Average mass of halo pairs vs. their pairwise velocity for the L2016N1008 run at z=0.0, 0.296, & 0.489. In the bottom panel (z=0.489) the horizontal dashed line represents an average pair mass of $8.25 \times 10^{14} M_{\odot}$ for 1E0657-56, and the vertical dashed line represents a pairwise velocity of $3000\,\mathrm{km\,s^{-1}}$ suggested by Mastropietro & Burkert (2008).

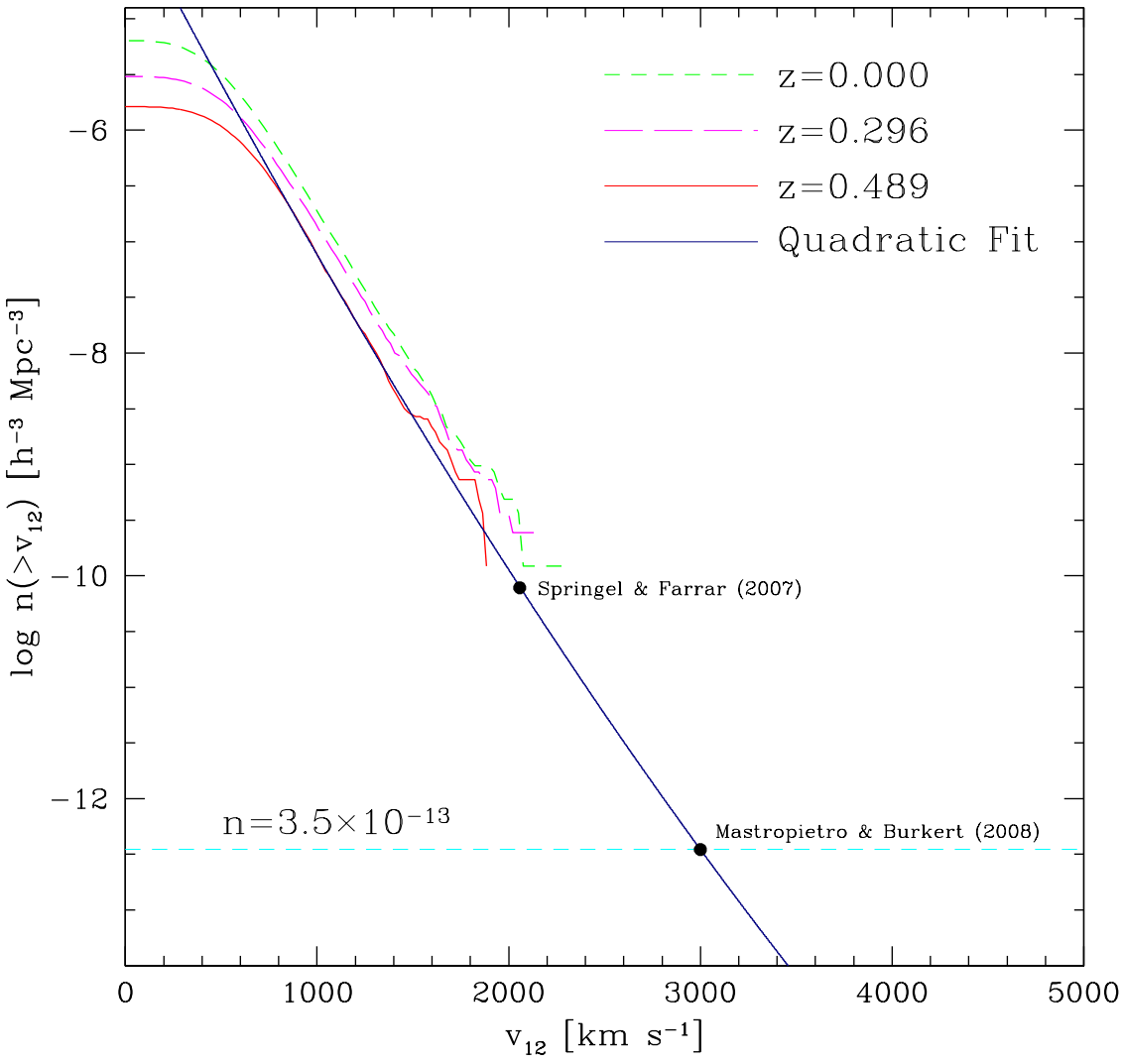

Figure 14 Comoving number density of halo pairs in the N2016N1008 run with masses above $10^{14} M_{\odot}$ at z=0, 0.296,& 0.489. We also over-plot a quadratic fit described in the text for z=0.489. The horizontal dashed line illustrates the number density of halos with $v_{12} = 3000\,\mathrm{km\,s^{-1}}$ corresponding to a box size of $(4.48\,h^{-1}\,\mathrm{Gpc})^3$ and 2240^3 DM particles. The black filled circles represent the v_{12} values listed in Table 4.

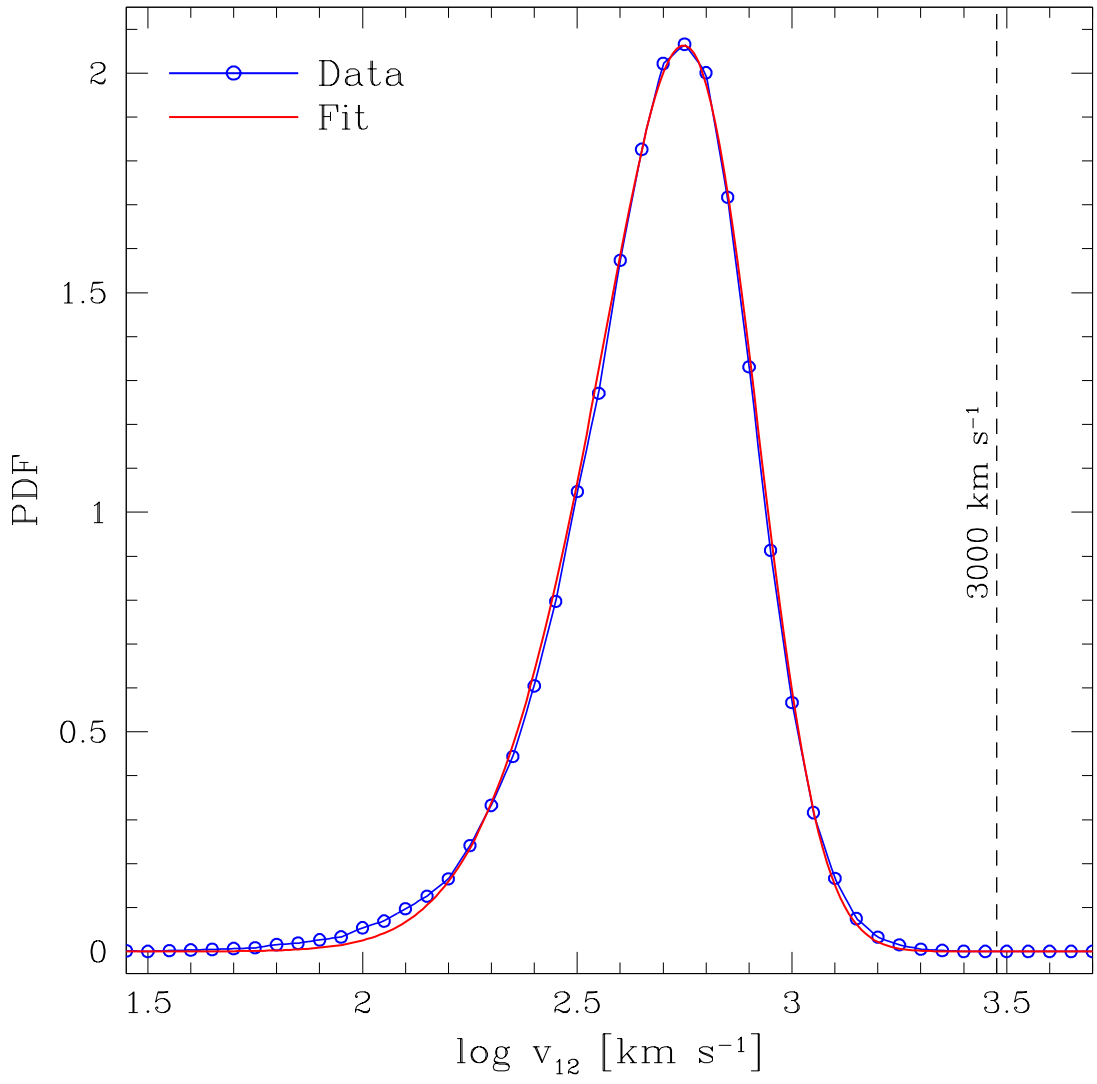

Figure 15 Pairwise velocity probability distribution function for halo pairs with masses above $10^{14} M_{\odot}$ in our L2016N1008 run. The blue circles represent v_{12} binned PDF data, the blue curve is the linearly interpolated values, and the red curve is the best-fit skew normal distribution (Azzalini & Capitanio, 2009). Integrating the fit from $v_{12} = 3000\,\mathrm{km\,s^{-1}}$ to infinity gives $P(> 3000\,\mathrm{km\,s^{-1}}) = 2.8 \times 10^{-8}$. This very low probability suggests that it is very difficult to produce a halo pair with high mass and high-v_{12} as the observed 1E0657-56.

Table 1. Summary of N-body Simulations

Run Name	Box Size $[h^{-1}$ Mpc]	Particle Count	$M_{\rm dm}$ $[h^{-1}\ M_\odot]$	ϵ $[h^{-1}$ kpc]	FOF LL $[h^{-1}$ kpc]
Box Size Effects					
L250 N125	250	125^3	5.74×10^{11}	80	400
L500 N250	500	250^3	5.74×10^{11}	80	400
L1000 N500	1000	500^3	5.74×10^{11}	80	400
L2016 N1008	2016	1008^3	5.74×10^{11}	80	400
Resolution Effects					
L250 N125	250	125^3	5.74×10^{11}	80	400
L250 N165	250	165^3	2.50×10^{11}	60.6	303
L250 N250	250	250^3	7.18×10^{10}	40	200
L250 N500	250	500^3	8.97×10^{9}	20	100

Note. — Summary of simulations employed in this paper. $M_{\rm dm}$ is the mass of each DM particle, ϵ is the comoving gravitational softening length, and FOF LL is the friends-of-friends linking length. The top four simulations explore the effects of increasing box size with fixed resolution, while the bottom four explore the effects of increasing resolution with a fixed box size.

Table 2. Highest Mass Pairs

Pair	v_{12}	θ	M_1	M_2	Mass Ratio	d	$r_{1\ virial}$	$r_{2\ virial}$
z=0								
1	1670	165	5.71E+15	5.02E+14	0.088	8.70	5.67	2.52
2	1792	46	5.71E+15	1.99E+14	0.035	7.84	5.67	1.85
3	1767	75	5.71E+15	1.01E+14	0.018	7.63	5.67	1.48
4	1624	80	5.71E+15	7.33E+13	0.013	7.13	5.67	1.33
5	2316	72	5.71E+15	7.04E+13	0.012	6.20	5.67	1.31
z=0.296								
6	1360	141	3.80E+15	3.50E+14	0.092	9.55	4.18	1.89
7	1533	44	3.80E+15	2.61E+14	0.069	6.23	4.18	1.71
8	1486	56	3.80E+15	2.51E+14	0.066	10.00	4.18	1.69
9	1425	129	3.80E+15	2.13E+14	0.056	6.20	4.18	1.60
10	2007	112	3.80E+15	1.78E+14	0.047	5.65	4.18	1.51
z=0.489								
11	869	91	3.28E+15	5.59E+14	0.170	8.78	3.70	2.05
12	1277	111	2.64E+15	1.07E+15	0.405	8.11	3.44	2.55
13	1875	132	2.45E+15	1.19E+15	0.485	3.86	3.36	2.64
14	1257	108	2.45E+15	1.08E+15	0.440	4.83	3.36	2.55
15	1256	54	3.28E+15	1.73E+14	0.053	6.01	3.70	1.39

Note. — Five halo pairs with the highest average halo mass from the L2016N1008 simulation at z=0.0, z=0.296 and z=0.489. The values of v_{12} are given in $\mathrm{km\,s^{-1}}$, collision angles θ in degrees, masses (M_1, M_2) in $M_\odot$, pair separation distances (d_{12}) and virial radius of each halo in physical Mpc. Although this simulation can produce massive pairs matching the observed mass of 1E0657-56, these pairs have too low relative velocities, and too large separation distances.

Table 3. Highest Velocity Pairs

Pair	v_{12}	θ	M_1	M_2	Mass Ratio	d	$r_{1\ virial}$	$r_{2\ virial}$
z=0								
31	3674	103	3.64E+13	2.71E+13	0.746	8.83	1.05	0.95
32	3199	151	2.14E+13	2.02E+13	0.946	8.20	0.88	0.86
33	3133	134	5.83E+13	2.60E+13	0.446	9.09	1.23	0.94
34	3095	113	8.20E+13	4.56E+13	0.556	9.21	1.38	1.13
35	3053	108	8.20E+13	2.14E+13	0.261	9.11	1.38	0.88
z=0.296								
36	3538	143	3.35E+13	1.96E+13	0.586	9.94	0.86	0.72
37	3282	125	4.96E+13	2.37E+13	0.477	9.39	0.98	0.77
38	3141	155	8.60E+13	3.41E+13	0.396	8.80	1.18	0.87
39	3089	170	6.93E+13	2.77E+13	0.400	5.27	1.10	0.81
40	3053	153	4.16E+13	2.48E+13	0.597	8.60	0.93	0.78
z=0.489								
41	3361	128	6.75E+13	2.60E+13	0.385	8.81	1.01	0.74
42	3312	148	5.66E+13	3.18E+13	0.561	8.03	0.96	0.79
43	3239	102	6.75E+13	2.37E+13	0.350	7.57	1.01	0.72
44	3109	146	2.94E+13	2.37E+13	0.804	9.57	0.77	0.72
45	3083	103	7.56E+13	2.37E+13	0.313	9.25	1.05	0.72

Note. — Five halo pairs with highest v_{12} found in the L2016N1008 simulation at z=0.0, z=0.296 and z=0.489. The values of v_{12} are given in km s^{-1}, collision angles θ in degrees, masses (M_1, M_2) in $M_\odot$, pair separation distances (d_{12}) and viral radius of each halo in physical Mpc. None of these high velocity halo pairs are massive enough to match the observations of 1E0657-56.

Table 4. Simulation Requirements to produce a Bullet

Reference	v_{12} [km s^{-1}]	Box Size [h^{-1} Mpc]	Particle Count
Mastropietro & Burkert (2008)	3000	4480	2240^3
Springel & Farrar (2007)	2057	2224	1112^3

Note. — Required box size and particle number needed to produce at least one halo pair with an average mass greater than $10^{14} M_\odot$ and a certain value of v_{12} at z=0.489 suggested by each of the authors. See text in § 2.4.3.2 for more details.

CHAPTER 3

MOLECULAR HYDROGEN REGULATED STAR FORMATION IN COSMOLOGICAL SPH SIMULATIONS

Abstract

It has been shown observationally that star formation (SF) correlates tightly with the presence of molecular hydrogen (H_2). Therefore it would be important to investigate its implication on galaxy formation in a cosmological context. In the present work, we track the H_2 mass fraction within our cosmological smoothed particle hydrodynamics (SPH) code GADGET-3 using an equilibrium analytic model by Krumholz et al. This model allows us to regulate the star formation in our simulation by the local abundance of H_2 rather than the total cold gas density, and naturally introduce the dependence of star formation on metallicity. We investigate implications of the equilibrium H_2-based SF model on galaxy population properties, such as the stellar-to-halo mass ratio (SHMR), baryon fraction, cosmic star formation rate density (SFRD), galaxy specific SFR, galaxy stellar mass functions (GSMF), and Kennicutt-Schmidt (KS) relationship. The advantage of our work over the previous ones is having a large sample of simulated galaxies in a cosmological volume from high-redshift to $z = 0$. We find that low-mass halos with $M_{\rm DM} < 10^{10.5}{\rm M}_\odot$ are less efficient in producing stars in the H_2-based SF model at $z \geq 6$, which brings the simulations to a better agreement with observational estimates of SHMR and GSMF at the low-mass end. This is particularly evident by a reduction in the number of low-mass galaxies at ${\rm M}_\star \leq 10^8{\rm M}_\odot$ in the GSMF. The overall SFRD is also reduced at high-z in the H_2 run, which results in slightly higher SFRD at low-redshift due to more abundant gas available for star formation at later times. This new H_2 model is able to reproduce

the empirical KS relationship at $z = 0$ naturally without the need for setting its normalization by hand, and overall it seems to have more advantages than the previous pressure-based SF model.

3.1 Introduction

Properly modeling star formation and feedback within simulations of galaxy formation is one of the holy grails for computational astrophysicists. Unfortunately, current cosmological simulations lack the spatial and mass resolutions to properly resolve the small scale processes which govern star formation within the interstellar medium (ISM). This computational restriction gives rise to the need for sub-grid models that can accurately describe global properties of the ISM. Simulation results can vary drastically depending on the details adopted for such sub-grid models and their feedback prescriptions. It is for this reason that these sub-grid models rely heavily on observed empirical star formation models.

The most well-known empirical star formation relation is the Schmidt (1959) and Kennicutt (1998) relationship, which relates the density (or surface density) of star formation to the gas density (or surface density), respectively. For numerical simulations of galaxy formation, the Schmidt relationship is easier to implement (e.g., Katz, 1992; Cen & Ostriker, 1992), however, observationally Kennicutt relationship is easier to measure because observations are done in the projected 2-dimensional plane. In the present work, we are implementing the Schmidt relationship as part of our SF model, but when comparing to the observations we use the Kennicutt relationship, hence referring to them collectively Kennicutt-Schmidt (KS) relationship.

Recent observational evidence has suggested that star formation is more tightly correlated with the presence of molecular hydrogen (H_2), rather than neutral atomic (HI) hydrogen (Wong & Blitz, 2002; Kennicutt et al., 2007; Leroy et al., 2008; Bigiel et al., 2008; Bolatto et al., 2011). In particular, Bigiel et al. (2008) studied the KS

relation for a sample of nearby galaxies, and found little to no correlation between $\Sigma_{\rm HI}$ and $\Sigma_{\rm SFR}$, whereas $\Sigma_{\rm H2}$ was found to correlate strongly with $\Sigma_{\rm SFR}$. Bolatto et al. (2011) used *Spitzer* dust continuum observations of the low metallicity SMC to calculate H_2 surface densities without the need for a CO luminosity conversion factor. Their findings suggested that H_2 can be used to infer star formation activity even in low metallicity galaxies.

Driven by these observational findings, new models have been developed relating SFRs directly to the abundance of H_2. Some are in the form of analytic models (Fu et al., 2010; Krumholz et al., 2008, 2009; McKee & Krumholz, 2010; Krumholz et al., 2012), while others in the form of non-equilibrium, fully time-dependent calculations (Gnedin et al., 2009; Feldmann et al., 2011; Mac Low & Glover, 2012). However, many of these models have been restricted to single isolated galaxies or cosmological zoom-in simulations of a very small sample of galaxies due to the expensive computational cost of full cosmological simulations.

Recently, both semi-analytic and non-equilibrium H_2 calculations have been implemented into full cosmological simulations. Kuhlen et al. (2012) implemented the analytic model of Krumholz et al. (2008, 2009) and McKee & Krumholz (2010) in the adaptive-mesh-refinement code Enzo (Bryan & Norman, 1997; O'Shea et al., 2004) to study how H_2-based star formation affected dwarf galaxies at $z > 4$. Both their previous model and the new H_2 model were able to reproduce many of the observational results pertaining to the KS relation. The advantage they found within the H_2 model was that it reduced the number of free parameters, and that star formation was quenched in dwarf galaxies from the onset without the need to artificially enhance stellar feedback. Christensen et al. (2012) implemented the non-equilibrium, fully time-dependent model of Gnedin et al. (2009) into their cosmological SPH code GASOLINE (Wadsley et al., 2004) in order to study the effects of H_2-based SF model on a dwarf galaxy down to $z = 0$. They found that the inclusion of H_2 resulted in

a greater baryonic mass in the disk, making it brighter, bluer, and more gas rich at $z = 0$ than the same galaxy formed without the inclusion of H_2. They also found that with H_2 there was more star formation at late times.

While there are other models of star formation based on, for example, supersonic turbulence in the ISM (e.g. McKee & Ostriker, 2007; Kritsuk & Norman, 2011; Renaud et al., 2012), it is still worthwhile to explore an implementation of H_2-based SF as well, and investigate its implications. The purpose of this paper is not to decide which process triggers the star formation (i.e., supersonic turbulence or molecules), as our simulations have neither the resolution nor detailed dust physics to address the issue. In this paper, we limit ourselves to examining the effects of a new H_2-based SF model on galaxy formation, and we defer the implementation of the turbulence-based SF model to the future.

There is another good reason to study the H_2-based SF model in cosmological simulations. Many of the earlier works based on a CDM model have predicted very steep faint-end of the mass/luminosity functions at high-redshift (e.g., Nagamine et al., 2004c; Night et al., 2006; Lo Faro et al., 2009; Finlator et al., 2011; Jaacks et al., 2012a), and suggested that these low-mass galaxies are responsible for reionizing the Universe at $z \geq 6$. However the observational estimates yield slightly shallower faint-end slopes, and if the observational results are not affected by the magnitude limit very much, the simulations need to consider processes that would decrease the number of low-mass galaxies, especially at high redshift. One of such candidate process is the H_2-based star formation, and Jaacks et al. (2012a) for example have speculated that the H_2-based SF model may reduce the discrepancy in GSMF at the low-mass end.

This paper is organized as follows. In Section 3.2 we discuss simulation parameters, SF models, and basic results. Section 3.3 contains our findings for galaxy populations. The results of SHMR, cosmic SFRD, GSMF, and KS relation are presented along with resolution studies. Lastly in Section 3.4 we summarize our results and discuss future

prospects.

3.2 Simulations & basic results

For our simulations we use a modified version of the GADGET-3 cosmological SPH code (originally described in Springel, 2005). Our conventional code includes radiative cooling by H, He, and metals (Choi & Nagamine, 2009), heating by a uniform UV background (UVB) of a modified Haardt & Madau (1996) spectrum (Katz et al., 1996; Davé et al., 1999; Faucher-Giguère et al., 2009), supernova (SN) feedback, the Multi-component Variable Velocity (MVV) wind model (Choi & Nagamine, 2011), and a sub-resolution model of multiphase ISM (Springel & Hernquist, 2003). In this multiphase ISM model, the high-density ISM is pictured to be a two-phase fluid consisting of cold clouds in pressure equilibrium with a hot ambient phase. Thermodynamic forces are calculated only for the hot phase. The cold phase on the other hand provides material for star formation, is subject to gravity, adds inertia, and participates in mass & energy exchange with the hot phase at the sub-particle level. The primary purpose of this work is to improve upon the SF models implemented within this code. Previous SF model implementations are also discussed in upcoming sections.

The same set of initial conditions (ICs) used by Choi & Nagamine (2011) and Jaacks et al. (2012a) are employed in this study to allow for cross comparison. Three primary simulations were run consisting of 2×400^3 or 2×600^3 particles of gas and dark matter. Comoving box sizes of $10h^{-1}$Mpc, $34h^{-1}$Mpc, & $100h^{-1}$Mpc are used to capture a range of halo masses. These runs will be referred to by their particle count followed by the length of their box: N400L10, N400L34, & N600L100. The other three runs (N144L10, N500L34, N600L10) where used mainly for resolution test of the H_2 model, and N500L34 & N600L10 runs were performed only for the H_2 run due to expensive computational cost. The ICs were generated using cosmological

parameters consistent with the WMAP best-fit values (Komatsu et al., 2011): $\Omega_{\rm m} = 0.26$, $\Omega_\Lambda = 0.74$, $\Omega_{\rm b} = 0.044$, $H_0/100 = 0.72$, $n_s = 0.96$, and $\sigma_8 = 0.80$. The simulation parameter values are summarized in Table 5. The runs with smaller box sizes are stopped at earlier time, because they do not include longer wavelength perturbations.

There are three additional differences between what we will refer to as the 'Fiducial' runs (Choi & Nagamine, 2011; Jaacks et al., 2012a) and the 'H_2' runs. First, we use an updated model of UVB radiation in the H_2 runs, as will be discussed in Section 3.2.2.4. The Fiducial run uses an older model wherein the UVB turns on at $z = 6.08$ to mimic the sudden reionization of the Universe; the UVB of the updated model turns on at $z = 10.75$, given the more recent WMAP results on early reionization of the Universe. For the majority of our comparisons, this change has little impact. Secondly, our H_2 runs use an optically-thick ultra-violet threshold or 'OTUV' (Nagamine et al., 2010) which will be discussed in Section 3.2.3. Most comparisons presented in this paper are not effected by this; the column density distribution presented in Section 3.3.5 and Figure 32 however, is strongly effected by this change. Our low resolution (N144L10) Fiducial run uses the OTUV threshold. Lastly, the Fiducial run uses the Salpeter (1955) initial mass function (IMF), while our new runs use the Chabrier (2003) IMF. The choice of the IMF is reflected in the value of gas recycling fraction parameter β in the SF relation in our simulation. We have also verified that this has little impact on the results presented in this paper.

3.2.1 Previous SF models

3.2.1.1 SH model

Springel & Hernquist (2003, SH model) describes the hybrid multiphase model for SF, originally implemented in the GADGET code. In this model, the SFR is

determined by

$$\dot{\rho}_* = (1-\beta)\frac{\rho_{cold}}{t_*}, \tag{3.1}$$

where ρ_{cold} is the density of cold gas available to form stars, and β is the fraction of stars instantaneously destroyed as supernova, determined by the stellar IMF. The parameter t_* is the SF time-scale which is taken to be proportional to the local dynamical time of the gas:

$$t_* = t_0^* \left(\frac{\rho}{\rho_{th}}\right)^{-1/2}, \tag{3.2}$$

where ρ_{th} is a density threshold, above which the gas is assumed to develop a multi-phase structure and form stars. The parameter t_0^* controls the normalization of the Kennicutt (1998) relation:

$$\Sigma_{\rm SFR} = \begin{cases} 0 & \text{if} \quad \Sigma_{\rm gas} < \Sigma_{th} \\ A\,(\Sigma_{\rm gas}/1{\rm M}_\odot{\rm pc}^{-2})^n & \text{if} \quad \Sigma_{\rm gas} > \Sigma_{th}, \end{cases} \tag{3.3}$$

where Σ_{th} is the SF threshold surface density. Observations suggest $A = 2.5 \pm 0.7 \times 10^{-4}{\rm M}_\odot{\rm yr}^{-1}{\rm kpc}^{-2}$, $n = 1.4 \pm 0.15$, and $\Sigma_{th} \sim 10{\rm M}_\odot{\rm pc}^{-2}$ (Kennicutt, 1998). The cutoff in $\Sigma_{\rm SFR}$ is controlled by ρ_{th}, which indirectly regulates Σ_{th}. See Springel & Hernquist (2003) for a description of how ρ_{th} is calculated self-consistently for this model.

Our simulations deal with three dimensional densities (i.e. Equation 3.1) rather than the two dimensional surface densities described by the KS-relation. It is not obvious then that Eq. (3.1) would be able to reproduce the observed KS-relation given by Eq. (3.3). Previous simulations (Springel & Hernquist, 2003; Nagamine et al., 2004b) were able to demonstrate that the observed relation could indeed be reproduced using $t_0^* = 2.1\,{\rm Gyr}$, which resulted in a threshold value of $\rho_{th} = 0.35\,h^2{\rm cm}^{-3}$. However Nagamine et al. (2004b) and Choi & Nagamine (2010) showed that using this value of ρ_{th} results in overprediction of $\Sigma_{\rm SFR}$ at low column densities ($N_{\rm HI} \leq 10^{20.5}{\rm cm}^{-2}$). This

over-prediction, coupled with the fact that this model produces stars from cold atomic gas rather than molecular, leads to the necessity for improvement in the sub-grid SF model, which we describe in the following sections.

3.2.1.2 Pressure model

Previous SF models assumed that the exponents of the Kennicutt and Schmidt relationships are equal. This is only true if the galactic disk scale-height is constant, or the equation of state behaves as $P \propto \rho^2$ (Schaye & Dalla Vecchia, 2008). Arguing that these assumptions are unnecessary and often incorrect, Schaye & Dalla Vecchia (2008) formulated a fully analytic conversion from the 2D KS-relation ($\Sigma_{\rm gas}$) to a 3D Schmidt-relation ($\rho_{\rm gas}$). They proposed that the density of a self-gravitating disk will fluctuate on the local Jeans scale, leading to the scale-height also being on the order of the local Jeans scale. This in turn leads to the gas column density being on the order of the 'Jeans column density':

$$\Sigma_{\rm gas} \sim \Sigma_{\rm gas,J} \equiv \rho_{\rm gas} L_{\rm J} = \left(\frac{\gamma}{G}\right)^{1/2} \left(f_g P_{tot}\right)^{1/2}, \tag{3.4}$$

where $L_{\rm J} = c_s/\sqrt{G\rho_{tot}}$ is the Jeans length, $c_s = \sqrt{\gamma P_{tot}/\rho_{\rm gas}}$ is the local sound speed, γ is the ratio of specific heats, G is the gravitational constant, f_g is the mass fraction within the scale-height of the gas, and P_{tot} is the mid-plane pressure. The SFR in this model is also described by Equation (3.1); the difference comes in the formulation of t_0^* which is derived by combining Equations (3.3) & (3.4):

$$t_0^* = \frac{\Sigma_{\rm gas}}{\Sigma_{\rm SFR}} = A^{-1} \left(1\,{\rm M_\odot\,pc^{-2}}\right)^n \left(\frac{\gamma}{G}\, f_{\rm g}\, P_{tot}\right)^{(1-n)/2}. \tag{3.5}$$

Schaye & Dalla Vecchia (2008) claim that their analytical conversion renders their parameters 'untweakable'. Adopting $n = 1.4$ & $\gamma = 5/3$, Choi & Nagamine (2010) implemented this model within our GADGET-3 code with some minor modifications.

It was found to reduce the overprediction of $\Sigma_{\rm SFR}$ at low column densities and was in good agreement with the observed KS-relation. It also reduced the SFR in low-density regions, causing a suppression of early star formation, which in turn shifted the peak of the cosmic SFRD to lower redshifts in better agreement with observational estimates.

The disadvantage of this model is that we are still imposing the KS relation onto our SF prescription. In an ideal situation the model would naturally reproduce the observed KS relation without such impositions. Simulations and data from previous work based off of the Schaye & Dalla Vecchia (2008) Pressure SF model (Choi & Nagamine, 2010, 2011; Jaacks et al., 2012a) will serve as our Fiducial runs for comparison.

3.2.2 H_2 *regulated star formation*

If star formation really requires molecular gas, then tracking the H_2 gas fraction and basing our SF prescription on it would make for a more realistic sub-grid model. There are currently two primary ways in which the H_2 mass fraction can be tracked in simulations. The first is a non-equilibrium model which calculates the H_2 fraction via a fully time-dependent chemistry and radiative transfer calculation as was done by Gnedin et al. (2009) and Christensen et al. (2012). This approach accurately calculates the instantaneous H_2 gas fraction, but can be computationally expensive. The second is a analytical approach developed by Krumholz et al. (2008, 2009) and McKee & Krumholz (2010) (hereafter KMT model), which calculates an equilibrium H_2 fraction assuming a formation-dissociation balance.

These two methods were directly compared in Krumholz & Gnedin (2011); the second method was found to be a viable and nearly cost free alternative to the computationally expensive first option at metallicities $Z \geq 10^{-2} Z_{\odot}$, where $Z_{\odot}$ is the solar metallicity. At metallicities $< 10^{-2} Z_{\odot}$ the KMT model was found to over-predict

the fractional H_2 abundance due to the neglect of time-dependent effects. Krumholz (2012) however, argues that the equilibrium H_2 fraction rather than the instantaneous one correlates more with gas temperature. He argued that the thermal timescale of gas is much shorter than the chemical timescale, which means that low metallicity clouds should cool via collisional de-excitation and form stars faster than they can fully convert all of their atomic gas to molecular. This suggests that the fractional H_2 abundance calculated by the KMT model may more accurately predict the amount of material available to form stars in low metallicity gas. Due to the computational simplicity we choose to adopt the KMT model to track H_2 within our simulations, and examine its impact on cosmological galaxy formation.

3.2.2.1 KMT model

Krumholz et al. (2008, 2009) and McKee & Krumholz (2010) developed an analytic model for tracking H_2 mass fraction. They used a Strömgren-type analysis, starting with a spherical gas cloud immersed in a uniform, isotropic Lyman-Werner band radiation field. Assuming that the cloud is in a steady state, they proceeded to solve the radiative transfer and H_2 formation-dissociation balance equations. After some approximations, they found a solution

$$f_{\rm H_2} \equiv \frac{\rho_{\rm H_2}}{\rho_{\rm HI}} \approx 1 - \frac{3}{4}\left(\frac{s}{1+0.25s}\right), \tag{3.6}$$

where $f_{\rm H_2}$ is the H_2 mass fraction relative to the neutral hydrogen gas. At such high densities where molecular gas may form, the hydrogen gas would be mostly neutral within our multiphase ISM model, hence the neutral hydrogen (HI) in the denominator above (see also Section 3.2.2.2). The parameter s is essentially the size

of the atomic-molecular complex given by

$$s \equiv \frac{\tau_R}{\tau_c}\xi_d = \frac{\ln\left(1 + 0.6\chi + 0.01\chi^2\right)}{0.6\tau_c}, \tag{3.7}$$

where τ_R is the dust optical-depth of the atomic-molecular complex, τ_c is the mean optical depth, and ξ_d is the characteristic radius (in units of the cloud radius) at which the transition from dust-dominated to molecular-dominated absorption occurs. The variable χ can be thought of as an estimation of the local radiation field given by

$$\chi = 71\left(\frac{\sigma_{d,-21}}{\mathcal{R}_{-16.5}}\right)\frac{G'_0}{n_{\rm H}}. \tag{3.8}$$

Here $\sigma_{d,-21}$ is the dust cross section per H nucleus to 1000Å radiation normalized to a value of $10^{-21}{\rm cm}^2$, $\mathcal{R}_{-16.5}$ is the rate coefficient for H_2 formation on dust grains normalized to the Milky Way value of $10^{-16.5}{\rm cm}^{-3}{\rm s}^{-1}$ (Wolfire et al., 2008), G'_0 is the ambient UV radiation field intensity normalized to the Draine (1978) value for the Milky Way, and $n_{\rm H}$ is the volume density of H nuclei.

At this point $f_{\rm H_2}$ depends only on τ_c & χ. In order to calculate the dust optical depth (τ_c) we first calculate the local HI column density ($\Sigma_{\rm HI}$) by means of a Sobolev-like approximation (e.g. Gnedin et al., 2009; Krumholz & Gnedin, 2011):

$$\Sigma_{\rm HI} \approx \rho_{\rm HI} \times h, \tag{3.9}$$

where h is the local scale height calculated by

$$h \approx \frac{\rho_{\rm HI}}{|\nabla\rho_{\rm HI}|}. \tag{3.10}$$

We find that per-particle, the Sobolev approximation gives higher values of $\Sigma_{\rm HI}$ than a true column density calculation. However, when we take the mass-weighted average

of these values along a column, the Sobolev approximation was actually lower by a factor of ~ 5 in the high density regions of interest. This suggests that, within each column, there are more particles with a low Sobolev-surface density. The average therefore, is biased towards lower values. As an experiment we ran a test simulation boosting $\Sigma_{\rm HI}$ in the high density regions by a factor of 5, and we find that more stars are formed at late times due to higher Σ values. Given that our current Sobolev approximation gives lower Σ values, we could regard our results on star formation as lower limits (See Section 3.3.2).

We can then find the dust optical depth by the relation $\tau_c = \Sigma_{\rm gas}\sigma_d/\mu_{\rm H}$, where σ_d is the dust cross section per hydrogen nucleus and $\mu_{\rm H}$ is the mean mass per H nucleus. The dust cross section is taken to be $\sigma_{d,-21} = 10^{-21} Z_{\rm sn} {\rm cm}^2$, where $Z_{\rm sn}$ is the gas metallicity normalized to the solar neighborhood value $Z_\odot = 0.0204$ (Rodríguez & Delgado-Inglada, 2011). The KMT model shows that, if the ISM is in a self-consistently determined two-phase equilibrium, then the ratio $G_0'/n_{\rm H}$ takes a characteristic value, and Equations (3.7) & (3.8) become

$$s \approx \frac{\ln\left(1 + 0.6\chi + 0.01\chi^2\right)}{0.04\left(\frac{Z}{Z_\odot}\right)\left(\frac{\Sigma_{\rm HI}}{{\rm M}_\odot {\rm pc}^{-2}}\right)} \tag{3.11}$$

and

$$\chi \approx 3.1\frac{1 + 3.1\left(Z/Z_\odot\right)^{0.365}}{4.1}, \tag{3.12}$$

respectively. Using Equations (3.11) & (3.12) we can now calculate the H_2 fraction of each gas particle by means of Equation (3.6) if $0 < s < 2$ (McKee & Krumholz, 2010), otherwise $f_{\rm H_2} = 0$.

Figure 16 shows how the transition from fully atomic to atomic & molecular changes for different metallicities. The value $s = 2$ is the minimum complex size required to allow for the transition from atomic to molecular gas for any given metallicity. This represents the need for the gas cloud to be sufficiently large to allow for the

formation of H_2. External UV radiation is absorbed first by dust, which is essentially traced by the metallicity, then by a thin molecular region. If the cloud is too small then there will not be enough surrounding material to absorb all of the UV, and the H_2-core will be dissociated. If the cloud is large, we expect a large molecular core. Higher metal content effectively absorbs more radiation, allowing for the formation of H_2 at lower surface densities.

Knowing f_{H_2} allows us to modify our SF model by replacing ρ_{cold} in Equation (3.1) with the H_2 mass density $\rho_{H_2} = f_{H_2}\,\rho_{HI}$. We also change our SF time-scale to a more physically realistic value, namely the free-fall-time of the H_2 gas available to form stars

$$t_{ff} = \sqrt{\frac{3\pi}{32 G \rho_{H_2}}}. \tag{3.13}$$

Furthermore, observations have shown that SF is a slow process and that the efficiency at which dense regions produce stars is $\sim$1% (Krumholz & Tan, 2007; Lada et al., 2010). To account for this we introduce an efficiency parameter of $\epsilon_{SF} = 0.01$ which leads us to our new formulation of Equation (3.1):

$$\dot{\rho}_* = (1-\beta)\,\epsilon_{SF}\,\frac{\rho_{H_2}}{t_{ff}}. \tag{3.14}$$

If a gas particle has $f_{H_2} > 0$, then it is eligible to form stars at the above rate.

3.2.2.2 Assumption on the neutral fraction

As discussed in the previous section, in order to calculate the fractional H_2 abundance, we must first calculate the scale-height of HI, which then allows for the calculation of Σ_{HI}. Our GADGET-3 code tracks the neutral fraction of each gas particle individually. For the high density multiphase gas however, the neutral fraction is tracked only for the hot phase, and the cold gas fraction $x \equiv \rho_c/\rho$ is computed within the multiphase ISM sub-particle model (Springel & Hernquist, 2003). For the very

high-density particles, most of the mass is in cold, neutral phase ($x \gtrsim 0.95$), but the tenuous hot phase determines the thermodynamic temperature. We calculate the neutral fraction using the x-parameter for high-density particles above the SF threshold for our N144L10 fiducial run at $z = 3$, and find all of particles to have $f_{\rm HI} > 0.96$, and 98% of the hydrogen mass to have $f_{\rm HI} > 0.97$. Given the small mass fraction of ionized gas, it is a good approximation to assume that any gas particle with $n_{\rm th}^{\rm SF} > 0.6\,{\rm cm}^{-3}$ (Choi & Nagamine, 2010) is completely neutral ($f_{\rm HI} = 1$) for the scale-height and column density calculations detailed in Section 3.2.2.1.

3.2.2.3 H_2 *formation threshold density and Wind model modifications*

This new SF model (Eq. [3.14]) allows us to compute the density threshold (ρ_{th}) for individual particles based on their metallicity, above which results in the formation of H_2. In the earlier version of our GADGET-3 code, Choi & Nagamine (2011) implemented the "Multi-component Variable Velocity" wind model, in which a particle was allowed to travel as a wind particle with no hydrodynamic forces applied as long as its physical density exceeded $0.1 \times {\rm n}_{\rm th}^{\rm SF}$ (i.e., maximum wind travel length threshold). The wind velocity of each particle was calculated based on the SFR of galaxy that the particle belongs to. We can now revise this wind criteria to be based off of individual particle's H_2 formation threshold rather than a fixed value as in previous SF models.

The formation of H_2 requires sufficient shielding, or else the molecule will be dissociated by UV radiation. We can set the threshold for H_2 formation for each particle by solving Equation (3.11) for $\Sigma_{\rm gas}$ using $s = 2$; this value allows us to calculate the minimum Σ for SF within our model:

$$\frac{\Sigma_{th}}{{\rm M}_\odot {\rm pc}^{-2}} \approx \frac{\ln\left(1 + 0.6\chi + 0.01\chi^2\right)}{2 \times 0.04\,(Z/Z_\odot)}. \tag{3.15}$$

We can then convert this surface density threshold to a volume density threshold

using Equation (3.9) for each particle, which leads us to the minimum volume density required to form H_2 at that particle's particular metallicity:

$$\rho_{\mathrm{HI_{th}}} \approx \frac{\ln\left(1 + 0.6\chi + 0.01\chi^2\right) \mathrm{M_\odot pc^{-2}}}{2 \times 0.04\,(Z/Z_\odot)\,h}. \tag{3.16}$$

In other words, this is the H_2 formation density threshold. In the present work, if the physical density of a gas particle is above its particular adaptive H_2 formation threshold $\rho_{\mathrm{HI_{th}}}$, then it is eligible to be a member of the wind.

Figure 17 shows the values of $\rho_{\mathrm{HI_{th}}}$ vs. metallicity of each particle in a low resolution simulation (N144L10). The previous SF density threshold is shown as the black dashed vertical line. Generally, the values of $\rho_{\mathrm{HI_{th}}}$ are higher for each particle than in the previous SF models, allowing for particles to reach higher densities before becoming eligible to form stars. This makes SF in the H_2 model less efficient than in the previous SF models. This plot also shows that for a given metallicity, a lower h returns higher $\rho_{\mathrm{HI_{th}}}$. Particles with higher metal content have lower formation thresholds due to their ability to absorb more dissociating photons. The accumulation of particles at $Z = 10^{-3} Z_\odot$ corresponds to those that have yet to be enriched by SF, but they have varying $\rho_{\mathrm{HI_{th}}}$ due to variations in h. Some particles at $-2 < \log n_{\mathrm{th}} < 0$ have already been enriched by $z = 3$.

3.2.2.4 Metal Floor

In our Fiducial runs, initially all gas particles are metal free. Enrichment occurs during star formation; in this process SN explosions return a metal mass of $\Delta M_Z = y_* \Delta M_*$ to the ISM, where $y_* = 0.02$ is the yield, and M_* is the mass of newly formed long-lived stars. It is assumed that each gas particle behaves as a closed box locally, wherein metals are instantaneously mixed between cold clouds and ambient hot gas.

Within the framework of our new SF model, stars can only form if they contain

H_2, as determined by Equation (3.6). In order for $f_{H_2} \neq 0$, the gas particle must have some metal content. To begin forming stars, we must first enrich the gas particles by hand at very high redshift. Recent high resolution numerical studies by Wise et al. (2012) found that a single pair-instability supernova of a Pop. III star can enrich its host halo to a metallicity of $10^{-3} Z_{\odot}$. Their findings are in agreement with observed DLA metallicities, which have metal floors of the same order (Wolfe et al., 2005; Penprase et al., 2010). To mimic this enrichment, we introduce a metal floor of $Z = 10^{-3} Z_{\odot}$ for all gas particles at a specified epoch.

To test the impact of the assumed metal floor, a few low resolution simulations (N144L10) are performed introducing the metal floor at redshifts of $z = 9, 11,$ &13; we refer to these as MF9, MF11, & MF13 runs, respectively. The cosmic SFRD histories are nearly identical between these three simulations; they differ only in the point at which each simulation starts to form stars. This is due to the different times at which their metal floors are introduced. The MF11 & MF13 runs both start to form stars at $z \sim 9.2$, while MF9 does not begin star formation until $z \sim 8.6$. After their initial bursts of star formation, each of the three simulations begin following the same SFRD track from $z \sim 8.3$ to $z = 3$. The GSMF between the three simulations are also nearly identical at $z = 3$ & 6, suggesting that the formation of galaxies within our simulations does not heavily depend on when the metal floor is set. Lastly, the SHMR (cf. Section 3.3.1.2) is examined at $z = 3$ & 6 for each simulation. We find significant scatter in the results for all three runs, but the median SHMR values for each simulation are all well within one standard deviation of one another. This again suggests that the stellar fraction of each halo does not depend heavily on the time at which the metal floor is set.

The redshift at which the metal floor is introduced is related to the metal enrichment by Pop. III stars. Therefore, we choose to introduce our metal floor at the epoch of reionization. Observational estimates by Komatsu et al. (2011) suggest this

happens at redshift $z = 10.6 \pm 1.2$. In our simulation, reionization is set by the UV background model (Faucher-Giguère et al., 2009, December 2011 version)[1], hence our metal floor of $Z = 10^{-3}\,Z_{\odot}$ is set at $z \sim 10.75$ accordingly.

3.2.3 Gas phase diagram

We examine a low resolution N144L10 simulation to study the gas temperature-density phase diagram. Figure 18 compares our Fiducial run with the new H_2 run at $z = 3$. Panel (a) represents our Fiducial run and contains three vertical lines representing different thresholds. The left most dashed line ($n_{\rm th}^{\rm UV} = 0.006\,{\rm cm}^{-3}$) represents an optically-thick ultra-violet threshold or 'OTUV' (Nagamine et al., 2010). Any particle below this threshold will be heated by the UVB to $> 10^4\,{\rm K}$; any particle above this threshold is shielded from the UVB. Nagamine et al. (2010) and Yajima et al. (2011) have demonstrated that this threshold is reasonable using full radiative transfer calculations.

The right most dotted line in Figure 18a represents the constant SF physical density threshold ($n_{\rm th}^{\rm SF} = 0.6\,{\rm cm}^{-3}$) in the Fiducial run. Any particle whose density exceeds this threshold is allowed to form stars based on the prescription outlined in Section 3.2.1.2. At densities & temperatures above $n \sim 3\,{\rm cm}^{-3}$ & $T \sim 10^4\,{\rm K}$, we begin to see the effects of SN feedback and the multi-phase ISM model (Springel & Hernquist, 2003). The cold phase component dominates the mass of the particle, but the hot phase governs the temperature. What is seen in this 'arm' is the temperature of the gas heated by SN feedback (hot phase component), and the density of the cold phase component. When we direct our attention to the H_2 run (Panel b) we see that this arm is now extended out to higher densities at lower temperatures. This is because stars are only allowed to form if the gas particles contain any H_2 above the adaptive density threshold $\rho_{\rm HI,th}$ given by Equation (3.16). As discussed earlier, Fig-

[1] `https://www.cfa.harvard.edu/~cgiguere/UVB.html`

ure 17 illustrates how $\rho_{\rm HI,th}$ is typically higher than the previous SF density threshold, which allows particles to condense to higher densities without being heated by SN feedback.

The dot-dashed line in between the two previously discussed lines in Figure 18a represents the maximum wind travel length (TL) threshold of $n_{\rm TL}^{\rm w} = 0.1 \times n_{\rm th}^{\rm SF} = 0.06\,{\rm cm}^{-3}$. If a particle becomes a member of the wind, hydrodynamic forces are turned off for a brief period of time (Springel & Hernquist, 2003; Choi & Nagamine, 2011). This allows the gas to adiabatically expand and cool to lower temperatures until the density drops below $n_{\rm TL}^{\rm w}$, or the brief period of time has elapsed. The dot-dashed line is absent from the Panel (b) because of the varying density threshold for each particle. Instead of a temperature discontinuity, as can be seen in Panel (a), we have a 'tail' that extends all the way to the OTUV threshold. This tail corresponds to wind particles that have adiabatically expanded as part of the galactic wind.

3.2.4 Atomic to molecular transition

It is important to study where the atomic to molecular transition occurs in our simulations. Figure 19 shows this transition as a function of gas surface density in our N600L100 run at $z = 0$ for three different metallicity ranges. In the KMT model, the value of $f_{\rm H_2}$ is solely determined by the surface density of gas and metallicity (Equations 3.6, 3.11 & 3.12), therefore the simulation data (black dots) in all three panels is restricted to a relatively thin band determined by the range of metallicity chosen.

Christensen et al. (2012) examined this transition for three isolated Milky Way-like simulations at different metallicities to test their fully time-dependent, non-equilibrium H_2 calculation. Their raw simulation output can be seen as the red contour in Figure 19. The transition in our simulations is in good agreement with theirs, corroborating the comparison work of Krumholz & Gnedin (2011). However,

our data deviates to higher column densities at high molecular fractions due to the per-particle overestimation of the column density calculated by the Sobolev-like approximation, as discussed in Section 3.2.2. This deviation should not pose a problem since particles in these high column density regions are already fully molecular.

3.3 Results on galaxy populations

3.3.1 Dark matter halo content

Dark matter (DM) particles were grouped using a simplified version of the parallel friends-of-friends group finder SUBFIND (Springel et al., 2001). The code groups the particles into DM halos if they lie within a specified linking length. We adopt a standard value of $b = 0.2$ for the linking length parameter, which is a fraction of the initial mean inter-particle separation. Each halo must also have a minimum of 100 particles to be considered a halo.

The DM halo mass functions were found to be in agreement between the H_2 and Fiducial runs. This is an expected result, because both sets of simulations were started from the identical IC. Both results are in good agreement with the Sheth & Tormen (1999) mass function. This paper focuses on baryonic properties, and it is useful to examine and compare the contents of these halos between the Fiducial and H_2 runs. The contents of each halo are calculated by the summation of particle properties located within $r_{200} = [(GM_{\rm DM})/(\Omega_{\rm m}(z)H(z)^2)]^{1/3}$ (Mo & White, 2002) of each halo's center of mass.

3.3.1.1 Baryon fraction

Figure 20 presents the baryon mass fraction over halo mass ($f_{\rm b} \equiv M_{\rm baryon}/M_{\rm DM} = (M_{\rm gas,200} + M_{\star,200})/M_{\rm DM}$) as a function of $\log M_{\rm DM}$ at $z = 6, 3, 1$ & 0. Here the cosmic mean ($\Omega_{\rm b}/\Omega_{\rm DM}$) is illustrated by the horizontal black dashed line. Panel (a) shows the composite data from the N400L10, N400L34, & N600L100 runs at $z = 6$;

Panel (b) is composite data from the N400L34 & N600L100 runs at $z = 3$; Panels (c) & (d) are composed of data from the N600L100 simulation only at $z = 1$ and 0, respectively. Solid lines represent the median value within each bin, and the hatched regions represent a 1σ spread in the data. The cutoff of the data at lower mass end is determined by the halo mass limit of the halo grouping.

At $z = 6$ (panel [a]), the $f_{\rm b}$ of the two SF models agree with each other well and with the cosmic mean for halos above $M_{\rm DM} \sim 10^9 {\rm M}_\odot$. Halos below this mass in the H_2 run have lower $f_{\rm b}$ than in the Fiducial run by $\sim 35\%$. This is presumably due to the different UVB model between the two runs; in the H_2 run the UVB is turned on much earlier, and the gas in low-mass halos are photo-evaporated.

This large difference in $f_{\rm b}$ is nonexistent in low mass halos at $z = 3$ as shown in Panel (b). The median values within the H_2 run are now generally higher than those in the Fiducial run. As we will see in later sections, this is likely due to higher SFRs and hence stronger SN feedback in the Fiducial run, and this trend continues to $z = 0$. The scatter in $f_{\rm b}$ at $M_{\rm DM} \sim 10^{9.7} {\rm M}_\odot$ is greater for the H_2 model, but it encompasses that of Fiducial run. Both begin to drop slightly below the cosmic mean at around $M_{\rm DM} \sim 10^{12} {\rm M}_\odot$.

By $z = 1$, $f_{\rm b}$ in the most massive halos settle to a value that is lower than the cosmic mean by $\sim 7\%$. Again in Panel (c), we see $f_{\rm b}$ in massive halos with $M_{\rm DM} > 10^{12} {\rm M}_\odot$ is in agreement between the two models. At lower $M_{\rm DM}$, the Fiducial run still shows a lower baryon fraction. Finally at $z = 0$, we see that, for the halos with $M_{\rm DM} < 10^{12} {\rm M}_\odot$, the mean $f_{\rm b}$ has decreased slightly since $z = 1$. This means that the halos on average have acquired more dark matter than baryons (either through mergers or accretion), and/or at the same time lose the gas from galaxies due to SN feedback. The scatter of $f_{\rm b}$ for lower mass halos is generally greater than for the massive halos, and this is a known resolution effect (e.g., O'Shea et al., 2005).

3.3.1.2 Stellar-to-halo mass ratio (SHMR)

The ratio of stellar-to-halo mass as a function of total halo mass $M_{\rm tot,200}$ (DM+gas+stars within r_{200}) provides a useful insight on the efficiency of star formation in different halos, and it has collected significant attention in the recent years (Conroy et al., 2007; Baldry et al., 2008; Behroozi et al., 2010; Moster et al., 2010; Foucaud et al., 2010; Evoli et al., 2011; Leauthaud et al., 2012; Papastergis et al., 2012). All of these work find a prominent peak in this relation at $M_{\rm tot,200} \sim 10^{12}{\rm M}_{\odot}$, suggesting that there is a characteristic halo mass that galaxy formation is most efficient. This mass-scale roughly corresponds to the characteristic stellar mass M^* of GSMF, i.e., the knee of Schechter function, where most of the stellar mass has formed globally. To further surprise, Behroozi et al. (2012, hereafter B12) found that, using observational data and semi-analytic modeling, SHMR is almost time-independent between $z = 4$ to $z = 0$. This is interesting, because SHMR should reflect all the cumulative effects of past star formation and feedback, and non-evolving SHMR suggests tight self-regulation and a subtle balance between star formation and feedback. It is a significant challenge for any cosmological hydrodynamic simulation to reproduce this relation across a wide range of halo mass and cosmic time.

Note that we are specifically using $M_{\rm tot,200}$, and not $M_{\rm DM}$ for this comparison. This is because Munshi et al. (2012) pointed out that, in order to accurately compare simulations to semi-analytic model results (such as abundance matching technique), one must observe the simulations in a similar manner. They refer to the work by Sawala et al. (2012), who showed that $M_{\rm tot,200}$ in N-body simulations can be greater than those in N-body+hydro simulations by up to 30%, because various baryonic processes (gas pressure, reionisation, supernova feedback, stripping, and truncated accretion) can remove baryons from the halo, decreasing the total mass systematically. Additionally, Graham et al. (2005) found that the stellar mass component of observed galaxies could be systematically underestimated by $\sim 20\%$ in some cases; for example,

additional flux of 0.22 mag lies beyond the SDSS Petrosian aperture for a galaxy that has an $R^{1/4}$ profile. Here, we consider that it would be more natural to examine SHMR as a function of $M_{\rm tot,200}$ rather than correcting our results by a certain number.

In Figure 21, we show the SHMR in our simulations by calculating the total stellar mass contained within r_{200} of each halo's center-of-mass ($M_{\star,200}$). If we assume that the B12 data extends out to $z = 6$, we see in Figure 21a that our H_2 run does a good job at reproducing the B12 data at $M_{\rm tot,200} < 10^{12}{\rm M}_\odot$, much better than the Fiducial model. We have verified that the different UVB models do not impact this result. The comparison of the models in Figure 21 clearly suggests that the suppression of star formation in low-mass halos is favorably achieved by the H_2 model. Note that this SF suppression is not due to the SN feedback, but rather due to the metallicity dependence of the new H_2-based SF model. This could become a critical point to distinguish between the H_2-based and turbulence-based SF models in the future.

At $z = 3$ (Figure 21b) the SHMR increases slightly for both simulations. Our simulations are in agreement with the B12 data at $M_{\rm tot,200} < 10^{12.2}{\rm M}_\odot$. However, we continue to overestimate SHMR at $M_{\rm tot,200} > 10^{12.2}{\rm M}_\odot$ down to $z = 0$, which could be due to lack of AGN feedback in our current simulations. It is widely believed that both thermal and momentum feedback from supermassive black holes suppresses the star formation in massive halos, making them 'red & dead' (e.g., Di Matteo et al., 2005; Springel et al., 2005a; Nagamine et al., 2005; Ostriker et al., 2010; Choi et al., 2012). There is little evolution between $z = 1$ & 0 in our simulations (Figure 21c,d), and our results are higher than B12 data even for low-mass halos at $z \leq 1$.

3.3.2 Quantities related to star formation

3.3.2.1 Cosmic star formation history

With the H_2 model producing less stars in lower mass halos, we expect the cosmic SFRD to be lower as well. When comparing simulations to observational estimates

of SFRD, we have to be careful about which IMF is being used. The Fiducial and H_2 runs use different IMFs. In order to fairly compare the two, we must make corrections to either the simulation data or the observations. Because SFR is a raw output of our simulation, we prefer to take the latter route and correct the observational data to the same IMF as in simulation. A simple factor $f_{\rm IMF}$ allows for this conversion:

$$\dot{\rho}_\star^{\rm IMF} = \dot{\rho}_\star^{\rm Salpeter} / f_{\rm IMF}, \tag{3.17}$$

where $\dot{\rho}_\star^{\rm IMF}$ represent an arbitrary IMF. To convert from Salpeter to Chabrier, we take $f_{\rm IMF} = 1.6$ (e.g., Nagamine et al., 2006; Raue & Meyer, 2012), and from Salpeter to Kroupa we take $f_{\rm IMF} = 1.8$ (Horiuchi et al., 2009). This is because, for a given amount of observed rest-frame UV flux, the required SFR would be lower for an IMF that is weighted more towards higher masses. After correcting our IMFs, we find that both simulations roughly agree with the observed data.

Figure 22 shows the cosmic SFRD history as a function of redshift. As expected, the H_2 runs show significantly lower SFRD at most redshifts relative to the corresponding Fiducial runs. The H_2 runs do not start forming stars until $z \sim 10.5$, which is a consequence of our model. In the H_2 run, in order for gas to be eligible for SF, it must first contain H_2, which requires non-zero metal content. As discussed in Section 3.2.2.4, we introduce the metal floor by hand at $z \sim 10.75$, after which stars are able to form. Until the metal floor is introduced, the gas continues to condense to higher densities.

The slopes of the H_2 SFRDs at high-z are slightly steeper than the Fiducial runs, because the H_2 run starts SF a little later than the Fiducial run, and has more abundant high-density gas available for SF. It tries to catch up to the Fiducial run after the metal floor is introduced. For the same reason, the peak of the SFRD of the N600L100 H_2 run is slightly shifted towards lower redshift compared to the Fiducial

run. With a lower SFRD in the H_2 runs, there are more gas available for SF at later times.

Note that Figure 22 is only showing the results of different simulations as separate lines, and it does not show the expected total SFRD. To really obtain the total SFRD, we must carefully examine the contribution from each galaxy mass ranges to SFRD, and sum up the contribution from each simulation. This was done by Choi & Nagamine (2010) for the Fiducial runs, and we will present such analyses separately (Jaacks et al. in preparation). Here, we simply note that the expected total SFRD would be even higher than the red dot-dashed line of N400L10 run, and it would go right through the data range shown by the cyan and magenta shaded regions.

3.3.2.2 In which halos do galaxies sit?

So far, we have not considered the grouping of galaxies themselves (i.e., star and gas particles). To examine individual galaxies in our simulations, we group gas and star particles based on the baryonic density field rather than the dark matter. This allows us to identify galaxies directly, and then calculate properties such as their SFRs, stellar masses ($M_\star$, which we distinguish from $M_{\star,200}$), gas masses ($M_{\rm gas}$, which we distinguish from $M_{\rm gas,200}$) and metallicities. A more detailed description of this galaxy group finding process can be found in Nagamine et al. (2004c).

Together with the friends-of-friends halo finding, we are interested in how the grouped galaxies relate to the DM halos. To find out the matching between the two sets, we search for the nearest DM halo from the center-of-mass of each galaxy. We limit our galaxy sample to those with minimum 10 star particles, and those that reside in halos with at least 100 DM particles. Note that the DM structure between the Fiducial and H_2 runs are nearly identical, because they both use identical IC.

We can then make a scatter plot of corresponding $M_{\rm DM}$ and $M_\star$ of each halo as shown in Figure 23. In Panel (a) we see that the low mass galaxies ($M_\star \sim 10^6 - 10^9 M_\odot$)

at $z = 6$ in the two runs reside in different halos with different masses; the median result of the two runs lie almost an order of magnitude apart, with the Fiducial run galaxies residing in lower mass halos on average. This is because the SF requires a higher threshold density in the H_2 run and the gas requires a deeper potential-well of massive halos in order to form the same amount of stars as in the Fiducial run. The results of the two runs converge at higher masses ($M_{\rm DM} > 10^9 {\rm M}_\odot$), suggesting that those halos contain similar galaxies in the two runs. For higher mass halos with $M_{\rm DM} > 10^{11.5} {\rm M}_\odot$, there seems to be little difference in the SF between the two runs.

This ${\rm M}_\star - {\rm M}_{\rm DM}$ relation does not evolve significantly as time proceeds. For comparison, the dashed lines in Figure 23 represent the same scaling of $\log M_{\rm DM} = 0.8(\log {\rm M}_\star - 10) + 12$. The figure shows that the halos grow in mass with time, and the median lines slide up to top-right direction along the dashed line.

3.3.2.3 Gas mass fraction of simulated galaxies

Figure 24 shows the median gas fraction ($f_{\rm gas} \equiv {\rm M}_{\rm gas}/({\rm M}_{\rm gas} + {\rm M}_\star)$) of simulated galaxies as a function of galaxy stellar mass. In general, $f_{\rm gas}$ in the H_2 is higher than that in the Fiducial run, but the 1σ regions overlap with each other. The non-smoothness in the median lines in Panels (a) & (b) are simply due to the procedure of combining the data from multiple simulations with different resolution.

We find that the median lines do not evolve very much over time. At $z \leq 3$, $f_{\rm gas}$ declines steeply with ${\rm M}_\star$; from values close to unity at ${\rm M}_\star \sim 10^9 {\rm M}_\odot$ to $f_{\rm gas} \lesssim 0.1$ at ${\rm M}_\star \sim 10^{12} {\rm M}_\odot$. This suggests that the massive galaxies with ${\rm M}_\star \sim 10^{12} {\rm M}_\odot$ in our simulations have converted most of baryons into stars, and not much gas is left in them, coinciding with the downturn of the SFRD at these epochs (Figure 22).

Black triangles in Panels (b) & (c) are from a sample of galaxies at $z \sim 2$ (Erb et al., 2006). Simulated galaxies from the H_2 run tend to agree better with the observed data at $z = 3 \,\&\, 1$. In Panel (d) we show observational data of nearby

galaxies from McGaugh (2005, stars), Leroy et al. (2008, filled circles), and West et al. (2009, 2010, crosses). Neither the H_2 or Fiducial models agree well with observations at $z = 0$. This may in part be due to the limited mass resolution of the N600L100 run; a higher resolution run would resolve lower mass galaxies, possibly shifting the distribution to the left in better agreement with observations, if we were to make a composite plot from different runs. Another possible cause for this discrepancy is that too much unenriched gas has fallen into these massive galaxies between $z = 1$ and $z = 0$, pushing $f_{\rm gas}$ to higher values.

3.3.2.4 Metallicity of galaxies

As the gas recycling with metals takes place following star formation, the metallicity of galaxies should be roughly inversely proportional to their gas fraction if we neglect gas infall. In Figure 25, we compute the average metallicity of each galaxy by summing the SFR-weighted metallicity of all gas particles within grouped galaxies. Observational constraints on galaxy metallicities are derived from HII regions, therefore only the regions close to bright stars are probed, and a SFR-weighted metallicity is more appropriate for comparison than a mass-weighted metallicity. If we instead use a mass-weighted metallicity, we obtain much lower metallicity than the SFR-weighted one, because it would include unenriched gas in the outskirts of galaxies.

Figure 25 illustrates a general agreement with the above expectation: higher mass galaxies have lower $f_{\rm gas}$ and higher metallicity in general. In all four panels, we show model predictions from Savaglio et al. (2005) as black dotted lines. At $z = 6$ we find our simulations to be in rough agreement with the model at $M_\star > 10^8 M_\odot$, but below this mass we over-predict Savaglio's model result. At lower redshifts, the metallicity of simulated galaxies is always below that of Savaglio's model. The colored regions at $z = 0$ correspond to observations from Tremonti et al. (2004, dark grey), Kewley & Ellison (2008, magenta), and Lara-Lopez et al. (2012, yellow). In particular, Kewley

& Ellison (2008) have shown that the observational estimates of metallicity could vary significantly depending on the adopted estimator. The median of our Fiducial run overlaps with the magenta shade in a limited stellar mass range while the scatter overlaps the entire range. Our H_2 simulations however, are in excellent agreement with the magenta shade while under-predicting the metallicity of high mass galaxies with $M_\star \gtrsim 10^{10} M_\odot$ when compared to the dark grey and yellow shades.

If we do not weight by SFR, we find that the mass-weighted metallicity is much lower for the H_2 run, but the Fiducial run results are not so much affected. This is because, for a fixed baryonic density cut used in our galaxy grouping procedure (Nagamine et al., 2004c), the galaxies in the H_2 run will contain less star-forming gas than in the Fiducial run due to the higher H_2-formation (and hence SF) threshold, as we discussed in Figure 17.

3.3.2.5 Specific star formation rates of galaxies

Figure 26 shows the redshift evolution of the specific star formation rates (i.e., SFR per unit stellar mass, $\mathrm{sSFR} \equiv \mathrm{SFR}/M_\star$) in our simulations. This plot shows the instantaneous efficiency of SF, whereas the SHMR reflects all past history of SF and feedback. Panel (a) shows that the low mass galaxies in the H_2 run at $z = 6$ have higher sSFRs than those in the Fiducial runs, mirroring the steeper slope of the SFRD (Figure 22) for the H_2 run. Our simulation data is higher than the observational data of Lyman-α emitters at $z = 5.7$ & 6.6 (Ono et al., 2010) and z-dropout galaxies at $z \sim 7$ (Labbé et al., 2010), but within their error bars.

The H_2 run in Panel (b) ($z = 3$) again show a slightly higher sSFR than the Fiducial run for lower mass galaxies with $M_\star \lesssim 10^{9.6} M_\odot$. At higher masses, the two runs agree very well, as well as with the observed data at $z = 3.7$ & 2.0, indicated by the shaded region (Daddi et al., 2007; Lee et al., 2011). Panel (c) ($z = 1$) also shows similarly good agreement between the two runs and the observational data

range (Elbaz et al., 2007).

Panel (d) ($z = 0$) shows that the sSFR of both runs continue to decrease with time, but the H_2 run decreases at a faster rate. Therefore the Fiducial run has a higher sSFR than the H_2 model at $z = 0$. Both models agree with the observational data (Brinchmann et al., 2004) with a slightly decreasing sSFRD as a function of $M_\star$.

3.3.3 Galaxy stellar mass function (GSMF)

In the previous sections, we have seen that SF is less efficient in the H_2 run, which should also be reflected in the GSMF. Recall that for a given $M_\star$ at high-z, the galaxies reside in more massive halos in the H_2 runs (Figure 23). Since the higher mass halos are less abundant in a CDM universe, this will reduce the number of low-mass galaxies and shifts the galaxy population to higher mass DM halos.

Figure 27 shows the GSMF for our three primary runs (N400L10, N400L34, N600L100) at $z = 6$. In Panels (a-c) we directly compare the H_2 run to the corresponding Fiducial run for each simulation, and find that the H_2 run produces far fewer low-mass galaxies as expected. Note the different y-axis ranges in Panels (a-c). Our result is in general agreement with the findings of Kuhlen et al. (2012); they also found a decrease in their GSMF at $M_\star < 10^9 M_\odot$ at $z = 4$.

Figure 27d shows the comparison of the composite GSMF from the two runs, following the method of Jaacks et al. (2012a); we connect the GSMF from runs with different box sizes at the resolution limit of each run. This method allows us to cover a wider range of $M_\star$ utilizing many simulations, and present the results collectively. The observational estimate from González et al. (2010, yellow shade) at $z = 6$ is also shown. At high-mass end of $M_\star > 10^9 M_\odot$, the two composite GSMFs from H_2 and Fiducial runs agree well. The slight kink in the composite GSMF at $M_\star \sim 10^{8.8} M_\odot$ for the H_2 run is due to the resolution gap between the simulations; we have verified that an intermediate resolution run (N500L34, $\epsilon = 2.72h^{-1}$kpc) fills in this gap. Due

to the heavy computational load, we did not complete the corresponding Fiducial run for N500L34, therefore this run is not used for other comparisons in this paper. At the low-mass end of $M_\star < 10^8 M_\odot$, the H_2 run has significantly lower number density of galaxies than the Fiducial run. This illustrates that the H_2 model has a greater impact on the number density of low-mass galaxies.

3.3.3.1 On the overprediction of GSMF

One of the primary motivation for implementing the H_2-based SF model was to see if it can remedy the overprediction of GSMF at low-mass end due to its natural dependence on metallicity as we described in Section 3.1. In the earlier sections, we saw that indeed the H_2-based SF model reduces the number of low-mass galaxies. However, even with the new H_2 model, we are still over-predicting the number of low-mass objects at $M_\star = 10^{7.8} - 10^{8.6} M_\odot$ compared to the observational estimate of González et al. (2010) at $z = 6$ (Panel [d]). Therefore the H_2 model alone does not seem to be able to solve this generic problem of CDM model. Our simulations also seem to under-predict the number of massive galaxies with $M_\star > 10^{9.5} M_\odot$ when compared to the González et al. (2010) observational data at $z = 6$. Jaacks et al. (2012a) argued that this difference likely originates from the different slope in the $M_\star$−SFR relation, where the observational estimate was derived by using a crude relation from $z \sim 4$ and applied to $z = 6$ assuming that it is unchanged. In our simulations, the $M_\star$−SFR relation has a different slope, and this results in a different slope in the GSMF.

Figure 27d also contains the results of applying the duty cycle (DC) corrections (Jaacks et al., 2012b) to our composite GSMF both with (dot-dashed line) and without (dotted line) accounting for dust extinction. Jaacks et al. (2012b) defined the DC as the fraction of time that a galaxy exceeds the current HST magnitude limit within a certain Δz, and characterized it with a sigmoid function as a function of

$M_\star$. According to their result, DC for $z = 6$ makes a relatively sharp transition from nearly zero at $M_\star < 10^7 M_\odot$, crosses 0.5 at $M_\star \sim 10^8 M_\odot$, and to almost unity at $M_\star > 10^9 M_\odot$. Using this relation, we can apply a correction for the observability of low-mass galaxies, and see the impact of SF duty cycle on the observed GSMF. Similarly to the results of Jaacks et al. (2012b), our GSMF becomes closer to the observational estimate after the DC correction.

3.3.3.2 GSMF at $z = 3$ and 0

Figure 28 shows the GSMF at $z = 3$ (Panel a) & $z = 0$ (Panel b). Panel (a) is composed of data from the N400L34 & N600L100 runs, and Panel (b) of N600L100 data. Dashed lines represent the Fiducial run, while solid lines represent the H_2 run. The shaded regions at $z = 3$ represent observational estimates of the GSMF at $3 < z < 4$ (yellow) and $2 < z < 3$ (cyan) from Marchesini et al. (2009), following Choi & Nagamine (2010). Both sets of simulations are in agreement with each other and with observations at $M_\star \gtrsim 10^{10} M_\odot$, which corresponds to $M_{\rm DM} \gtrsim 10^{11.5} M_\odot$ (Figure 23b). A substantial difference between the two SF models is again seen in galaxies with $M_\star \lesssim 10^{10} M_\odot$, but this is below the current observable flux limit.

We may try to understand the discrepancies in the GSMF in relation to the SHMR. The difficulty is that the SHMR is not per unit volume, hence there is no obvious direct link between SHMR and GSMF. Suppose $M_\star$ in low-mass halos is increased uniformly, then the normalization of SHMR shifts upwards. At the same time, those galaxies would move from the low-mass bin to higher mass bins, and the GSMF would be weighted more towards higher mass side. For example, Figure 21b suggests that we are producing roughly correct amount of stars in halos with $M_{\rm DM} \lesssim 10^{12} M_\odot$ at $z = 3$, and the agreement in the GSMF is not so bad either as shown in Figure 28a. Such a comparison provides a consistency check between SHMR and GSMF.

The shaded region at $z = 0$ (Panel [b]) is the observational estimate from Cole

et al. (2001). Our simulations agree well with the observation near the knee of GSMF ($M_\star \sim 10^{10.8} - 10^{11.3} M_\odot$), but over-predicts at both low and high mass end. This over-estimation at $M_\star > 10^{11.3} M_\odot$ is reflected in the overestimation of the SHMR at $M_{\rm tot,200} \sim 10^{13} M_\odot$ (Figure 21d), which could be due to a lack of AGN feedback in our current simulations. At low-mass end ($M_\star \lesssim 10^{10.5} M_\odot$), both models over-predict the GSMF, but the H_2 run to a lesser degree.

It is clear that simultaneously matching the SHMR and GSMF is not an easy task. We expect the inclusion of AGN feedback will assist in improving the high-mass end of our simulations at low redshift. The new H_2-based SF model seems to have improved the relations in regards to the low-mass end, but does not fully reconcile the differences. Further improvements to our SN feedback prescriptions (e.g., momentum feedback by winds) may be required to achieve better agreement with observations.

3.3.4 Kennicutt-Schmidt (KS) relationship

Ideally we would like to reproduce the empirical Kennicutt-Schmidt relationship naturally in simulations; previously the KS relation was imposed in our SF prescription (Choi & Nagamine, 2010) and in many others', therefore the results matched the observation well by construction. The new H_2-based SF model provides two main benefits: it is not 'tweaked' to match the KS relation, and it is more physically realized in that stars are formed out of cold molecular gas on a depletion time-scale which is equal to about 1% of the free-fall time (i.e., with 1% efficiency per free-fall time).

To examine the KS relation, we calculate the column density of HI, H_2, and SFRs along the z-axis of each halo in our simulation on a uniform grid with a cell size of ϵ^2. A detailed description of this process can be found in Nagamine et al. (2004a). In Section 3.2.2, we stated that the H_2 model was accurate for $Z \geq 10^{-2} Z_\odot$, yet we set

our metal floor below that at $Z = 10^{-3} Z_{\odot}$. The model fails at low metallicities by over-predicting the amount of H_2 mass. This is due to time-dependent effects being neglected within the analytical KMT model (Krumholz & Gnedin, 2011). However, the over-predicted value may be an accurate estimate of how much cold material is present to form stars (Krumholz, 2012). Therefore we simply assume that the f_{H_2} value calculated by Equation (3.6) for any gas particle with $Z < 10^{-2} Z_{\odot}$ is actually representative of the amount of cold HI gas, which is available for star formation.

Figure 29(a-d) shows the KS relation for the N600L100 simulation at $z = 6, 3, 1,$ & 0. Each point in this figure represents one pixel on the projected x-y plane, and the contour is used to represent all the columns from all halos in the simulation box. For each redshift, the panel is broken down into three sub-panels: the first being the KS relation for HI gas only, second is for H_2 gas only, and lastly for HI $+H_2$. We will refer to these panels as KS-HI, KS-H2, and KS-HIH2, respectively. Each panel includes the KS relation given by Equation (3.3) as a solid red line, with the dashed lines representing the range of slope $\Delta n = \pm 0.15$.

In KS-HI panel at $z = 0$, we also overplot the observational data from seven nearby spiral galaxies as a blue hatched region (Bigiel et al., 2008, hereafter B08). In KS-H2 panel ($z = 0$), we overplot the low surface density observations from the Small Magellanic Cloud (SMC) as red triangles (Bolatto et al., 2011, hereafter known as B11). Lastly in KS-HIH2 panel ($z = 0$), we again plot B08 data as a blue hatched region, and B11 data from the SMC as a red hatched region.

There are two major processes driving the evolution of these plots. The first is gas depletion: as time passes the cold molecular gas used to form stars is depleted, and become less available at late times. This is most obvious in the decrease of $\Sigma_{\rm SFR}$ between $z = 3, 1, \& 0$, corresponding to the downturn of the SFRD at $z \lesssim 2$ in Figure 22. The second is metal enrichment: the longer a simulation runs, the more enriched the gas becomes via SF (Figure 25). This process expands the distribution

of points to the left-hand-side of the plot, because higher metal content allows stars to form at lower surface densities, as shown in Figure 16. The distribution of points broadens from $z = 6$ to $z = 0$, indicating greater range of metallicities present in the simulations.

The KS-HIH2 panel includes theoretical results from the KMT model (Krumholz et al., 2009) to show the same effect. The column densities calculated for each pixel represent the smoothed value on a relatively large projected scale of ϵ^2; if we use this value, the model will underpredict $f_{\rm H_2}$, since it does not account for clumping of the gas on scales below our simulation's spatial resolution limit of $\epsilon = 4.30\,h^{-1}$kpc, as well as the path-length along the column. To account for this effect, the KMT model multiplies the calculated gas column density by a clumping factor "c" ($\Sigma_{\rm HI+H_2} = c \times \Sigma_{\rm calc}$), which increases the surface densities to be compared with observations. In order to compare the KMT model result with our simulation, the theory lines are shifted to lower 'computed' surface densities (i.e., $\Sigma_{\rm calc} = \Sigma_{\rm HI+H_2}/c$), which brings a good agreement between the KMT model results and our simulations. In Figure 29, we adopted $c = 5$.

In the KS-H2 panels, our simulation is in good agreement with the observations of $z = 0$. The $\Sigma_{\rm SFR}$ starts high at $z = 6$, and eases its way to the lower left due to the two processes described above. At $z = 6$, the lower end of our simulation data overlaps with the observation at $z = 0$. Again this is a metallicity effect; our simulations do not contain enough high-metallicity columns, and the low metallicity columns will form stars at higher surface densities in KMT model. By $z = 1$ & 0, the observations of $z = 0$ lie in the center of our simulation data showing a very good agreement even for low surface densities. It should be noted that we are directly measuring the amount of H_2 in our simulation, whereas the observers infer this value from the CO luminosity.

In the KS-HIH2 panels, we find a disagreement between simulation and the B08

data (blue hatched region) until $z = 1$, where we begin to see minor overlap. The data in these panels is dominated by HI, resulting in similar trends to the KS-HI panel. Our simulation data begins to overlap the red hatched region immediately at $z = 6$, and fully encompasses the region by $z = 1$ again due to metallicity effects. By $z = 0$ the bulk of our data is found at slightly higher surface densities compared to these observations.

In the KS-HIH2 panel at $z = 3$ (Panel [b]), we also overlay the upper limits from damped Lyman-alpha absorbers (DLAs) as green circles and outskirts of Lyman-break galaxies (LBGs) as black squares (Wolfe & Chen, 2006; Rafelski et al., 2011). LBGs are considered to be star-forming galaxies with moderate median mass of $M_\star \sim 10^{10} M_\odot$, therefore are expected to have been enriched to some level. Rafelski et al. (2011) find the LBGs in their sample have $Z \approx 0.07 - 0.26\, Z_\odot$. Figure 30 shows the KS plot for only star-forming columns in our N600L100 simulation with $Z = 0.07 - 0.26\, Z_\odot$ at $z = 3$. The observed data points are close to the edge of the simulation contour, but there are many columns that agree with the observational data. Note that it is certainly easier to observe the SFR closer to the upper edge of the contour rather than the bottom side of it due to the surface brightness dimming.

Figure 31 further illustrates the metallicity effect by separating the KS-HIH2 panel from Figure 29d into three different metallicity ranges for the N600L100 run at $z = 0$. We find that the columns with the lowest metallicity (Panel [a]) are forming stars at the highest gas surface densities for a given $\Sigma_{\rm SFR}$ as expected. Panel (b) brackets $Z = 0.2\, Z_\odot$, which is roughly equal to the metallicity of the SMC (Bolatto et al., 2011). Columns in our simulation in this metallicity range agree very well with the observed data (red contour). In Panel (c) we show columns of higher metallicity $Z > 0.3\, Z_\odot$, which is similar to the range of B08 sample ($0.41 - 0.69\, Z_\odot$) (Walter et al., 2008). As discussed previously, our data does not agree very well with observations in this range. There are some points overlapping with the observed data, but the

majority lie at higher column densities than the observed range. This discrepancy is presumably caused by different metallicities: the highest metal column at $z = 0$ in the N600L100 run is $Z = 1.26\,Z_\odot$, yet the median column metallicity at $Z > 0.3\,Z_\odot$ is $Z = 0.41\,Z_\odot$. This suggests that our N600L100 run does not contain enough high metallicity columns to match these observations. If the simulation had more high metallicity columns, then the SF would occur more at lower gas surface density, and there would be more points overlapping with the B08 data.

3.3.5 HI & H_2 column density distribution functions

One of the best ways to investigate the distribution of HI gas in the Universe statistically is to examine the HI column density distribution function $f(N_{\rm HI})$ (e.g., Nagamine et al., 2004b,a; Wolfe et al., 2005; Zwaan & Prochaska, 2006; Prochaska & Wolfe, 2009; Noterdaeme et al., 2009; Pontzen et al., 2010; Altay et al., 2011; Yajima et al., 2011; Rahmati et al., 2012; Erkal et al., 2012). Using the Fiducial runs, Nagamine et al. (2010) found that a simple self-shielding model with a threshold density ($n_{\rm th}^{\rm UV} = 6 \times 10^{-3}\,{\rm cm}^{-3}$) for UVB penetration can reproduce the observed $f(N_{\rm HI})$ quite well at $\log N_{\rm HI} < 21.5$ for $z = 3$. Yajima et al. (2011) later showed the validity of $n_{\rm th}^{\rm UV}$ value using full radiative transfer calculations. However, Nagamine et al. (2010) also found that the Fiducial run over-predicts $f(N_{\rm HI})$ at $\log N_{\rm HI} > 22$, and argued that this might be due to the neglect of H_2 within the Pressure SF model (Section 3.2.1.2), because then part of HI would be converted into H_2 and $f(N_{\rm HI})$ would decrease at high $N_{\rm HI}$ values.

Figure 32 compares the column density distributions of both HI and H_2 in the H_2 and Fiducial runs at $z = 6, 3, 1, \& 0$. Panels (a) & (b) are composed of N144L10 data, while Panels (c) & (d) are composed of N600L100 data. The Fiducial run is omitted from panels (c) & (d), because the N600L100 Fiducial run did not use the OTUV threshold which is necessary to bring the column density distribution into agreement

with observations at $z = 3$ (Nagamine et al., 2010).

In Panel (a) we see that the H_2 run consistently has higher amplitude of $f(N_{\rm HI})$ than the Fiducial run due to less efficient star formation. At $z = 3$ (b) however, we find that the H_2 run has a higher $f(N_{\rm HI})$ than that of Fiducial run at $\log N_{\rm HI} > 22$. This is because the star formation is less efficient in the new H_2 run, therefore more HI gas is left over in high density regions. In the H_2 run the varying SF threshold density was higher than the constant $n_{\rm th}^{\rm SF}$ adopted in the Fiducial run (Figure 17), and it was also clear from Figure 18 that the gas particles are reaching higher densities in the H_2 run before being heated by SN feedback than in the Fiducial run. The $f(N_{\rm HI})$ results at the lower $N_{\rm HI}$ do not change between the two runs at this redshift. Panels (c) & (d) continue to show the redshift evolution of this relationship in our simulations. At $z = 0$, we find that our simulations over-predict $f(N_{\rm HI})$ at $\log N_{\rm HI} > 21$, over-predict the $f(H_2)$ at $\log N_{\rm H_2} < 21$, and under-predict at $\log N_{\rm H_2} > 22$.

Therefore the current simulations suggest that it is difficult to explain the sharp turn-down of observed $f(N_{\rm HI})$ at $\log N_{\rm HI} \sim 22$ by the atomic-to-molecular transition, in agreement with the conclusions of Erkal et al. (2012). Additionally, Erkal et al. (2012) showed that their simulations could be brought into agreement with observations if a region of 3 kpc radius around the center of all galaxies was removed. This could be another opportunity for AGN feedback to play an important role: if feedback from super massive black holes can prevent the formation of high columns, then our simulations may come into better agreement with observations at $N > 10^{22}{\rm cm}^{-2}$. Obviously more refinement of feedback models are needed to bring the simulations into agreement with the observations of $f(N_{\rm HI})$ and $f(N_{\rm H_2})$.

3.3.6 Resolution studies

The new H_2-based SF model has implicit resolution dependence. With higher resolution, the simulation resolves higher (column) densities (Eq. 3.9), which yield

lower s values (Eq. 3.11) for a given metallicity. Figure 16 illustrates that lower s values lead to higher $f_{\rm H_2}$ (Eq. 3.6), which increases the SFR (Eq. 3.14).

To examine the resolution effect, Figure 33 shows the KS relation for the N600L10, N400L10, N400L34, & N600L100 runs at $z = 6$. These panels are ordered by resolution: Panel (a) shows the highest resolution, and Panel (d) shows our lowest resolution simulation. In Panels (a) & (b), we can examine the resolution effect on the KS plot when keeping the box size constant. In general the gas surface densities where SF takes place do not change very much, but with higher resolution, the points cover a wider range of $\Sigma_{\rm SFR}$. This is an expected result from a higher resolution simulation; the additional resolution allows the gas to collapse to higher densities, yielding additional shielding which eases the transition to H_2.

While Panels (a) & (b) are both from simulations with a box size of comoving $10h^{-1}$ Mpc, Panels (c) & (d) are from simulation boxes of $34h^{-1}$Mpc and $100h^{-1}$Mpc, respectively. Increasing the box size of a simulation usually comes with a price of decreasing the resolution, and it results in more higher mass halos and fewer low-mass halos (e.g., Thompson & Nagamine, 2012). Note that the simulations shown in Panels (c) & (d) are of lower resolution than those in Panels (a) & (b). When comparing the L10 boxes with the L34 & L100 boxes, we are actually examining the resolution and box size effects simultaneously. Comparing all the panels in Figure 33 suggests that our KS results are not significantly affected by these resolution effects. The only visible effect we see in the figure is that the lower resolution results in a thinner contour distribution

3.3.6.1 Probability Distribution Function (PDF) of H_2 *density*

Physical number densities of observed molecular clouds are on the order of a few hundred cm^{-3}, in rough agreement with the highest densities achieved in our current cosmological simulations. Figure 34 shows the mass-weighted PDF of H_2

number density at the highest densities in our simulations at $z = 6$. As expected, we can see that the peak of the highest density region shifts to higher densities as the resolution increases; the lowest resolution production run (N600L100) has a peak at $n_{\rm H_2} \sim 10^2\,{\rm cm}^{-3}$, and our highest resolution production run (N400L10) has a peak at $n_{\rm H_2} \sim 10^{3.6}\,{\rm cm}^{-3}$. However, the N400L10 run has a slightly different shape from the other runs, and the higher resolution N600L10 run has a peak at a slightly lower value of $n_{\rm H_2} \sim 10^{2.8}\,{\rm cm}^{-3}$. The exact reason for this different PDF shape is unclear, but presumably it was affected by some SF events.

Earlier, Jaacks et al. (2012a) showed that the Fiducial runs do not satisfy the Bate & Burkert (1997) mass resolution criteria, even though gas particles in our N400L10 have particle masses lower than the typical Jeans mass at $z = 6$ by a factor of $\approx 1 - 100$. This prevents us from explicitly resolving the collapse of star forming molecular clouds directly, and it is one of the primary reasons for employing a sub-grid model for SF using the KMT model. Given that the highest densities reached in our simulations is approximately equivalent to those of observed giant molecular clouds, we consider that the KMT is suitable to use as a sub-grid model in our simulation to estimate the H_2 mass for star formation. In fact, the KMT model is well suited to predict the galactic-scale trends in atomic and molecular content rather than the structure of individual photo-dissociation regions (Krumholz et al., 2008; Kuhlen et al., 2012).

3.4 Summary

We have implemented a new H_2-based SF model in our cosmological SPH code GADGET-3 . Previous SF models did not consider the formation of H_2, and imposed the KS relation in their SF prescriptions. The analytic KMT model has provided a computationally inexpensive way to estimate the H_2 mass fraction in cosmological hydrodynamic simulations, which allows us to modify our SF prescription to compute

the SFR based on H_2 density rather than total gas density. The model brings a natural dependence of star formation on metallicity (in addition to the previous dependence through metal line cooling).

We performed a series of cosmological simulations with different box sizes and resolutions, and examined how this new H_2-based SF model affected the results such as stellar-to-halo mass ratio, cosmic SFRD, galaxy specific star formation rates, galaxy stellar mass function, Kennicutt-Schmidt relationship, and HI column density distributions. We find that this new H_2-based SF model provides many advantages over previous models, and we summarize our primary conclusions below.

- In the new H_2-based model, each gas particle has different SF threshold densities based on its metallicity (Figure 17). We have shown that the new SF threshold densities (i.e., metallicity-dependent density required for H_2 formation) are higher than the constant threshold density used in the Fiducial run, which results in overall decrease of SFRD (Figure 22) in the new model. Decrease of star formation leads to weaker feedback effects subsequently. The need for sufficient shielding from radiation field for H_2 formation results in lower SFR, causing a gas reservoir to build up. Consequently, SF starts later than in the Fiducial run, and the peak of SFRD has slightly shifted to a lower redshift. But both runs are still compatible with the observed range of SFRD in the Lilly-Madau diagram.

- The H_2 run is able to successfully reproduce the SHMR at $z = 3$ & 6 for lower mass halos with $M_{\rm tot,200} < 10^{12}{\rm M}_\odot$ (Figure 21). The Fiducial run with previous SF model significantly overpredicts SHMR at the same mass range, therefore the H_2 run provides a significant improvement on this aspect. Since the SN feedback model was kept the same in the two runs, this improvement was purely driven by the change in the SF model, rather than the feedback.

Both runs overpredict the SHMR in halos $M_{\rm tot,200} > 10^{12}{\rm M}_{\odot}$ at $z < 3$, which might be due to lack of AGN feedback in our current simulations. This is connected with the over-prediction of GSMF at the high-mass end in our simulations.

- The sSFRs of galaxies in the H_2 and Fiducial runs are in rough agreement with observations, and they decrease systematically with decreasing redshift. At $z = 6$, the H_2 run have higher sSFR for galaxies with ${\rm M}_{\star} < 10^{10}{\rm M}_{\odot}$, but this is due to the fact that the galaxies with same ${\rm M}_{\star}$ reside in higher mass halos in the H_2 runs than in the Fiducial run (Figure 23). At later times, this difference becomes much smaller and the two models are in rough agreement with one another.

- We find that the H_2-based SF model produces significantly fewer galaxies at ${\rm M}_{\star} < 10^{8}{\rm M}_{\odot}$ compared to the Fiducial run at $z = 6$ (Figure 27d). Even after this reduction, the faint-end slope of GSMF in the H_2 run is still steeper than what has been observationally estimated at $z = 6$. Employing duty cycle corrections following Jaacks et al. (2012b) brings the GSMF closer to observations.

  At $z = 3$ we find that our simulations are in good agreement with observed GSMFs at ${\rm M}_{\star} > 10^{10}{\rm M}_{\odot}$, consistently with our previous finding in Choi & Nagamine (2010). At the lower masses of ${\rm M}_{\star} < 10^{10}{\rm M}_{\odot}$, again the H_2 model produces fewer number of low-mass galaxies relative to the Fiducial run. At the moment, the flux limit of GSMF data is ${\rm M}_{\star} \sim 10^{10}{\rm M}_{\odot}$ even with the deepest HST imaging, and there are no good data below this limit. Galaxies with ${\rm M}_{\star} < 10^{10}{\rm M}_{\odot}$ correspond to halos with $M_{\rm DM} < 10^{12}{\rm M}_{\odot}$, and in this regime the new H_2 run agrees with the observational estimate of SHMR much better than the Fiducial run. For this reason, we expect that the H_2 run would match the observations of GSMF better in the future at ${\rm M}_{\star} < 10^{10}{\rm M}_{\odot}$.

Finally at $z = 0$, we find that our simulations over-predict the GSMF at both low and high-mass end. The deviation at the low-mass end seems smaller than at the high-mass end, however, since this is a log-log plot, the actual deviation is greater at the low-mass end. Further improvement in our feedback prescriptions (e.g., momentum-driven feedback by SN and AGN) may be needed to reconcile these differences.

- We find that the new H_2-based SF model naturally produces the empirical Kennicutt-Schmidt relationship without the need for 'tweaking' the parameters of the SF model. The most significant discrepancy between the H_2 run and observation can be seen against the nearby spiral galaxy data of Bigiel et al. (2008). It seems that the H_2 run does not contain enough high-metallicity columns to match observations of nearby spiral galaxies, and the same trend can be seen in the galaxy mass-metallicity plot (Figure 25). These discrepancies indicate that our current simulations might have too much low-metallicity gas in massive galaxies at $z < 2$, which is also indicated by Figure 24d. However the H_2 run is able to match the observations of DLAs and LBGs at $z = 3$, as well as the observations of the low-metallicity SMC by $z = 0$.

- As for the hydrogen column density distribution function, we find that the new H_2 model did not improve the agreement with observation at $\log N_H > 21.6$ at $z = 3$, and we still over-predict $f(N_{\rm HI})$ similarly to the previous simulations. Erkal et al. (2012) also concluded that the atomic-to-molecular transition alone could not account for the downturn in $f(N_{\rm HI})$ at $\log N_H > 21$. At $z = 0$, our simulations do not agree with the observational data of Zwaan & Prochaska (2006), and further refinement of star formation and feedback models are needed.

As for our future plan, we intend to improve our simulations on a few fronts, given the problems that we observed in this paper. Since the $f_{\rm H_2}$ calculated in the KMT

model depends on gas metallicity, we need to account for the metal diffusion in the ISM more accurately (e.g. Shen et al., 2010). Our current SPH code does not allow for particles to share their metal content with one another, and we plan to implement and explore the effects of metal diffusion in the near future. Finally, as a comparison to the H_2-based SF model, we also plan to develop a turbulence-based SF model and and explore the differences between the two approaches to star formation.

The author thanks the co-authosr of this paper Dr. Kentaro Nagamine, Dr. Jun-Hwan Choi, and Jason Jaacks for their time and dedication. We are grateful for the helpful and insightful discussions with Mark Krumholz, and Volker Springel for providing us with the original version of GADGET-3 .

Run Name	Box Size $[h^{-1}$ Mpc]	Particle Count DM & Gas	$m_{\rm dm}$ $[h^{-1}$ M$_\odot]$	$m_{\rm gas}$ $[h^{-1}$ M$_\odot]$	ϵ $[h^{-1}$ kpc]	$z_{\rm end}$ H_2	$z_{\rm end}$ Fiducial	OTUV H_2	OTUV Fiducial
N144L10	10.00	2×144^3	2.01×10^7	4.09×10^6	2.77	3.00	3.00	Y	Y
N500L34	33.75	2×500^3	1.84×10^7	3.76×10^6	2.70	3.00	-	Y	-
N600L10	10.00	2×600^3	2.78×10^5	5.65×10^4	0.67	6.00	-	Y	-
N400L10	10.00	2×400^3	9.37×10^5	1.91×10^5	1.00	6.00	5.50	Y	N
N400L34	33.75	2×400^3	3.60×10^7	7.34×10^6	3.38	3.00	1.00	Y	N
N600L100	100.00	2×600^3	2.78×10^8	5.65×10^7	4.30	0.00	0.00	Y	N

Table 5 Simulation parameters used in this work. The first three simulations were used to perform tests of the H_2 model and resolution study (Section 3.3.6). The second set of three simulations are the main production runs used to compare with previous SF models. The quantities $m_{\rm dm}$ & $m_{\rm gas}$ are the particle masses of dark matter and gas particles, ϵ is the comoving gravitational softening length, and $z_{\rm end}$ is the ending redshift of each simulation. The H_2 simulations (along with N144L10 Fiducial) use an optically-thick ultra-violet threshold or 'OTUV' (see Section 3.2.3; Nagamine et al., 2010).

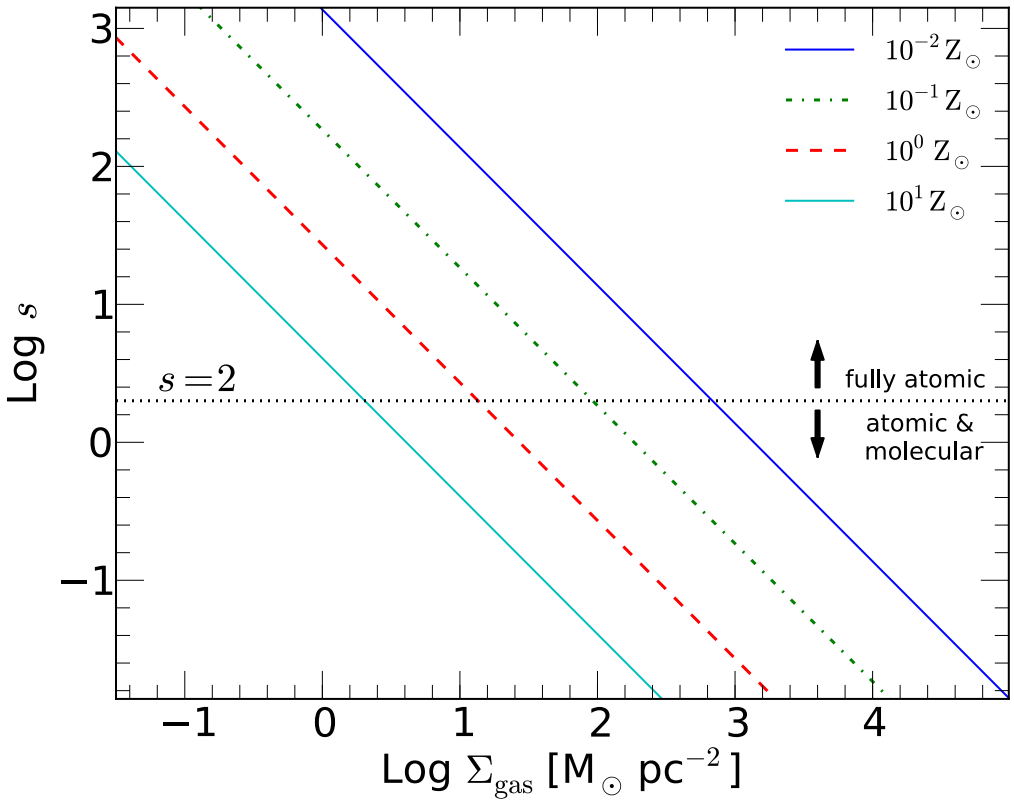

Figure 16 The parameter s (Equation 3.11) as a function of gas surface density for different metallicities. The value of $s = 2$ corresponds to the transition from fully atomic gas to atomic & molecular within the KMT model. Lower metallicity gas requires larger column densities (i.e., more shielding) in order to form H_2.

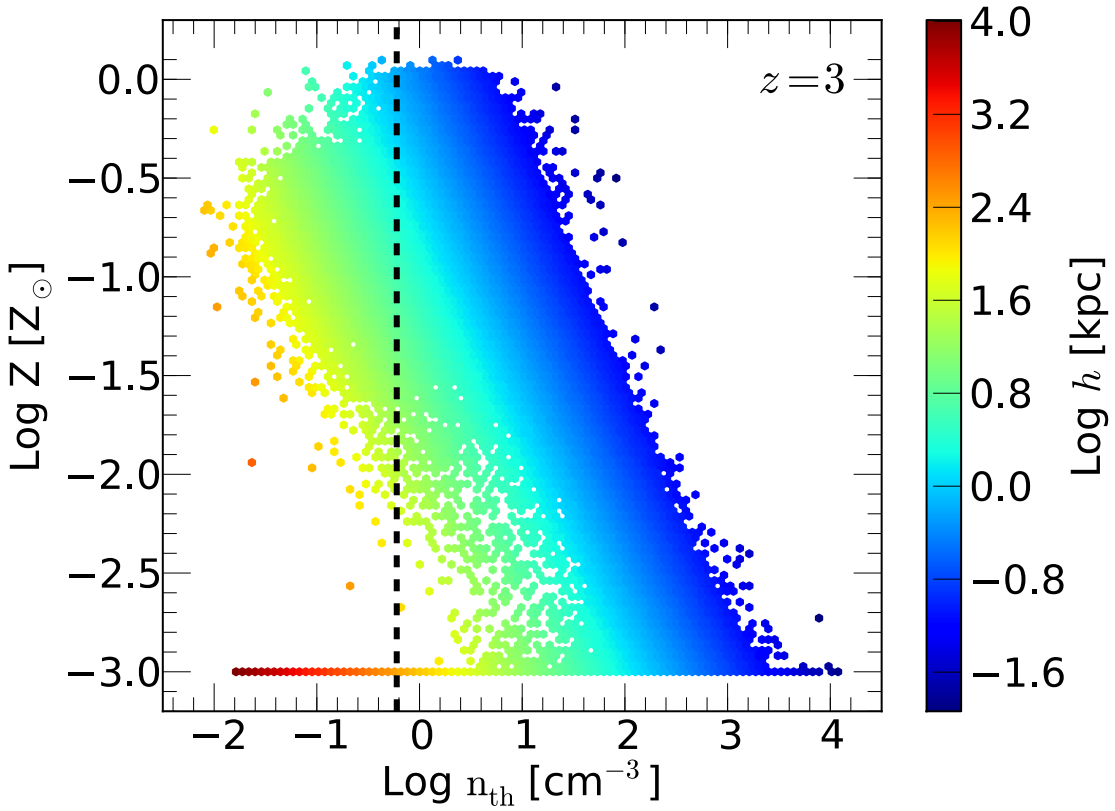

Figure 17 Physical density threshold (Eq. [3.16]) for H_2 formation of all particles within a low resolution run (N144L10) at $z = 3$. Color gradient corresponds to the median scale-height h (Eq. [3.10]) as indicated by the color bar. The black dashed line represents the physical SF density threshold of $n_{th}^{SF} = 0.6\,cm^{-3}$ used in our previous SF models (Choi & Nagamine, 2010) . The KMT model generally requires higher densities to form H_2 and hence be eligible for SF, compared to the Fiducial model.

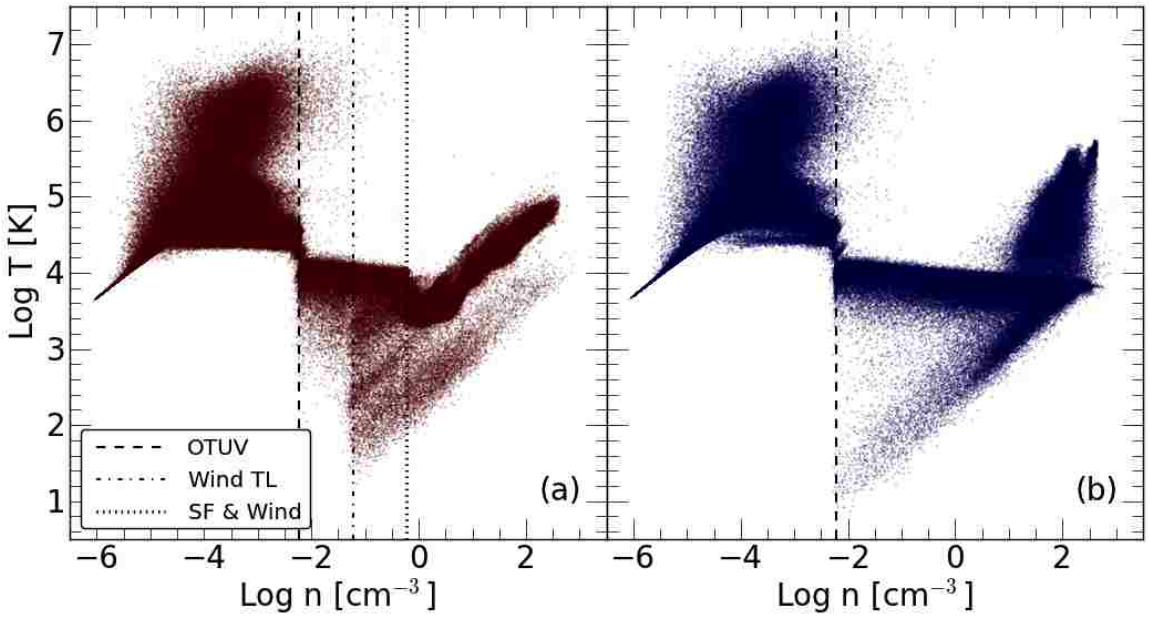

Figure 18 Gas temperature vs. number density phase diagrams for the low resolution N144L10 runs at $z = 3$. *Panel (a)*: the Fiducial run. The right-most dotted line is the physical SF and wind density threshold ($n_{th}^{SF} = 0.6 cm^{-3}$, Section 3.2.3), the middle dot-dashed line is the maximum wind travel length (TL) discussed in Section 3.2.3, and the left-most dashed line corresponds to the OTUV threshold discussed in Section 3.2.3. *Panel (b)*: H_2 run. Here only the OTUV threshold is shown. There is no fixed SF density threshold, as it is different for every particle depending on the metallicity and surface density as described in Section 3.2.2.3.

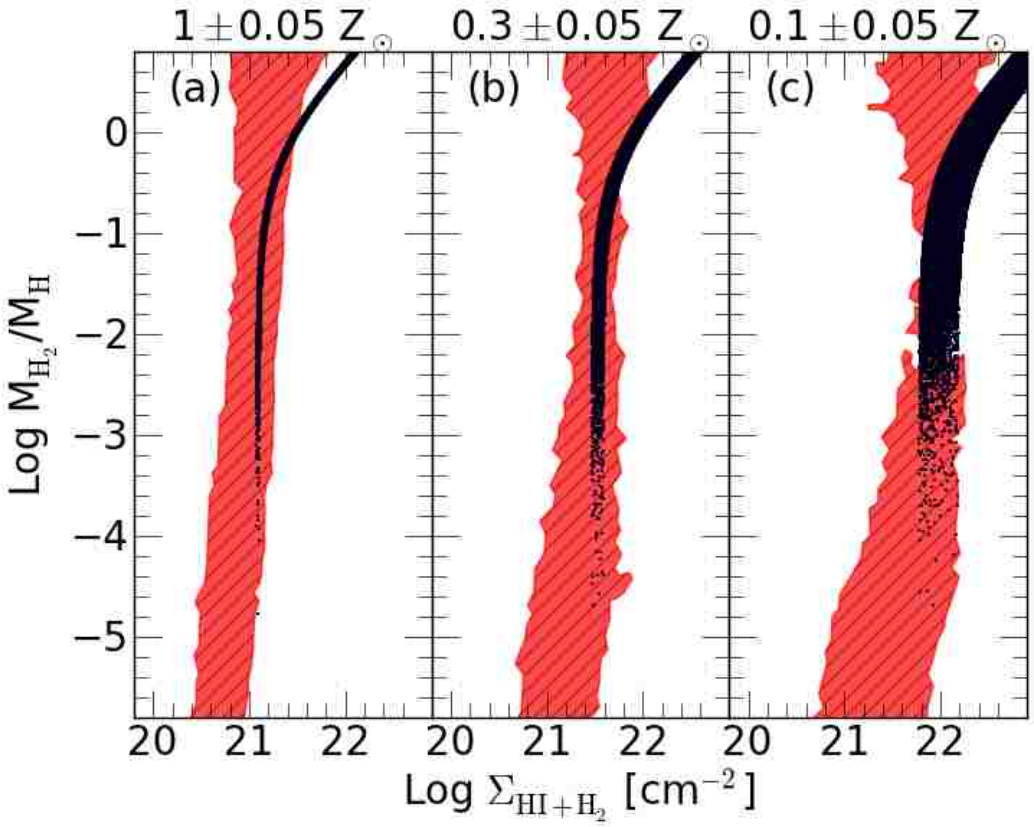

Figure 19 H_2 mass fraction as a function of HI+H_2 surface density within our N600L10 run (black points) at $z = 0$ for three different metallicity ranges. The red shaded regions show the results of three Milky Way-like simulations of Christensen et al. (2012) using a full non-equilibrium H_2 model with different metallicities of (a) $1Z_\odot$, (b) $0.3Z_\odot$, and (c) $0.1Z_\odot$.

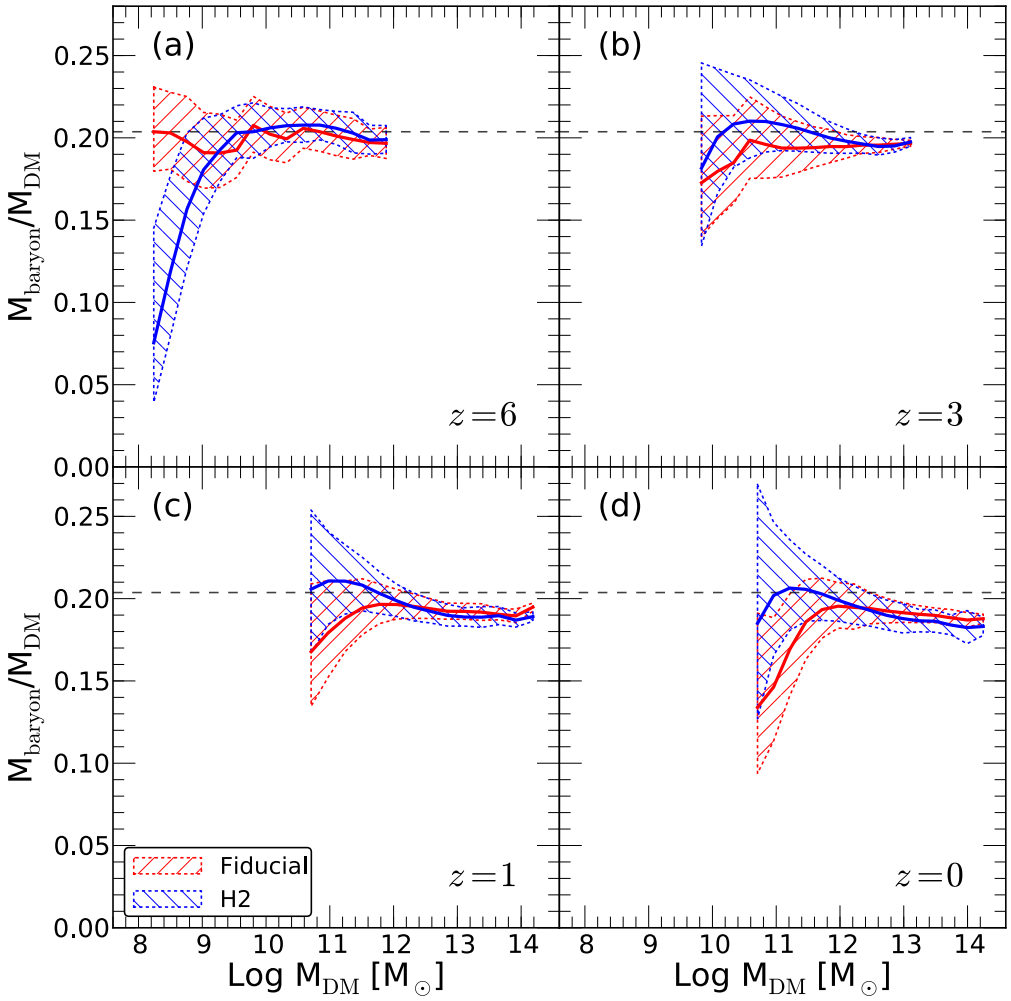

Figure 20 Baryon mass fraction within r_{200} of each halo, $f_b \equiv (M_{gas,200} + M_{\star,200})/M_{DM}$, as a function of halo mass (only DM) for $z = 6, 3, 1, \& 0$. The red and blue solid lines represent the median points in each mass bin for the Fiducial and H_2 runs, respectively. The hatched regions represent 1σ scatter in each M_{DM} bin. The cosmic mean baryonic fraction (Ω_b/Ω_{DM}) is represented by the dashed horizontal line.

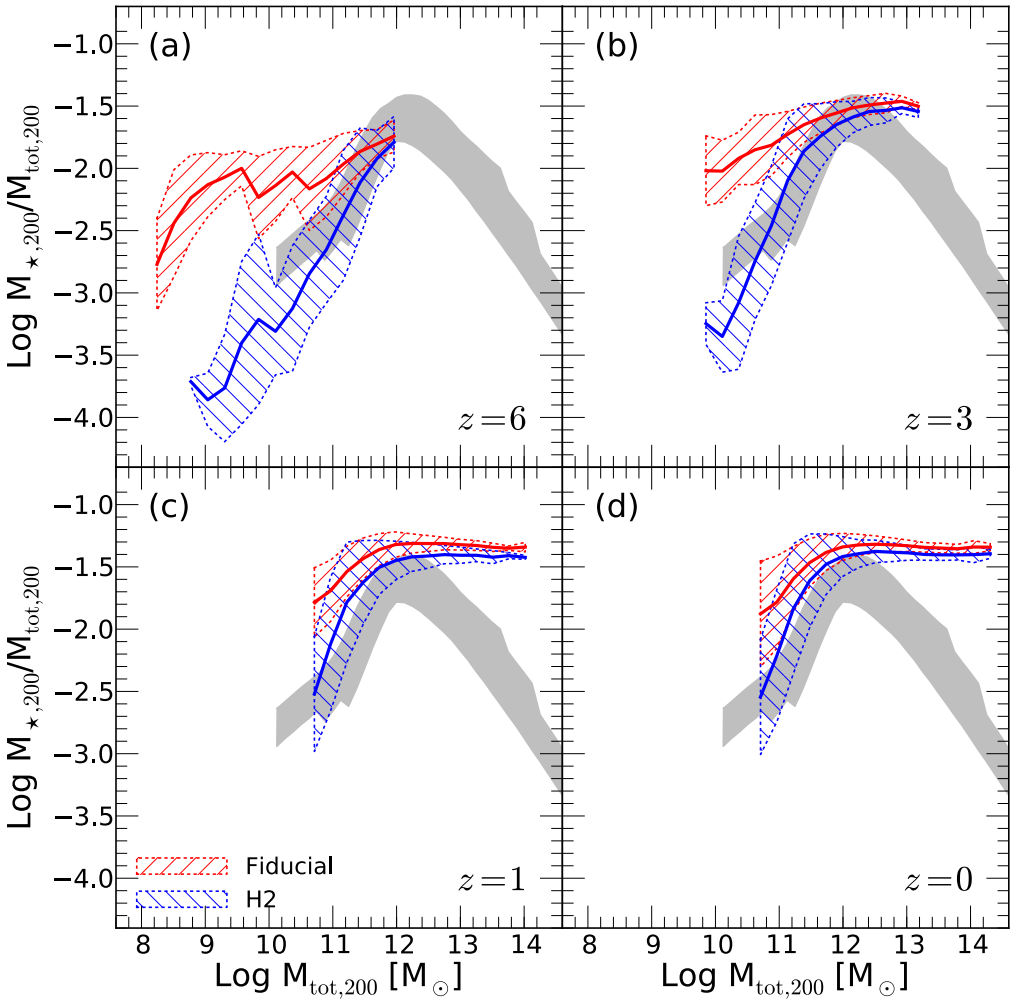

Figure 21 The SHMR as a function of total halo mass (DM+baryons) within r_{200}. The data from semi-analytic models and observations are shown as the grey shade, which is identical in all four panels as it doesn't evolve very much with redshift (Behroozi et al., 2012).

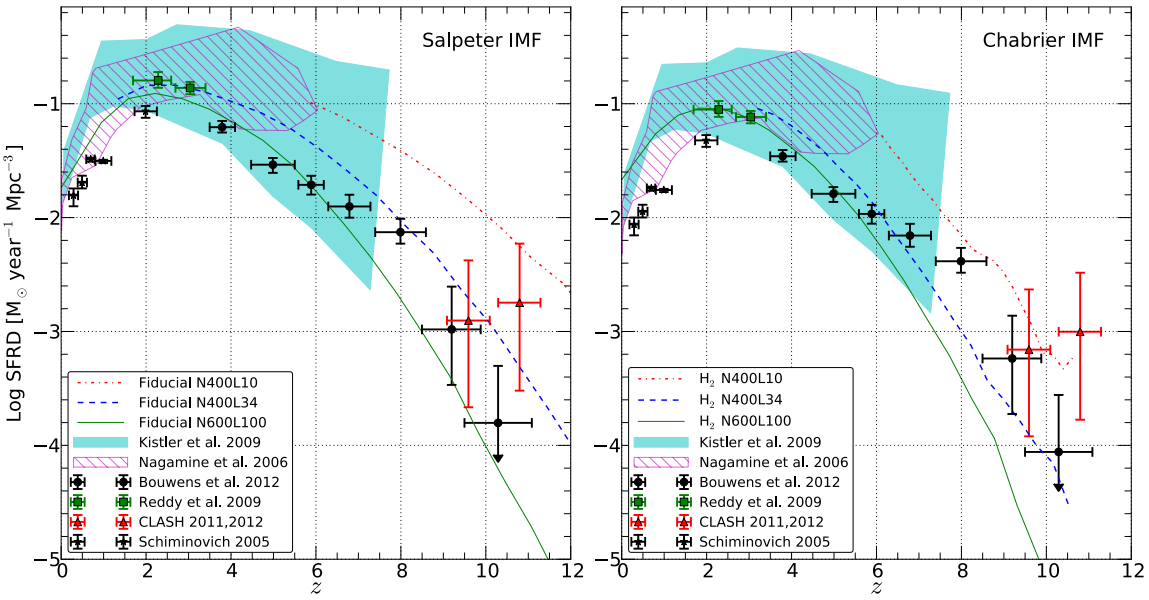

Figure 22 Cosmic SFRD for our simulations compared to some observations. The left panel is for the Salpeter IMF, and the right for Chabrier IMF. The Fiducial runs are using Salpeter IMF, and the H_2 runs are using Chabrier IMF. The observational data are from: the CLASH program (Postman et al., 2012; Coe et al., 2012, red triangles), Bouwens et al. (2011, 2012, black circles), Reddy & Steidel (2009, green crosses), Schiminovich et al. (2005, black stars), Kistler et al. (2009, cyan shade), and Nagamine et al. (2006, magenta hatched region). All observational data are corrected for dust extinction by each author as they deemed appropriate.

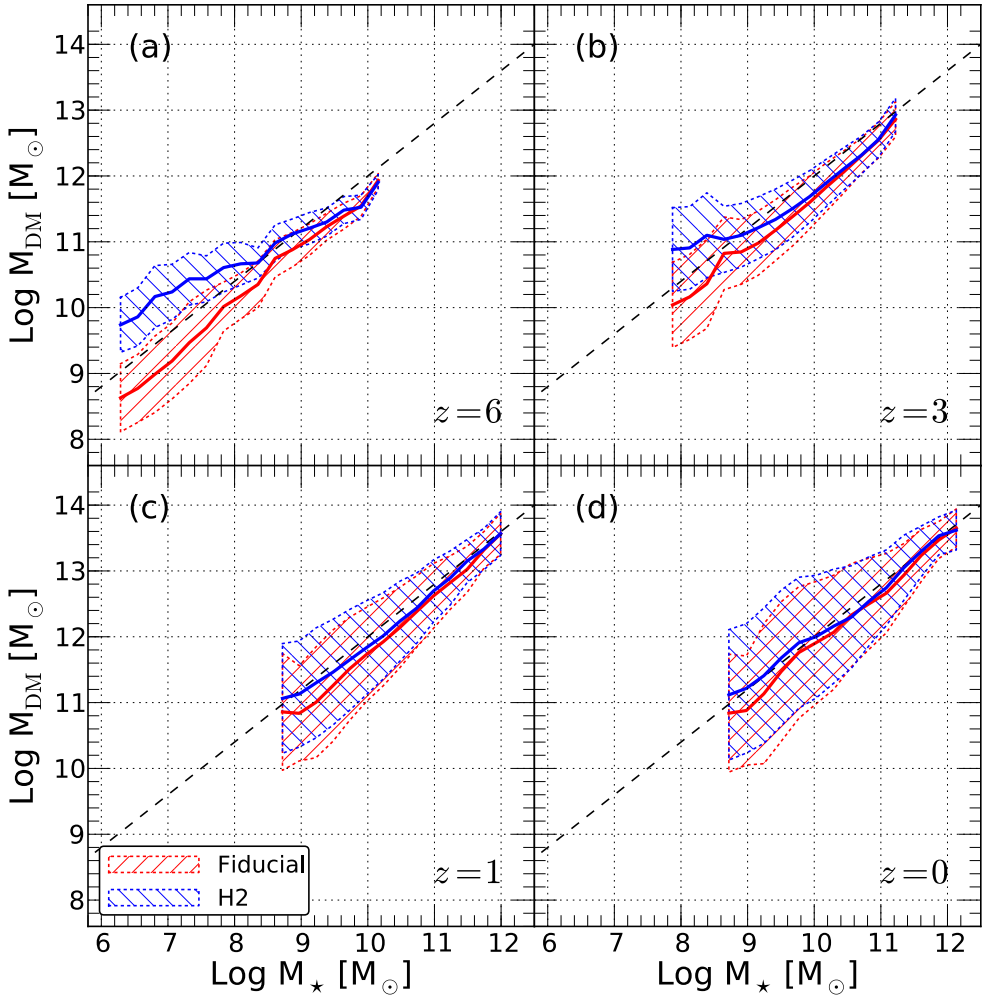

Figure 23 Relationship between the masses of simulated galaxies (identified by the friends-of-friends grouping) and their nearest DM halos. Note that $M_\star$ is not exactly same as $M_{\star,200}$. We see that the low-mass galaxies with $M_\star \sim 10^6 - 10^9 M_\odot$ at $z = 6$ reside in more massive DM halos in the H_2 runs than in the Fiducial run. The dashed line in each panel represent the scaling of $\log M_{DM} = 0.8(\log M_\star - 10) + 12$, which is a simple eye-ball fit at $z = 0$.

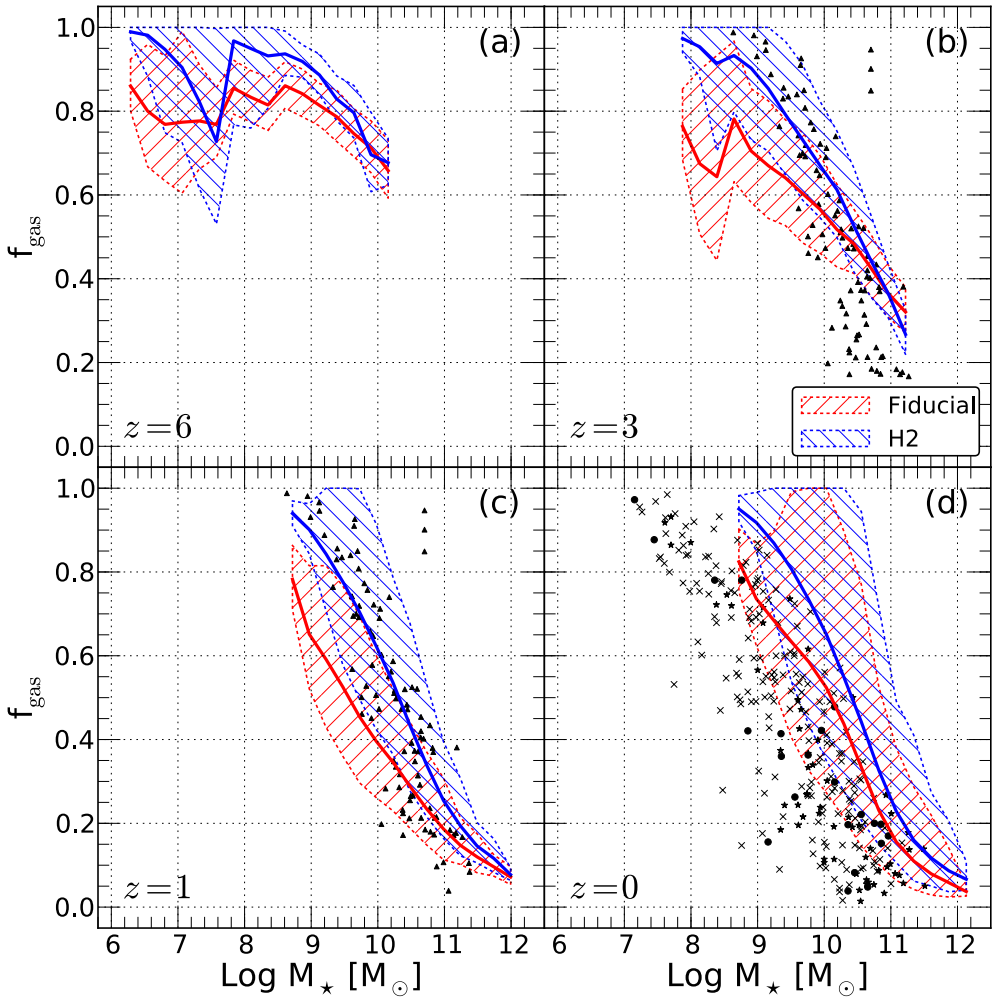

Figure 24 Gas mass fraction $f_{\rm gas} = {\rm M_{gas}}/({\rm M_{gas}} + {\rm M_\star})$ of simulated galaxies as a function of galaxy stellar mass. Black triangles in Panels (b) & (c) are observed galaxies at $z \sim 2$ (Erb et al., 2006). In Panel (d) we show observational data at $z = 0$ taken from Peeples & Shankar (2011).

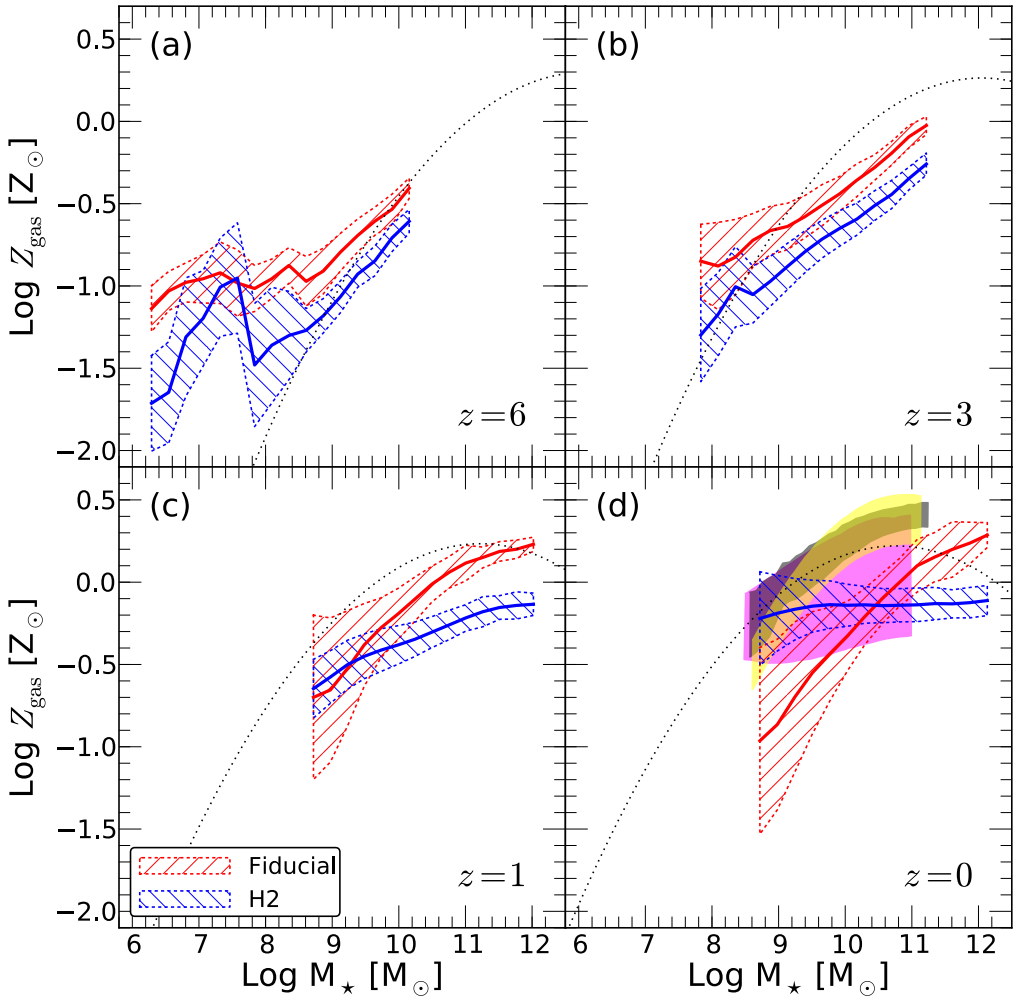

Figure 25 Gas metallicity of simulated galaxies as a function of galaxy stellar mass. Black dashed line in all panels is the theoretical model from Savaglio et al. (2005). Colored contours in Panel (d) correspond to observational data from Tremonti et al. (2004, dark-gray), Kewley & Ellison (2008, magenta), and Lara-Lopez et al. (2012, yellow).

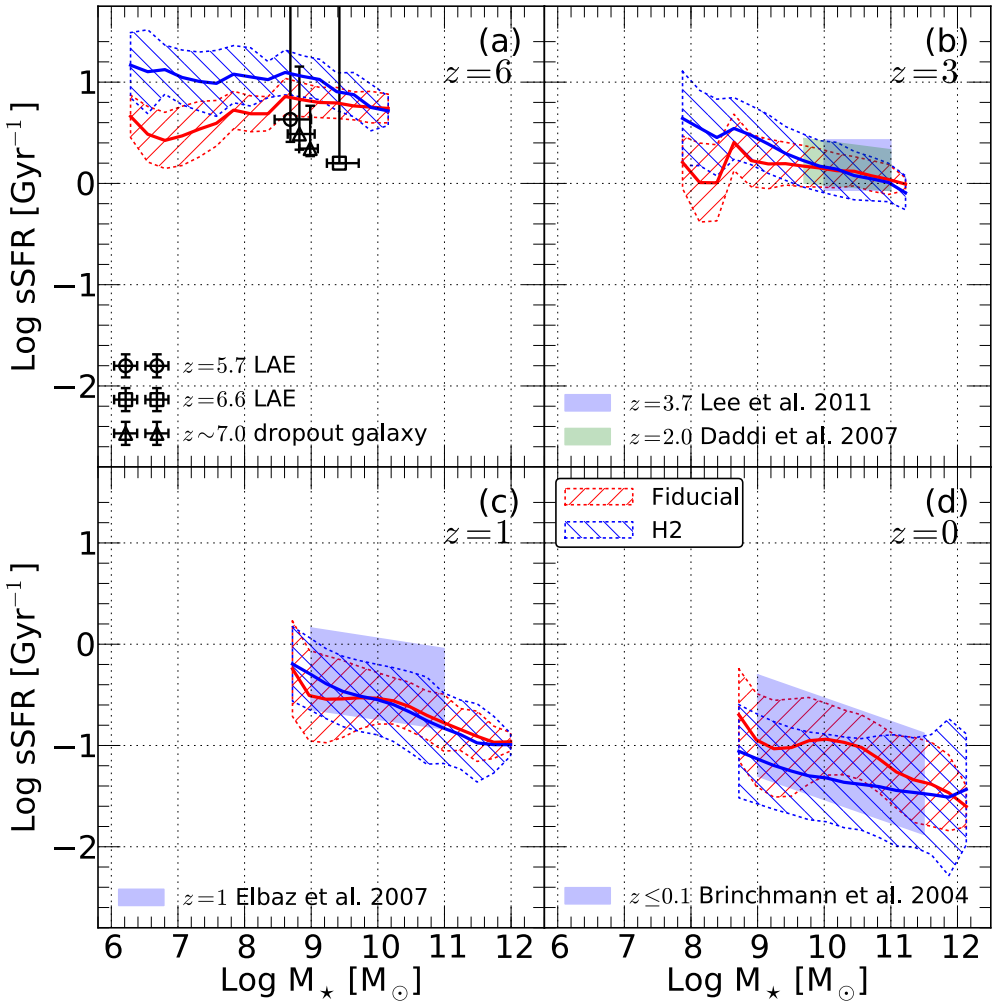

Figure 26 Specific star formation rate (sSFR $\equiv$ SFR/M$_\star$) of simulated galaxies as a function of galaxy stellar mass. The observed data ranges are indicated by the shaded region with the source indicated in each panel. Observational data was taken from Krumholz & Dekel (2011).

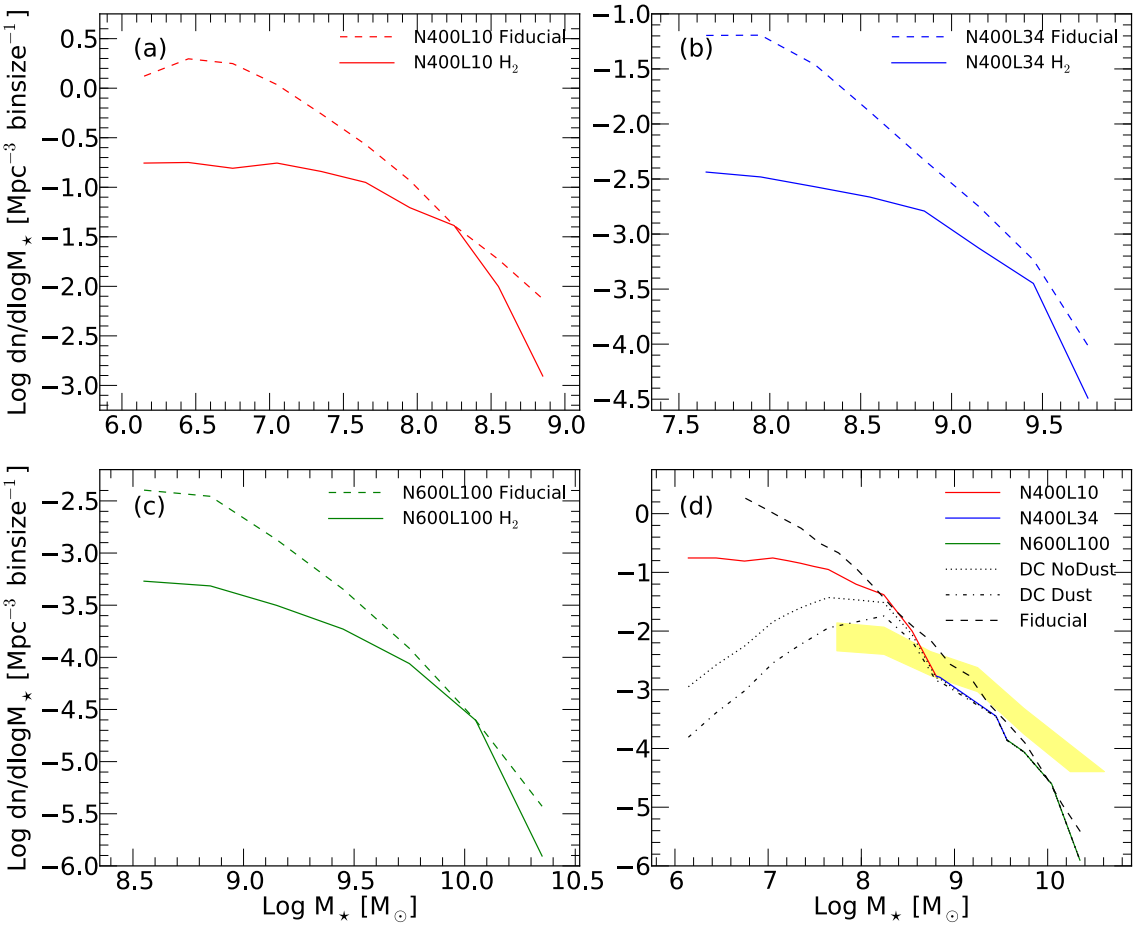

Figure 27 *Panels (a-c)*: Galaxy stellar mass function for three different box sizes at $z = 6$, plotted against their respective Fiducial run. *Panel (d)*: Composite GSMF of the H_2 runs, compared with the Fiducial composite GSMF (black dashed line). Additionally we show DC corrections (Jaacks et al., 2012b) with (dot-dashed) and without (dotted) dust correction. The yellow shaded region is the observational estimate from González et al. (2010).

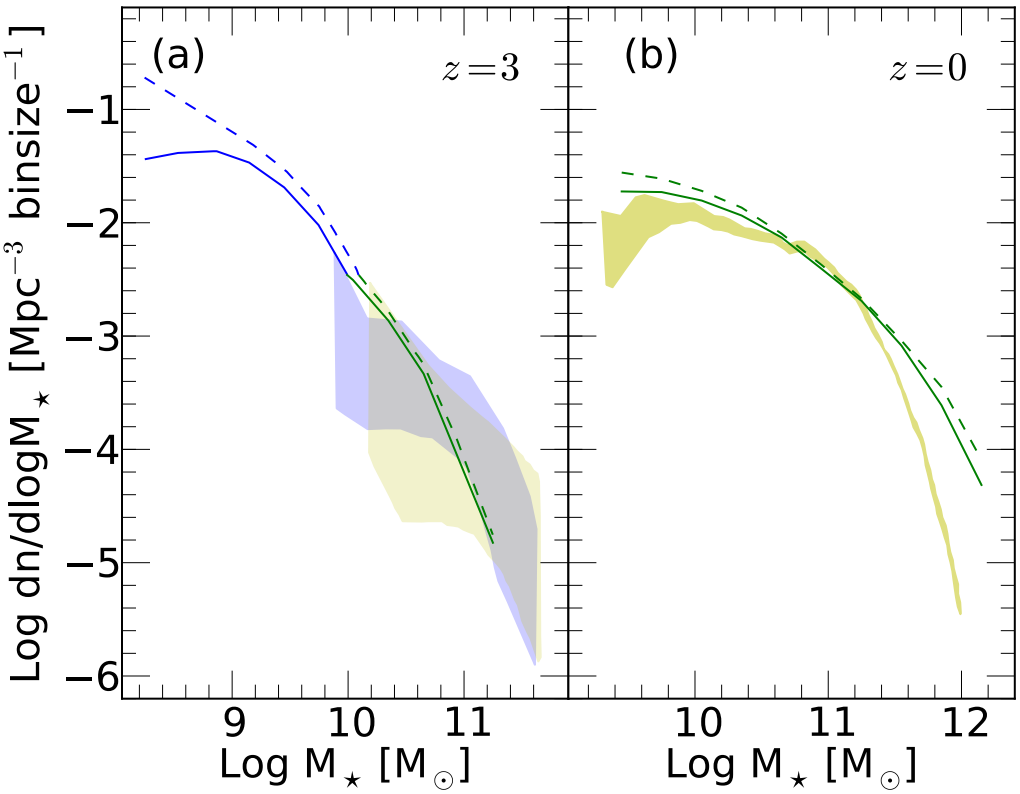

Figure 28 *Panel (a)*: composite GSMF for $z = 3$ for both the H_2 (solid lines) and Fiducial (dashed lines) runs. The data is from the N400L34 & N600L100 runs. The shaded regions represent observational estimates at $3 < z < 4$ (yellow) and $2 < z < 3$ (cyan) from Marchesini et al. (2009). *Panel (b)*: GSMF at $z = 0$ from the N600L100 run. The yellow shaded region is the observation from Cole et al. (2001).

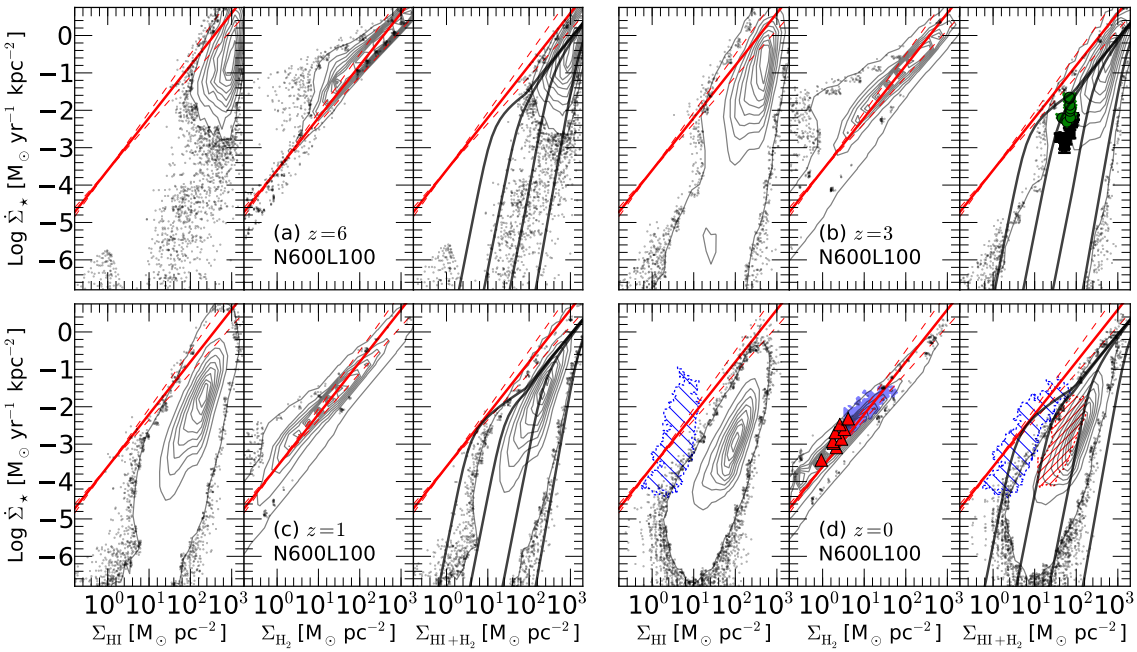

Figure 29 The Kennicutt-Schmidt relation for the N600L100 simulation at $z = 6, 3, 1,$ & 0. Each redshift is broken into three panels: SFR surface density as a function of HI(left panel, hereafter KS-HI), H_2 (middle panel, KS-H2), and HI $+H_2$ surface density (right panel, KS-HIH2). In each panel, the solid red line represents the empirical KS law given by Equation (3.3), and the dashed red lines represent the range of slope $\Delta n = \pm 0.15$. Blue hatched regions in the KS-HI and KS-HIH2 panels, and the blue solid contour in KS-H2 panel are the observations from Bigiel et al. (2008). The red triangles in the KS-H2 panels along with the red hatched region in the KS-HIH2 panels are low-metallicity SMC observations from Bolatto et al. (2011). At $z = 3$ we have observational data from Rafelski et al. (2011) plotted as green circles and black squares. The green circles represent upper limits derived for DLAs, while the black squares represent outskirts of LBGs. Lastly in KS-HIH2 panels, black lines represent theoretical results from the KMT model (Krumholz et al., 2009). In the $z = 6$ KS-HIH2 panel, the four theory lines correspond to the metallicities $\log(cZ/Z_\odot) = 0.11, -0.69, -1.49, -2.29$ from left to right, respectively. For $z = 3$, we have $\log(cZ/Z_\odot) = 0.47, -0.45, -1.37, -2.29$. For $z = 1$, $\log(cZ/Z_\odot) = 0.77, -0.25, -1.27, -2.29$, and for $z = 0$ $\log(cZ/Z_\odot) = 0.80, -0.23, -1.26, -2.29$. Any discreteness of the dotted points at the contour edge is an artifact from our plotting procedure.

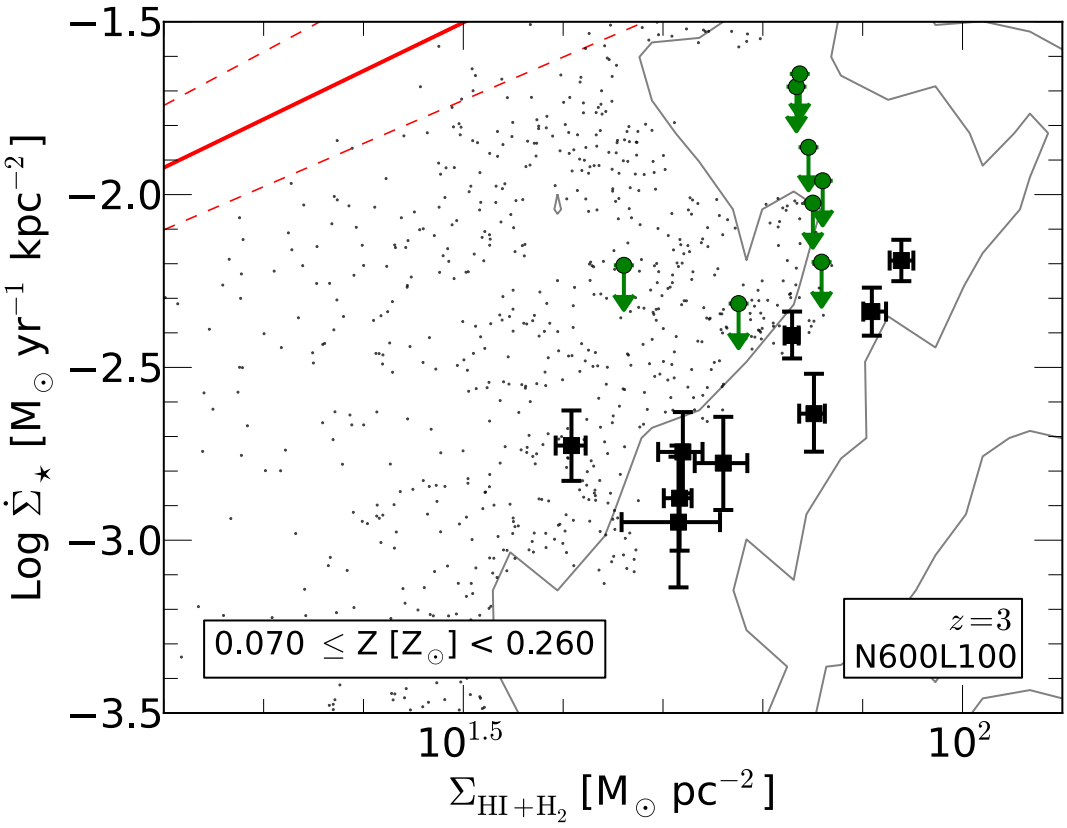

Figure 30 Enlarged region of Figure 29b KS-HIH2 plot. Here we only plot star-forming columns with metallicities consistent with observations from Rafelski et al. (2011) ($Z = 0.07 - 0.26\,Z_\odot$). Green circles represent upper limits derived for DLAs (Wolfe & Chen, 2006), and black squares represent outskirts of LBGs (Rafelski et al., 2011). The observed data points are at the upper edge of the simulation data contour, but there are many simulated columns that overlap with the observed data.

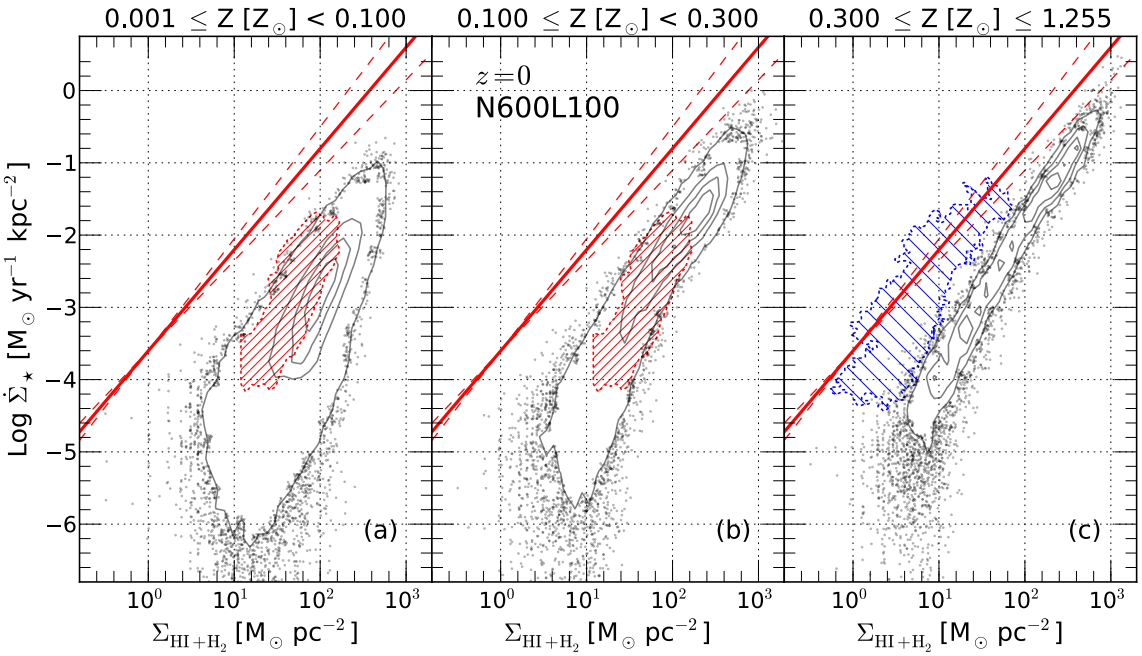

Figure 31 The KS-HIH2 panel from Figure 29d is separated into three different metallicity ranges at $z = 0$ using the N600L100 run, in order to show the metallicity effect on the KS plot. Panel (a) only shows columns with the lowest metallicities. The metallicity range in panel (b) brackets the Bolatto et al. (2011) SMC data. Panel (c) shows the highest metal columns, however, the median metallicity of the simulated columns are biased towards the lower end of the bracket $Z = 0.3\,Z_{\odot}$, which is presumably causing the offset between the simulation result and the blue hatched observed data.

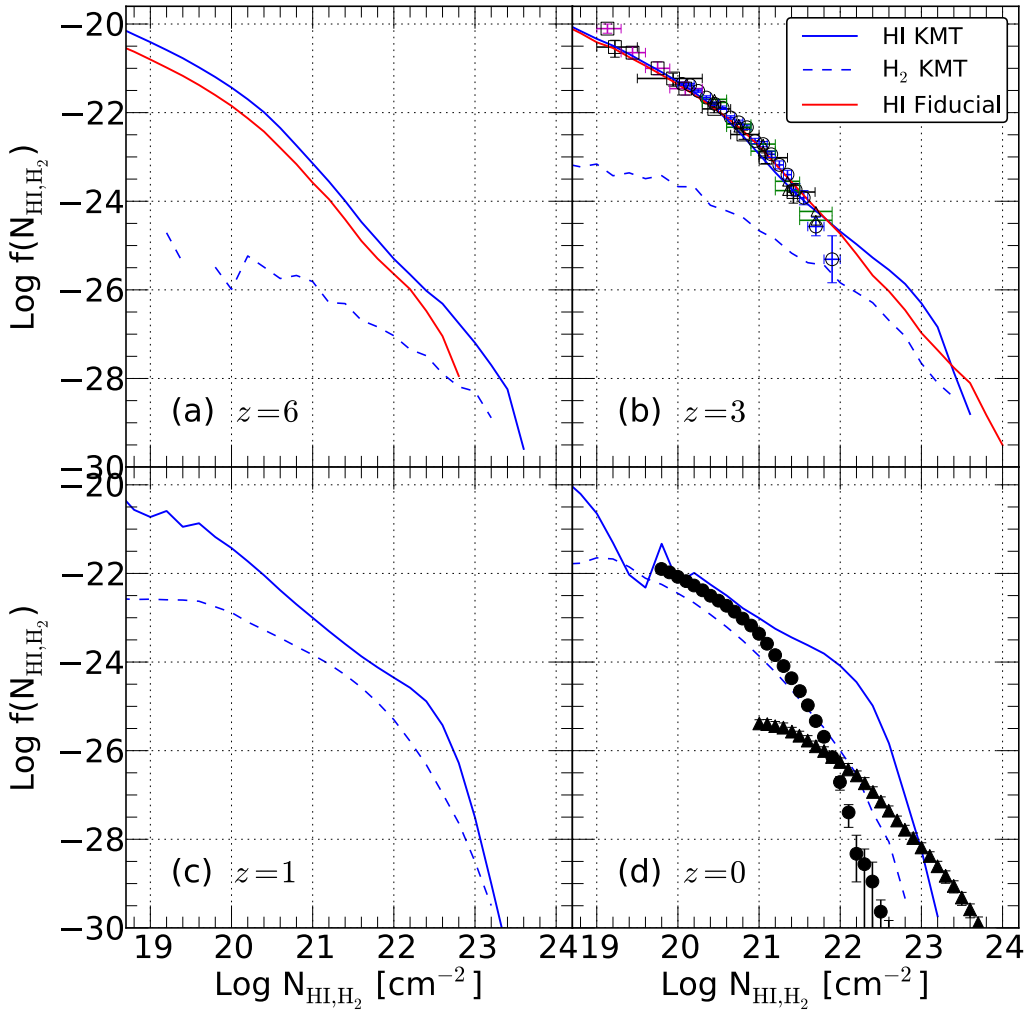

Figure 32 Column density distribution functions of HI and H_2 at $z = 6, 3, 1,$ & 0 for the H_2 and Fiducial runs. Redshifts $z = 6$ & 3 are from the N144L10 runs, while $z = 1$ & 0 are from the N600L100 H_2 runs (N600L100 Fiducial was omitted because it lacks the OTUV threshold). The observational data points at $z = 3$ are from Péroux et al. (2005, black squares), O'Meara et al. (2007, magenta squares), Prochaska & Wolfe (2009, green triangles), and Noterdaeme et al. (2009, blue circles). Panel (d) shows observations from Zwaan & Prochaska (2006), where black circles represent the HI and black triangles represent the H_2 column density distribution functions.

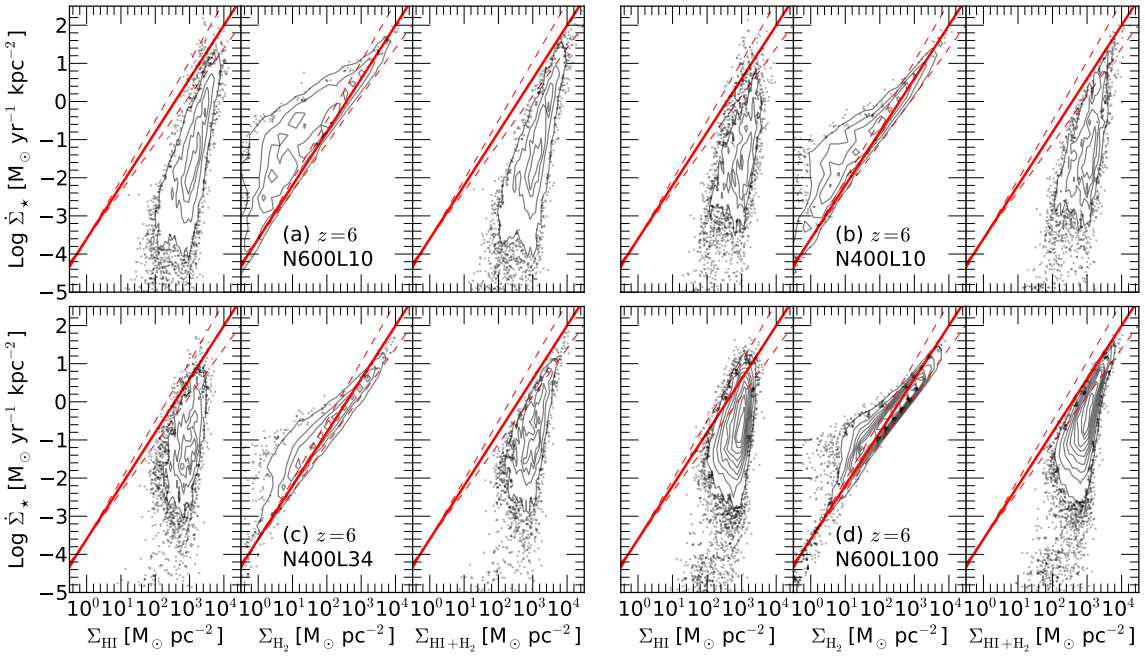

Figure 33 Similarly to Figure 29, we plot the KS relation for the N600L10, N400L10, N400L34, & N600L100 simulations at $z = 6$ to examine the resolution and box size effects. See text for detailed discussions.

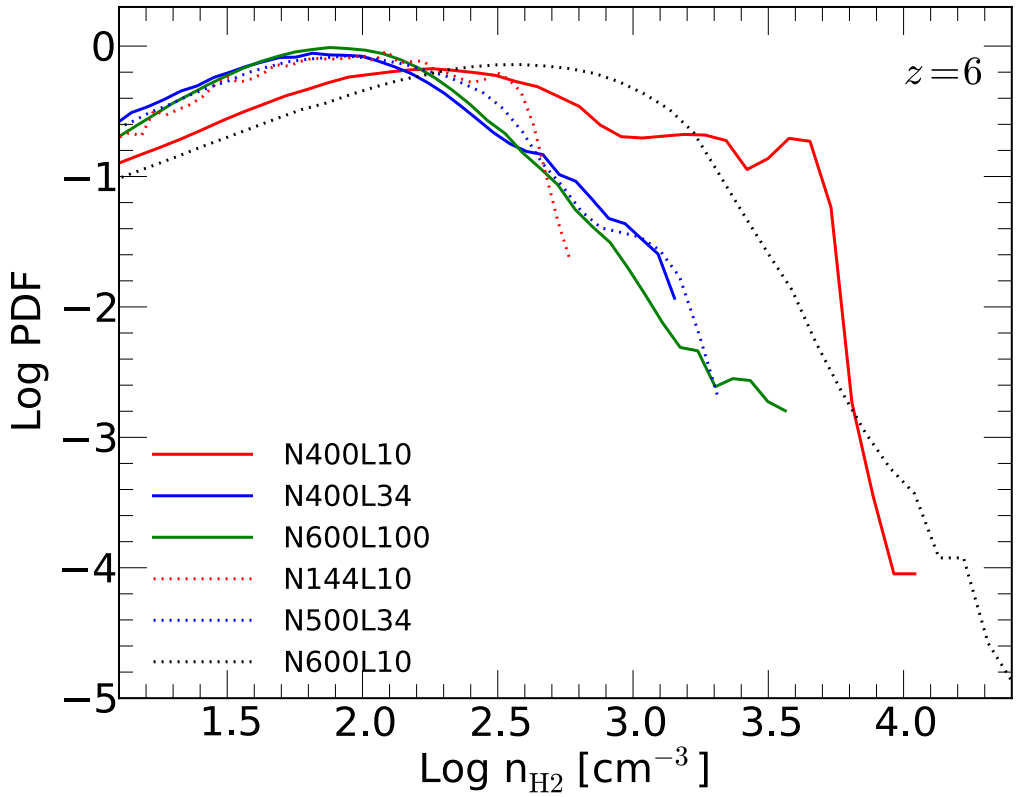

Figure 34 H_2 number density probability distribution functions for all runs in Table 5 at $z = 6$. One can see that the peak of the highest density region shifts to higher densities as the resolution increases.

CHAPTER 4

CONSTRUCTING A GALACTIC HALO & DISK

4.1 Introduction

Supernova explosions and stellar winds that happen on small scales affect the interstellar medium on galactic scales and regulate the formation of galaxies. Current cosmological simulations lack the necessary resolution to correctly follow these effects. For this reason many ad-hoc assumptions are employed in today's simulations at unresolved scales of sub-kiloparsecs. It is our goal to explore and develop a better method for implementing supernova feedback in large and small scale hydrodynamic simulations. Previous work has been done on large cosmological simulations (Choi & Nagamine, 2010). This work tackles the task of exploring these methods on smaller galactic scales and comparing results to observations. In order to properly do this we propose to simulate a single galaxy with high resolution. This allows for precise control and understanding of the effects these methods may have on the galaxy's morphology and star formation history.

The first phase of this research consists of the development of an initial condition generator for our toy galaxy. It is essential to study the effects from as early as possible, such as the spherical collapse of a gas cloud. The foundation for our toy galaxy is a spherical dark matter halo spatially distributed with a Hernquist (1990) density profile. It is a non-trivial task to form a halo in quasi-equilibrium. The velocities of our dark matter particles are assigned via a Monte Carlo method based upon the velocity distribution function detailed in Widrow (2000); Widrow & Dubinski (2005). Gas particles are then added with the same spatial distribution as the dark matter particles, and the velocities of the gas are assigned so that their angular momentum

is a fraction of the halo's (Mo et al., 1998).

4.2 DM Halo

We begin with the construction of a dark matter halo (DMH) in quasi-equilibrium. For this we first distribute the particles spatially according to a Hernquist (1990) density profile:

$$\rho_{dm}(r) = \frac{M_{dm}}{2\,\pi}\frac{a}{r\,(r+a)^3}. \tag{4.1}$$

Here M_{dm} is the total DM mass, and r is the radius. The parameter a is defined by

$$a = r_s\sqrt{2[\ln(1+c) - c/(1+c)]}, \tag{4.2}$$

where r_s is a characteristic scale length, and the concentration parameter c is defined as $c = r_{200}/r_s$ with r_{200} describing the radius at which the mean enclosed density is 200 times the critical density ($\rho_{crit} = 3H_0^2/(8\pi G)$). We then integrate Equation 4.1 from 0 to r obtaining an expression for the mass enclosed within a given radius:

$$M(<r) = M_{\rm dm}\frac{r^2}{(r+a)^2}. \tag{4.3}$$

To assign each particle an x, y, z position, we first generate a random radius. We accomplish this by solving Equation (4.3) for r

$$r = \frac{a\,\sqrt{M(<r)}}{\sqrt{M_{dm}} - \sqrt{M(<r)}}, \tag{4.4}$$

and generating a random number R_n for $M(<r)$. Position angles can be randomly generated via:

$$\theta = \cos^{-1}(R_n - 0.5), \tag{4.5}$$

$$\phi = R_n\,2\,\pi, \tag{4.6}$$

and spacial positions are then assigned by a simple coordinate transformation from spherical to Cartesian ($x = r\sin\theta\cos\phi$, $y = r\sin\theta\sin\phi$, $z = r\cos\theta$).

Next we must determine the DM particle velocities. We follow the velocity distribution function prescription outlined by Widrow & Dubinski (2005), and from Dr. Martin Weinberg's UMass class notes (taken by Jun-Hwan Choi). For each particle we determine the maximum velocity by its gravitational potential:

$$V_{max} = \sqrt{2(E_{max} - \Phi(r))}, \tag{4.7}$$

where $\Phi(r) = -GM_{dm}/(a+r)$, and $E_{max} = -GM_{dm}/(a+r_{200})$. Then V_{max} is broken into its radial and tangential components:

$$V_r = (\pm 1)\, V_{max}\, p, \tag{4.8}$$

$$V_t = V_{max}\sqrt{R_n\,(1-p^2)}, \tag{4.9}$$

where p is defined by:

$$p = -2\,\cos\left[\frac{\cos^{-1}\,R_n}{3} - \frac{2\pi}{3}\right]. \tag{4.10}$$

Now we combine the potential and kinetic energies for the total energy of each particle:

$$E(r) = \Phi(r) + \frac{1}{2}(V_r^2 + V_t^2). \tag{4.11}$$

Next we can calculate the dimensionless distribution function $\mathcal{F}$:

$$\mathcal{F}_H(q) = \frac{1}{2^{7/2}\pi^3}\frac{1}{(1-q^2)^{5/2}} \times [3\,\sin^{-1}q + (1+q^2)^{1/2}(1-2q^2)(8q^4-8q^2-3)] \tag{4.12}$$

where $q \equiv \sqrt{-E(r)/\sigma^2}$, $q_{max} \equiv \sqrt{-E_{max}/\sigma^2}$, and $\sigma^2 = M_{dm}/a$. We then use a Monte-Carlo 'accept-reject' method to determine if we shall proceed. This involves taking the ratio of $\mathcal{F}_H(q)/\mathcal{F}_H(q_{max})$ and comparing it to a random number R_n. If the

ratio is larger than R_n then the calculation proceeds; if not, the calculation repeats with another set of random numbers. Once this ratio is accepted we proceed to assigning V_x, V_y, V_z velocities.

At this point $V_r \,\&\, V_t$ are known; in order to transform back to Cartesian coordinates V_t must be broken into additional components. This can be accomplished by $V_{tx} = V_t \cos\chi$, and $V_{ty} = V_t \sin\chi$ where $\chi = 2\pi R_n$. We can now simply transform coordinate systems as we did for the positions ($V_x = V_r \sin\theta\cos\phi + V_{tx}\cos\theta\cos\phi - V_{ty}\sin\phi$, $V_y = V_r \sin\theta\sin\phi + V_{tx}\cos\theta\sin\phi + V_{ty}\cos\phi$, $V_z = V_r\cos\theta - V_{tx}\sin\theta$).

This prescription has allowed us to create a DM halo in quasi-equilibrium. A DM only simulation of this halo was ran, and the density profile continually matched the theoretical Hernquist (1990) profile well for $\sim$ 400 million years. There were some initial density perturbations, or relaxation waves, that propagated throughout the halo but they had minimal impact on the overall profile.

4.3 Gas

The next component to be added to our 'toy' galaxy is gas. We spatially distribute the gas in the exact same manner as the DM (Section 4.2). The velocities of the gas particles however, are determined quite differently. Mo et al. (1998) outlines a prescription for determining gas velocities assuming that the angular momentum of the gas is a fraction of the halo's angular momentum. Many attempts at having an isothermal (T $\sim 10^4$K) gaseous sphere collapse to a disk were unsuccesful. Most led to the gaseous halo expanding indefinitely. We later assigned a temperature gradient to the gas of the form:

$$T(r) = \frac{\mu}{k_B}\frac{1}{\rho_h}\int_r^\infty \rho_h(r)\frac{GM(r)}{r^2}dr, \tag{4.13}$$

where μ is the mean molecular weight, and k_B is the Boltzmann constant 1.4×10^{-16} erg/K (Kaufmann et al., 2007). The halos no longer expanded indefinitely,

instead they collapsed and underwent significant fragmentation preventing the formation of a disk.

4.4 Conclusions

Much time and effort was involved in the attempt to make an initial condition generator for a single disk galaxy from scratch. Ultimately it was determined that creating a galaxy in this manner was not realistic in the cosmological context. Cold gas inflows from cosmological filaments for example, can play an important role in star formation within galaxies (e.g. Dekel et al., 2009). Others who study single galaxy simulations usually create their initial conditions in an ad-hoc manner. They start with the galaxy already formed and do not consider any type of spherical collapse (e.g. Cox et al., 2006; Tasker & Bryan, 2006; Robertson & Kravtsov, 2008). In light of this, attention was diverted to implementing the H_2-based star formation model described in Chapter 3.

CHAPTER 5

CONCLUSIONS

Two primary studies were presented along with a brief discussion of unpublished work. Chapter 2 provides a resolution study of N-body simulations and examines the probability of finding a halo pair whose relative velocity is comparable to inferred estimates of 1E0657-56. At the time of publication, we concluded that ΛCDM was incompatible with current observations. Recent observations of 1E0657-56 by Paraficz et al. (2012) however, have significantly reduced the mass estimates of these two halos. This could possibly ease the tension between theory and observations by altering the required initial conditions needed to reproduce such observations within simulation. Further improvements to observations and simulations of this interesting system are needed before ΛCDM is ruled out.

Chapter 3 details our investigation of cosmological smoothed particle hydrodynamic simulations including baryonic physics. We conducted a comparison study between previous sub-grid star formation (SF) models and a new molecular hydrogen (H_2) based SF model. The new H_2 prescription was found to provide three distinct advantages when compared to previous models. First, it reduces the number of low mass galaxies at $M_\star \leq 10^8 M_\odot$. When combined with duty cycle arguments and dust extinction our GSMF becomes closer to the observational estimates at $z = 6$ (Figure 27). Secondly, the H_2 SF model is in very good agreement with the semi-analytic and observed SHMR at $z = 6$; the Fiducial model on the other hand severely over-predicts the stellar mass contained within low mass halos. At later redshifts the discrepancy between the H_2 and Fiducial SHMR diminishes, but the H_2 runs continue to be in closer agreement with the SMHM relation (Figure 21). Finally, our new H_2

prescription is found to naturally reproduce the Kennicutt-Schmidt (KS) relationship at all redshifts without having to tweak parameters of the model (Figure 29). Unfortunately, the gas columns within our simulations are found to have low metallicities resulting in disagreement with some observations.

This leads to the disadvantages of the new H_2 prescription. As it currently stands, our new model under predicts the mass-metallicity relationship (Figure 25) at low redshift. However, the disagreement at early times is not as severe. Comparing to our Fiducial run and observations, one could argue that our new H_2 model is inferior when it comes to metal enrichment. It is unclear at this point as to how we should go about improving the model to account for this discrepancy. Since our new model heavily depends on the gas column density and metallicity, one idea we would like to explore in future work is the implementation of metal diffusion within our simulations. Standard SPH codes do not allow particles to share their properties with one another. No diffusion occurs for example, if a high Z gas particles is next to a low Z gas particle. Greif et al. (2009); Shen et al. (2010) have implemented such diffusion techniques in SPH codes; it would be worthwhile to see if these methods could improve our results. Lastly this model introduces an implicit resolution dependence. As the resolution improves, the simulation can form higher density regions which may artificially enhance star formation. Because of this, we must choose our problems carefully when using this model. Overall we believe the benefits of the H_2 based SF model outweigh the disadvantages.

REFERENCES

Abazajian, K. N., Adelman-McCarthy, J. K., Agüeros, M. A., Allam, S. S., Allende Prieto, C., An, D., Anderson, K. S. J., Anderson, S. F., Annis, J., Bahcall, N. A., & et al. 2009, ApJS, 182, 543

Altay, G., Theuns, T., Schaye, J., Crighton, N. H. M., & Dalla Vecchia, C. 2011, ApJL, 737, L37

Azzalini, A. & Capitanio, A. 2009, ArXiv e-prints

Baldry, I. K., Glazebrook, K., & Driver, S. P. 2008, MNRAS, 388, 945

Barnes, J. & Hut, P. 1986, Nature, 324, 446

Bate, M. R. & Burkert, A. 1997, MNRAS, 288, 1060

Behroozi, P. S., Conroy, C., & Wechsler, R. H. 2010, ApJ, 717, 379

Behroozi, P. S., Wechsler, R. H., & Conroy, C. 2012, ArXiv e-prints

Bertschinger, E. & Dekel, A. 1989, ApJL, 336, L5

Bigiel, F., Leroy, A., Walter, F., Brinks, E., de Blok, W. J. G., Madore, B., & Thornley, M. D. 2008, AJ, 136, 2846

Blumenthal, G. et al. 1984, Nature, 311, 517

Bolatto, A. D., Leroy, A. K., Jameson, K., Ostriker, E., Gordon, K., Lawton, B., Stanimirović, S., Israel, F. P., et al. 2011, ApJ, 741, 12

Bouwens, R., Bradley, L., Zitrin, A., Coe, D., Franx, M., Zheng, W., Smit, R., Host, O., et al. 2012, ArXiv e-prints

Bouwens, R. J., Illingworth, G. D., Oesch, P. A., Labbé, I., Trenti, M., van Dokkum, P., Franx, M., Stiavelli, M., et al. 2011, ApJ, 737, 90

Bradač, M., Clowe, D., Gonzalez, A. H., Marshall, P., Forman, W., Jones, C., Markevitch, M., Randall, S., Schrabback, T., & Zaritsky, D. 2006, ApJ, 652, 937

Brinchmann, J., Charlot, S., White, S. D. M., Tremonti, C., Kauffmann, G., Heckman, T., & Brinkmann, J. 2004, MNRAS, 351, 1151

Bryan, G. L. & Norman, M. L. 1997, ArXiv Astrophysics e-prints

Cen, R. & Ostriker, J. P. 1992, ApJL, 399, L113

Chabrier, G. 2003, PASP, 115, 763

Choi, E., Ostriker, J. P., Naab, T., & Johansson, P. H. 2012, ApJ, 754, 125

Choi, J.-H. & Nagamine, K. 2009, MNRAS, 393, 1595

—. 2010, MNRAS, 407, 1464

—. 2011, MNRAS, 410, 2579

Christensen, C., Quinn, T., Governato, F., Stilp, A., Shen, S., & Wadsley, J. 2012, ArXiv e-prints

Clowe, D., Bradač, M., Gonzalez, A. H., Markevitch, M., Randall, S. W., Jones, C., & Zaritsky, D. 2006, ApJL, 648, L109

Clowe, D., Gonzalez, A., & Markevitch, M. 2004, ApJ, 604, 596

Coe, D., Zitrin, A., Carrasco, M., Shu, X., Zheng, W., Postman, M., Bradley, L., Koekemoer, A., et al. 2012, ArXiv e-prints

Cole, S., Norberg, P., Baugh, C. M., Frenk, C. S., Bland-Hawthorn, J., Bridges, T., Cannon, R., Colless, M., et al. 2001, MNRAS, 326, 255

Conroy, C., Wechsler, R. H., & Kravtsov, A. V. 2007, ApJ, 668, 826

Cox, T. J., Jonsson, P., Primack, J. R., & Somerville, R. S. 2006, MNRAS, 373, 1013

Crocce, M., Fosalba, P., Castander, F. J., & Gaztañaga, E. 2010, MNRAS, 403, 1353

Daddi, E., Dickinson, M., Morrison, G., Chary, R., Cimatti, A., Elbaz, D., Frayer, D., Renzini, A., Pope, A., Alexander, D. M., Bauer, F. E., Giavalisco, M., Huynh, M., Kurk, J., & Mignoli, M. 2007, ApJ, 670, 156

Davé, R., Hernquist, L., Katz, N., & Weinberg, D. H. 1999, ApJ, 511, 521

Davis, M., Nusser, A., & Willick, J. A. 1996, ApJ, 473, 22

Davis, M. et al. 1985, ApJ, 292, 371

Dekel, A., Birnboim, Y., Engel, G., Freundlich, J., Goerdt, T., Mumcuoglu, M., Neistein, E., Pichon, C., Teyssier, R., & Zinger, E. 2009, Nature, 457, 451

Di Matteo, T., Springel, V., & Hernquist, L. 2005, Nature, 433, 604

Dicke, R. et al. 1965, ApJ, 142, 414

Draine, B. T. 1978, ApJS, 36, 595

Efstathiou, G., Sutherland, W. J., & Maddox, S. J. 1990, Nature, 348, 705

Eisenstein, D. J. & Hu, W. 1998, ApJ, 496, 605

Elbaz, D., Daddi, E., Le Borgne, D., Dickinson, M., Alexander, D. M., Chary, R.-R., Starck, J.-L., Brandt, W. N., et al. 2007, A&A, 468, 33

Erb, D. K., Steidel, C. C., Shapley, A. E., Pettini, M., Reddy, N. A., & Adelberger, K. L. 2006, ApJ, 646, 107

Erkal, D., Gnedin, N. Y., & Kravtsov, A. V. 2012, ArXiv e-prints

Evoli, C., Salucci, P., Lapi, A., & Danese, L. 2011, ApJ, 743, 45

Faucher-Giguère, C.-A., Lidz, A., Zaldarriaga, M., & Hernquist, L. 2009, ApJ, 703, 1416

Feldmann, R., Gnedin, N. Y., & Kravtsov, A. V. 2011, ApJ, 732, 115

Finlator, K., Oppenheimer, B. D., & Davé, R. 2011, MNRAS, 410, 1703

Forero-Romero, J. E., Gottlöber, S., & Yepes, G. 2010, ApJ, 725, 598

Foucaud, S., Conselice, C. J., Hartley, W. G., Lane, K. P., Bamford, S. P., Almaini, O., & Bundy, K. 2010, MNRAS, 406, 147

Friedmann, A. 1922, Zeitschrift für Physik A Hadrons and Nuclei, 10, 377

—. 1924, Zeitschrift für Physik A Hadrons and Nuclei, 21, 326

Fu, J., Guo, Q., Kauffmann, G., & Krumholz, M. R. 2010, MNRAS, 409, 515

Fukushige, T. & Suto, Y. 2001, ApJL, 557, L11

Gnedin, N. Y., Tassis, K., & Kravtsov, A. V. 2009, ApJ, 697, 55

González, V., Labbé, I., Bouwens, R. J., Illingworth, G., Franx, M., Kriek, M., & Brammer, G. B. 2010, ApJ, 713, 115

Gottlöber, S. & Yepes, G. 2007, ApJ, 664, 117

Graham, A. W., Driver, S. P., Petrosian, V., Conselice, C. J., Bershady, M. A., Crawford, S. M., & Goto, T. 2005, AJ, 130, 1535

Greif, T. H., Glover, S. C. O., Bromm, V., & Klessen, R. S. 2009, MNRAS, 392, 1381

Grogin, N. A., Kocevski, D. D., Faber, S. M., Ferguson, H. C., Koekemoer, A. M., Riess, A. G., Acquaviva, V., Alexander, D. M., et al. 2011, ApJS, 197, 35

Haardt, F. & Madau, P. 1996, ApJ, 461, 20

Hayashi, E. & White, S. D. M. 2006, MNRAS, 370, L38

Hernquist, L. 1990, ApJ, 356, 359

Hockney, R. W. & Eastwood, J. W. 1981, Computer Simulation Using Particles, ed. Hockney, R. W. & Eastwood, J. W.

Horiuchi, S., Beacom, J. F., & Dwek, E. 2009, PhysRevD, 79, 083013

Jaacks, J., Choi, J.-H., Nagamine, K., Thompson, R., & Varghese, S. 2012a, MNRAS, 420, 1606

Jaacks, J., Nagamine, K., & Choi, J.-H. 2012b, ArXiv e-prints

Juszkiewicz, R., Springel, V., & Durrer, R. 1999, ApJL, 518, L25

Katz, N. 1992, ApJ, 391, 502

Katz, N., Weinberg, D. H., & Hernquist, L. 1996, ApJS, 105, 19

Kaufmann, T. et al. 2007, MNRAS, 375, 53

Kennicutt, Jr., R. C. 1998, ApJ, 498, 541

Kennicutt, Jr., R. C., Calzetti, D., Walter, F., Helou, G., Hollenbach, D. J., Armus, L., Bendo, G., Dale, D. A., et al. 2007, ApJ, 671, 333

Kewley, L. J. & Ellison, S. L. 2008, ApJ, 681, 1183

Kistler, M. D., Yüksel, H., Beacom, J. F., Hopkins, A. M., & Wyithe, J. S. B. 2009, ApJL, 705, L104

Klypin, A. A. & Shandarin, S. F. 1983, MNRAS, 204, 891

Komatsu, E., Dunkley, J., Nolta, M. R., Bennett, C. L., Gold, B., Hinshaw, G., Jarosik, N., Larson, D., Limon, M., Page, L., Spergel, D. N., Halpern, M., Hill, R. S., Kogut, A., Meyer, S. S., Tucker, G. S., Weiland, J. L., Wollack, E., & Wright, E. L. 2009, ApJS, 180, 330

Komatsu, E., Smith, K. M., Dunkley, J., Bennett, C. L., Gold, B., Hinshaw, G., Jarosik, N., Larson, D., et al. 2011, ApJS, 192, 18

Kowalski, M. et al. 2008, ApJ, 686, 749

Kritsuk, A. G. & Norman, M. L. 2011, ArXiv e-prints

Krumholz, M. R. 2012, ArXiv e-prints

Krumholz, M. R. & Dekel, A. 2011, ArXiv e-prints

Krumholz, M. R., Dekel, A., & McKee, C. F. 2012, ApJ, 745, 69

Krumholz, M. R. & Gnedin, N. Y. 2011, ApJ, 729, 36

Krumholz, M. R., McKee, C. F., & Tumlinson, J. 2008, ApJ, 689, 865

—. 2009, ApJ, 693, 216

Krumholz, M. R. & Tan, J. C. 2007, ApJ, 654, 304

Kuhlen, M., Krumholz, M. R., Madau, P., Smith, B. D., & Wise, J. 2012, ApJ, 749, 36

Labbé, I., González, V., Bouwens, R. J., Illingworth, G. D., Oesch, P. A., van Dokkum, P. G., Carollo, C. M., Franx, M., Stiavelli, M., Trenti, M., Magee, D., & Kriek, M. 2010, ApJL, 708, L26

Lada, C. J., Lombardi, M., & Alves, J. F. 2010, ApJ, 724, 687

Landy, S. D. & Szalay, A. S. 1993, ApJ, 412, 64

Lara-Lopez, M. A., Hopkins, A. M., Robotham, A., Owers, M. S., Colless, M., Brough, S., Norberg, P., Steele, O., et al. 2012, ArXiv e-prints

Leauthaud, A., Tinker, J., Bundy, K., Behroozi, P. S., Massey, R., Rhodes, J., George, M. R., Kneib, J.-P., et al. 2012, ApJ, 744, 159

Lee, J. & Komatsu, E. 2010, ApJ, 718, 60

Lee, K.-S., Dey, A., Reddy, N., Brown, M. J. I., Gonzalez, A. H., Jannuzi, B. T., Cooper, M. C., Fan, X., et al. 2011, ApJ, 733, 99

Lemaître, G. 1927, Annales de la Société Scientifique de Bruxelles, 47, 49

Leroy, A. K., Walter, F., Brinks, E., Bigiel, F., de Blok, W. J. G., Madore, B., & Thornley, M. D. 2008, AJ, 136, 2782

Lo Faro, B., Monaco, P., Vanzella, E., Fontanot, F., Silva, L., & Cristiani, S. 2009, MNRAS, 399, 827

Mac Low, M.-M. & Glover, S. C. O. 2012, ApJ, 746, 135

Marchesini, D., van Dokkum, P. G., Förster Schreiber, N. M., Franx, M., Labbé, I., & Wuyts, S. 2009, ApJ, 701, 1765

Markevitch, M. 2006, in ESA Special Publication, Vol. 604, The X-ray Universe 2005, ed. A. Wilson, 723–+

Markevitch, M., Gonzalez, A. H., Clowe, D., Vikhlinin, A., Forman, W., Jones, C., Murray, S., & Tucker, W. 2004, ApJ, 606, 819

Mastropietro, C. & Burkert, A. 2008, MNRAS, 389, 967

McGaugh, S. S. 2005, ApJ, 632, 859

McKee, C. F. & Krumholz, M. R. 2010, ApJ, 709, 308

McKee, C. F. & Ostriker, E. C. 2007, ARA&A, 45, 565

Milosavljević, M., Koda, J., Nagai, D., Nakar, E., & Shapiro, P. R. 2007, ApJL, 661, L131

Mo, H. et al. 1998, MNRAS, 295, 319

Mo, H. J. & White, S. D. M. 2002, MNRAS, 336, 112

More, S., Kravtsov, A., Dalal, N., & Gottlöber, S. 2011, ArXiv e-prints

Moster, B. P., Somerville, R. S., Maulbetsch, C., van den Bosch, F. C., Macciò, A. V., Naab, T., & Oser, L. 2010, ApJ, 710, 903

Munshi, F., Governato, F., Brooks, A. M., Christensen, C., Shen, S., Loebman, S., Moster, B., Quinn, T., & Wadsley, J. 2012, ArXiv e-prints

Nagamine, K., Cen, R., Hernquist, L., Ostriker, J. P., & Springel, V. 2005, ApJ, 627, 608

Nagamine, K., Choi, J.-H., & Yajima, H. 2010, ApJL, 725, L219

Nagamine, K., Ostriker, J. P., Fukugita, M., & Cen, R. 2006, ApJ, 653, 881

Nagamine, K., Springel, V., & Hernquist, L. 2004a, MNRAS, 348, 421

—. 2004b, MNRAS, 348, 435

Nagamine, K., Springel, V., Hernquist, L., & Machacek, M. 2004c, MNRAS, 350, 385

Night, C., Nagamine, K., Springel, V., & Hernquist, L. 2006, MNRAS, 366, 705

Noterdaeme, P., Petitjean, P., Ledoux, C., & Srianand, R. 2009, A&A, 505, 1087

O'Meara, J. M., Prochaska, J. X., Burles, S., Prochter, G., Bernstein, R. A., & Burgess, K. M. 2007, ApJ, 656, 666

Ono, Y., Ouchi, M., Shimasaku, K., Dunlop, J., Farrah, D., McLure, R., & Okamura, S. 2010, ApJ, 724, 1524

O'Shea, B. W., Bryan, G., Bordner, J., Norman, M. L., Abel, T., Harkness, R., & Kritsuk, A. 2004, ArXiv Astrophysics e-prints

O'Shea, B. W., Nagamine, K., Springel, V., Hernquist, L., & Norman, M. L. 2005, ApJS, 160, 1

Ostriker, J. P., Choi, E., Ciotti, L., Novak, G. S., & Proga, D. 2010, ApJ, 722, 642

Ostriker, J. P. & Steinhardt, P. J. 1995, Nature, 377, 600

Papastergis, E., Cattaneo, A., Huang, S., Giovanelli, R., & Haynes, M. P. 2012, ApJ, 759, 138

Paraficz, D., Kneib, J.-P., Richard, J., Morandi, A., Limousin, M., & Jullo, E. 2012, ArXiv e-prints

Peebles, P. J. E. 1980, The large-scale structure of the universe, ed. Peebles, P. J. E.

Peeples, M. S. & Shankar, F. 2011, MNRAS, 417, 2962

Penprase, B. E., Prochaska, J. X., Sargent, W. L. W., Toro-Martinez, I., & Beeler, D. J. 2010, ApJ, 721, 1

Penzias, A. & Wilson, R. 1965, ApJ, 142, 419

Péroux, C., Dessauges-Zavadsky, M., D'Odorico, S., Sun Kim, T., & McMahon, R. G. 2005, MNRAS, 363, 479

Pontzen, A., Deason, A., Governato, F., Pettini, M., Wadsley, J., Quinn, T., Brooks, A., Bellovary, J., & Fynbo, J. P. U. 2010, MNRAS, 402, 1523

Postman, M., Coe, D., Benítez, N., Bradley, L., Broadhurst, T., Donahue, M., Ford, H., Graur, O., et al. 2012, ApJS, 199, 25

Prochaska, J. X. & Wolfe, A. M. 2009, ApJ, 696, 1543

Rafelski, M., Wolfe, A. M., & Chen, H.-W. 2011, ApJ, 736, 48

Rahmati, A., Pawlik, A. P., Raičević, M., & Schaye, J. 2012, ArXiv e-prints

Raue, M. & Meyer, M. 2012, MNRAS, 426, 1097

Reddy, N. A. & Steidel, C. C. 2009, ApJ, 692, 778

Renaud, F., Kraljic, K., & Bournaud, F. 2012, ArXiv e-prints

Riess, A. G., Filippenko, A. V., Challis, P., Clocchiatti, A., Diercks, A., Garnavich, P. M., Gilliland, R. L., Hogan, C. J., Jha, S., Kirshner, R. P., Leibundgut, B., Phillips, M. M., Reiss, D., Schmidt, B. P., Schommer, R. A., Smith, R. C., Spyromilio, J., Stubbs, C., Suntzeff, N. B., & Tonry, J. 1998, AJ, 116, 1009

Robertson, B. E. & Kravtsov, A. V. 2008, ApJ, 680, 1083

Robertson, H. 1935, ApJ, 82, 248

—. 1936a, ApJ, 83, 187

—. 1936b, ApJ, 83, 257

Rodríguez, M. & Delgado-Inglada, G. 2011, ApJL, 733, L50

Salpeter, E. E. 1955, ApJ, 121, 161

Savaglio, S., Glazebrook, K., Le Borgne, D., Juneau, S., Abraham, R. G., Chen, H.-W., Crampton, D., McCarthy, P. J., et al. 2005, ApJ, 635, 260

Sawala, T., Frenk, C. S., Crain, R. A., Jenkins, A., Schaye, J., Theuns, T., & Zavala, J. 2012, ArXiv e-prints

Schaye, J. & Dalla Vecchia, C. 2008, MNRAS, 383, 1210

Schiminovich, D., Ilbert, O., Arnouts, S., Milliard, B., Tresse, L., Le Fèvre, O., Treyer, M., Wyder, T. K., et al. 2005, ApJL, 619, L47

Schmidt, M. 1959, ApJ, 129, 243

Shen, S., Wadsley, J., & Stinson, G. 2010, MNRAS, 407, 1581

Sheth, R. K. & Tormen, G. 1999, MNRAS, 308, 119

Smoot, G. et al. 1992, ApJ, 396, L1

Springel, V. 2005, MNRAS, 364, 1105

—. 2010, ARA&A, 48, 391

Springel, V., Di Matteo, T., & Hernquist, L. 2005a, ApJL, 620, L79

Springel, V. & Farrar, G. R. 2007, MNRAS, 380, 911

Springel, V., Frenk, C. S., & White, S. D. M. 2006, Nature, 440, 1137

Springel, V. & Hernquist, L. 2003, MNRAS, 339, 289

Springel, V., White, S. D. M., Jenkins, A., Frenk, C. S., Yoshida, N., Gao, L., Navarro, J., Thacker, R., Croton, D., Helly, J., Peacock, J. A., Cole, S., Thomas, P., Couchman, H., Evrard, A., Colberg, J., & Pearce, F. 2005b, Nature, 435, 629

Springel, V., White, S. D. M., Tormen, G., & Kauffmann, G. 2001, MNRAS, 328, 726

Tasker, E. J. & Bryan, G. L. 2006, ApJ, 641, 878

Thompson, R. & Nagamine, K. 2012, MNRAS, 419, 3560

Tremonti, C. A., Heckman, T. M., Kauffmann, G., Brinchmann, J., Charlot, S., White, S. D. M., Seibert, M., Peng, E. W., et al. 2004, ApJ, 613, 898

Wadsley, J. W., Stadel, J., & Quinn, T. 2004, Nature, 9, 137

Walker, A. 1937, Proceedings of the London Mathematical Society, s2-42(1), 90

Walter, F., Brinks, E., de Blok, W. J. G., Bigiel, F., Kennicutt, Jr., R. C., Thornley, M. D., & Leroy, A. 2008, AJ, 136, 2563

West, A. A., Garcia-Appadoo, D. A., Dalcanton, J. J., Disney, M. J., Rockosi, C. M., & Ivezić, Ž. 2009, AJ, 138, 796

West, A. A., Garcia-Appadoo, D. A., Dalcanton, J. J., Disney, M. J., Rockosi, C. M., Ivezić, Ž., Bentz, M. C., & Brinkmann, J. 2010, AJ, 139, 315

White, S. D. M., Frenk, C. S., & Davis, M. 1983, ApJL, 274, L1

Widrow, L. 2000, ApJS, 131, 39

Widrow, L. & Dubinski, J. 2005, ApJ, 631, 838

Willick, J. A., Courteau, S., Faber, S. M., Burstein, D., Dekel, A., & Kolatt, T. 1996, ApJ, 457, 460

Wise, J. H., Turk, M. J., Norman, M. L., & Abel, T. 2012, ApJ, 745, 50

Wolfe, A. M. & Chen, H.-W. 2006, ApJ, 652, 981

Wolfe, A. M., Gawiser, E., & Prochaska, J. X. 2005, ARA&A, 43, 861

Wolfire, M. G., Tielens, A. G. G. M., Hollenbach, D., & Kaufman, M. J. 2008, ApJ, 680, 384

Wong, T. & Blitz, L. 2002, ApJ, 569, 157

Yajima, H., Choi, J.-H., & Nagamine, K. 2011, ArXiv e-prints

Zehavi, I., Zheng, Z., Weinberg, D. H., Blanton, M. R., Bahcall, N. A., Berlind, A. A., Brinkmann, J., Frieman, J. A., et al. 2010, ArXiv e-prints

Zwaan, M. A. & Prochaska, J. X. 2006, ApJ, 643, 675

VITA

Graduate College
University of Nevada, Las Vegas

Robert Jo Thompson

Degrees:

Associate of Science, 2004
Community College of Southern Nevada

Bachelor of Sciences, Physics, 2008
Masters of Science, Astronomy, 2010
University of Nevada, Las Vegas

Thesis Title: Thesis Title

Thesis Examination Committee:
Chairperson, Kentaro Nagamine, Ph. D.
Committee Member, Daniel Proga, Ph. D.
Committee Member, Stephen Lepp, Ph. D.
Graduate Faculty Representative, Balakrishnan Naduvalath, Ph. D.